The Pennsylvania State University

The Graduate School

Department of Electrical Engineering

INTELLIGENT CONTROL OF A FUEL CELL POWER PLANT AS A DISTRIBUTED GENERATION SOURCE

A Dissertation in

Electrical Engineering

by

Tae-Il Choi

Submitted in Partial Fulfillment
of the Requirements
for the Degree of

Doctor of Philosophy

May 2008

The dissertation of Tae-Il Choi was reviewed and approved* by the following:

Kwang Y. Lee
Professor of Electrical Engineering
Dissertation Advisor
Chair of Committee

Heath F. Hofmann
Associate Professor of Electrical Engineering

Jeffrey S. Mayer
Associate Professor of Electrical Engineering

Robert M. Edwards
Professor of Nuclear Engineering

W. Kenneth Jenkins
Professor of Electrical Engineering
Head of the Department of Electrical Engineering

*Signatures are on file in the Graduate School.

ABSTRACT

Environmental problems caused by fossil fuel energy have become a focus of attention. Deregulation has accelerated the development of various types of alternative technologies as inventors see the opportunity to compete in market niches that did not exist a few short years ago. Specific market needs include producing reliable and voltage sag-free power in a manner that is less disruptive to the environment as well as the ability to supply power where it is too expensive to string power lines. Fuel cells will start out as a high-cost technology, supplying electricity (and heat) to these niches and gradually become more attractive to mainstream electricity users as they improve in capability and decrease in cost.

The Molten Carbonate Fuel Cell (MCFC) stack dynamic model was developed to analyze a spectrum of dynamic responses. A simplified process flow diagram of the fuel cell power plant is presented. The massive parallelism, natural fault tolerance, and implicit programming of neural network (NN) computing architectures suggest that they may be good candidates for implementing real-time controllers for complicated, nonlinear dynamic systems. To reduce the complexity of the NN model, a fuel cell power plant can be divided into three subsystems. With fewer weights for each NN model, the random influence on the fuel cell model can be lowered.

A new concept of an intelligent setpoint reference governor (I-SRG) using a heuristic algorithm will be developed to find the optimal setpoints based on system constraints and performance objectives. The NN Identification system realizes an adaptive NN identifier for the control of the MCFC. A fuel cell power plant can be interfaced with the utility system via a three-phase inverter, controlling real and

reactive power. Some of operating conflicts and the effects of distributed generation on power quality are also addressed and possible solutions are suggested. Simulation results of the matlab/simulink model of a fuel cell power plant with an inverter controller proved load tracking capability following the real and reactive power change of the load.

TABLE OF CONTENTS

LIST OF FIGURES

LIST OF TABLES

ACKNOWLEDGEMENTS

I would like to express my sincere gratitude to Prof. Kwang Y. Lee for his support and advice. I extend my sincere thanks to Prof. Heath F. Hofmann, Prof. Jeffrey S. Mayer, and Prof. Robert M. Edwards for reviewing my thesis and for their valuable comments that helped me in completing this thesis.

My appreciation also goes to my colleagues in the power systems control lab including; Myongsoo Kim, Byounghee Kim, Jin S. Heo, Nate Hobbs, Joel Van Sickel, Jason Hoffman, Wenli Yang, and Jonathon Williams. Finally, I would like to dedicate this thesis to my wife, Kyonghee Lee, son, Joonsuk Choi, and daughter, Yena Choi, for their devotions to my work.

Chapter 1

INTRODUCTION

Small scale power generating technologies, such as gas turbines, small hydro turbines, photovoltaics, wind turbines, and fuel cells, are gradually replacing conventional generating technologies in various applications of electric power system. These distributed technologies have many benefits such as high fuel efficiency, short construction lead time, modular installation, and low capital expense, which all contribute to their growing popularity. The prospect of independent ownership for distributed and other new generators, as encouraged by the current deregulation of the generation sector, further broadens their appeal. In addition, the industry restructuring process is moving the power sector away from the traditional vertical integration and cost-based regulation toward an increased exposure to market forces. Competitive structures for generation and alternative regulatory structures for transmission and distribution are emerging from this restructuring process.

For a system with distributed generation to operate reliably and efficiently, the system's operation and control strategy must accommodate both the engineering need to maintain collective system services and the economic push for independent and decentralized decision making [1].

1.1 Motivation

Recently, renewable energy sources have become more commonplace for producing electricity, fuel, and heat. This is in response to the major threats of climate

change due to pollution, exhaustion of fossil fuels, and the environmental, social and political risks of fossil fuels and nuclear power. Molten Carbonate Fuel Cells (MCFCs) are a type of a fuel cell that internally reforms methane-containing fuels within the anode compartment of the fuel cell.

For the optimized operation of a fuel cell power plant, an intelligent control method needs to be developed. Several operational requirements such as load tracking and fuel efficiency can be considered to find the optimal setpoints. New technologies such as inverters with real and reactive power control are becoming available to provide a uniform standard interconnection of distributed resources with the electric power system.

1.2 Background

1.2.1. Deregulation in Electricity Energy Markets

It has been a surprise to many Californians that the most prosperous state in the U.S. is experiencing power shortages and that the Silicon Valley is not exempt from black outs [2]. Electricity is an essential part of modern life. When supply fails to keep pace with demand, costs to consumers and businesses rise and reliability falls. The California experience demonstrates the crippling effect that electricity shortages and blackouts can have on a state or region.

Electricity demand is projected to grow sharply over the next twenty years. If the U.S. electricity demand continues to grow the high rate it has recently, even more generating capacity will be needed. To meet the future demand, the United States will have to build new power plants [2]. Over the next few years, if the demand for electricity

continues to grow as predicted and we fail to implement a comprehensive energy plan that recognizes the need to increase capacity, we can expect our electricity shortage problems to grow. The result will be higher costs and lower reliability.

1. Electricity Restructuring

To provide ample electricity supplies at reasonable prices, states are opening their retail markets to competition. This is the most recent step in a long transition from reliance on regulation to reliance on competitive forces.

The electricity industry has undergone considerable changes in the last two decades. These changes affect how our electricity infrastructure operates. Major industry restructuring has separated once vertically integrated electric utilities that supplied generation, transmission, and distribution services into distinct entities. To facilitate competition at the wholesale level, in 1996, the Federal Energy Regulatory Commission (FERC) required transmission-owning utilities to "unbundle" their transmission and power marketing functions, and provide nondiscriminatory, open access to their transmission systems by other utilities and independent power producers [2]. At the retail level, some states have required utilities to divest their generation assets as part of restructuring. These utilities currently supply only transmission and distribution services for customers who purchase electricity (i.e., generation services) from other firms.

2. Change in Wholesale Electricity Market

This transition from regulation to competition began in 1978 with enactment of the Public Utility Regulatory Policies Act, which promoted independent electricity

generation. Open-access transmission policies adopted by the FERC in the late 1980s further promoted competition in wholesale power markets.

Congress largely ratified these polices with enactment of the Energy Policy Act of 1992, which further promoted non-utility generation. FERC took another large step to promote competition with its open-access rule in 1996, which provided greater access to the transmission grid, the highway for interstate commerce in electricity [2].

3. Change in the Retail Electricity Market

Increased competition in wholesale power markets encourages states to open retail electricity markets. Under current law, FERC has jurisdiction over the wholesale power market, while states have jurisdiction over retail markets. Beginning in 1996, states began opening their retail markets to competition in order to lower electricity prices.

Most new electricity generation is being built not by regulated utilities, but by independent power producers. These companies assume the financial risk of investment in new generation, and their success rides on their ability to generate electricity at a low cost.

1.2.2. Future Energy Sources

We can look to alternative energy technologies for long term solutions. There is significant promise in these technologies to meet an ever-growing portion of the energy needs. In the long run, alternative energy technologies such as hydrogen show great

promise. Hydrogen is the most common element in the universe and can be extracted from water. Converting hydrogen into energy is compatible with existing energy technologies, such as fuel cells, engines, and combustion turbines. Hydrogen can be converted into useful energy forms efficiently and without detrimental environmental effects. Unlike other energy sources, its production by-product is water [3].

Fuel cells can produce electricity and heat from hydrogen, natural gas, and petroleum fuels. Fuel cell gases can be derived from coal and biomass. What makes fuel cells unique is that they can use fuels without combustion but by chemical reactions, making them extremely clean and efficient.

Fuel cells were developed by the National Aeronautics and Space Administration to generate electricity, heat, and water in space vehicles. The first-generation fuel cells for stationary power applications entered the commercial market in 1995. This type of fuel cell is used to generate very high-quality electricity and heat with negligible emissions in commercial and industrial settings. It is most likely to be used in cases where users are willing to pay a premium for cleaner, more reliable power than is available from the commercial grid [3].

The second generation of stationary fuel cells is currently in the demonstration phase, including a combined fuel cell-turbine hybrid. These fuel cells are expected to be more efficient and cost less when used in similar distributed energy systems [4]-[5]. Smaller fuel cells for residential units are also being developed, and some are in the demonstration phase.

Despite technical progress, high costs remain the main deterrent to widespread fuel cell use. Significant cost reductions must be achieved before fuel cells will be competitive with internal combustion engines. Additionally, the size and weight of fuel cell systems must be reduced even more to accommodate vehicle packaging requirements [3].

A significant amount of promising research and development has already been completed. The automobile industry is aggressively exploring fuel cells as the future of the industry. Moreover, a new first generation class of distributed energy technologies is already hitting the market. New developments in microturbine and fuel cell technologies are also highly promising.

Renewable energy technologies tap natural flows of energy–such as water, wind, solar, geological, and biomass sources to produce electricity, fuels, and heat. Non-hydropower renewable electricity generation is projected to grow at a faster rate than all other generation sources, except natural gas. These sources of energy are continuously renewable, can be very clean, are domestically produced, and can generate income for farmers, landowners, and others. Although its production costs generally remain higher than other sources, renewable energy has not experienced the price volatility of other energy resources.

The most important long-term challenge facing renewable energy remains the economy. Renewable energy costs are often greater than those of other energy sources. However, these costs have declined sharply in recent years, due to improved technology. If this trend continues, renewable energy growth will accelerate [3].

1.3 Statement of Purpose

Fuel cells used to generate electricity are an up-and-coming solution to the energy problem and may increase in popularity as the world moves toward the deregulation of the utility industry. The major problems in power plant operation including fuel cells are coupling problems among systems and optimization problems. To design a control system for reducing the complexity, a new approach to provide an optimal operation needs to be developed. The main object of this research is to develop an intelligent control system for a fuel cell power plant. Control systems will consist of an intelligent setpoint reference governor for the generation of optimal setpoints and an intelligent identification system for the preservation of stability.

What has made the concept of distributed power especially attractive is, of course, all of the innovative electronics that have lowered the cost of protective relaying, improved remote control, and simplified interfaces between generating resources and the grid. Even so, the difficulties of connecting distributed resources to the grid are not to be underestimated. It is necessary to gain a detailed understanding of the control schemes for an inverter interfaced distribute generation. An appropriate model for PQ controlled fuel cells will be developed to meet the requirements of the loads in grid-connected operation.

The issues of distributed generation on the grid side are also important. Unwanted flows back into the grid can be a serious threat to maintenance personnel, as well as to equipment. Design of protective relaying systems becomes much more complicated because, for example, ways must be found to feed current back into the network through

protectors designed to regulate current flowing in the opposite direction. Conversely, when a protector opens a circuit, a distributed generator might continue to feed a sub-distribution system, blowing a fuse, which would then stay open when the larger circuit recloses. Those concerned about interconnection issues still have many issues to clarify

Main research items are as follows:

1. Intelligent Control of a Fuel Cell Power Plant

- development of intelligent setpoint reference governor (I-SRG)
- development of learning system for INNS
- development of NN identifier for control

2. Interface to the Utility System

- development of inverter-based interface model
  - control scheme for an inverter interfaced fuel cell power plant
  - voltage source inverter PQ controller
  - inverter-based interface model to the utility grid
- development of matlab/simulink model for case studies

3. Operating Conflicts and Power Quality Issues

- the recommendation of operational standard to the utility and DG provider

- how to solve the problem of fault clearing, reclosing, and the interface with relaying

▪ recommendation of construction standard to the utility

- how to prevent harmonics through grounding arrangements

▪ development of remote control system for DG switches, transformer and generators

- monitoring of islanding, voltage regulation and DG transformer

▪ development of inverter-based PQ control system model

- simulation to prevent voltage flicker and voltage sags

1.4 Contributions of the Thesis

A renewed interest for distributed generation led to a considerable increase in the proportion of DG in the electric market. Generators with renewable sources became more economical, as wind or solar energy became more economically and technically feasible. In order to control distributed systems efficiently, an intelligent control scheme using a heuristic algorithms and neural networks is applied for a fuel cell power plant. Among several objective functions, load tracking and plant efficiency are solved to find optimal setpoints for the fuel cell power plant. The intelligent setpoint reference governor (I-SRG) proved its usefulness for load tracking and improvement of plant efficiency.

A new concept for intelligent controllers is proposed to mimic the function of an Intelligent Setpoint Reference Governor in generating the setpoint profile for a fuel cell power plant. In the design of control systems, a NN identifier is developed to provide

information about the plant to controllers and shows its feasibility through an evaluation using arbitrary reference input.

The introduction of distributed generation to the distribution network might be considered to bring a significant impact on the power quality conditions for the customers and utility equipment. Many of these problems can be solved using new inverter technologies including real and reactive power control and power flow simulations. Through various case studies, it is proved that the interface of a fuel cell power plant to a distribution network does not bring any significant impact to an existing network and the effective grounding of the transformer between the fuel cell and distribution network can restrict the fault current successfully during a line-to-ground fault.

1.5 Organization of the Thesis

Distributed generation technologies and their effects on deregulation in the electricity energy market are introduced in Chapter 2. Among these new technologies, fuel cells are presented as a promising technology. Four main types of fuel cells and several specific applications are introduced.

In Chapter 3, a control-oriented simulation model of a molten carbonate fuel cell (MCFC) stack is developed as part of an ongoing study of autonomous plant-wide and distributed generation control of fuel cell power plants. Designed data and parameters for the simulation are based on Fuel Cell Energy (FCE)'s 2-MW conceptual system design leading to the Santa Clara Demonstration Project (SCDP) plant.

In view of the complexity of the fuel cell model, an intelligent setpoint reference governor to achieve optimal operation is proposed in Chapter 4. Chapter 5 realizes adaptive feedback control through the use of NNs.

In chapter 6, case studies are shown of how a fuel cell power plant can be interfaced with the utility system via a three-phase inverter, controlling real and reactive power. Some of the operating conflicts and the effect of distributed generation on power quality are addressed and main research items are mentioned.

Chapter 2

FUEL CELLS FOR DISTRIBUTED GENERATION

In this Chapter, Distributed Generation (DG) technologies and fuel cell power plants as DG resources are investigated. The concept of DG has a variety of meanings, often resulting in some confusion. DG will refer to any modular generation located at or near the load center. These small, self-contained, decentralized power systems are categorized as photovoltaic, mini-hydro, and wind systems or in the form of fuel-based systems, such as fuel cells and microturbines [6]. Microturbines produce low cost electricity but at low efficiencies. Fuel cells can produce electricity from hydrogen, natural gas, and petroleum fuels without combustion or motion. This makes fuel cell DGs extremely clean and efficient.

2.1 DG Technologies

A shift in the economies of scale recently took place where smaller power plants of a few dozens MW's, instead of a few GW's, became more economical. Also, generators with renewable sources of wind or solar energy became more economically and technically feasible. This has resulted in the installation of small power plants connected to the distribution side of the network. These plants are close to the customers and hence referred to as "embedded" or "distributed" generation.

Recently, power market liberalization in Europe and North America has resulted in an increase in the number of smaller power producers participating in the electricity

market, giving rise to a renewed interest for DG. This led to a considerable increase in the proportion of DGs in the network. A study by the Electric Power Research Institute (EPRI) indicates that by 2010, 25% of new generation will be distributed [7].

The introduction of DG to the distribution system will have a significant impact on the flow of power and voltage conditions for the customers and utility equipment. These impacts might be positive or negative, depending on the distribution system's operating characteristics and the DG characteristics. Positive impacts include:

1. Voltage support and improved power quality.
2. Diversification of power sources.
3. Reduction in transmission and distribution losses.
4. Transmission and distribution capacity release.
5. Improved reliability.

However, some operating conflicts related to over-current protection, voltage regulation, power quality problems, ferroresonance, and others might result when the distributed generators are operated in parallel with the utility distribution system [8].

The International Energy Agency (IEA) identifies 5 major factors that contribute to the renewed interest in DG [9]:

1. Electricity market liberalization.
2. Developments in DG technology.
3. Constraints on the construction of new transmission lines.
4. Increased customer demand for highly reliable electricity.
5. Environmental concerns.

2.2 DG Resources

There are various types of distributed generation technologies ranging from the well-established reciprocating engines and gas turbines to more recent types of renewable sources such as wind farms and photovoltaic cells. Emerging technologies such as fuel cells and micro-turbines have just been commercialized recently. DG technologies typically fall under two main categories:

2.2.1 Combined Heat and Power

CHP plants or cogeneration plants are power plants where either electricity is the primary product and heat is used as a byproduct, or where heat is the primary product and electricity is generated as a byproduct. The overall energy efficiency is then increased. Many DG technologies, such as reciprocating engines, micro-turbines, and fuel cells, can be used as CHP plants.

2.2.2 Renewable Energy Generation

Renewable Energy Generator refers to distributed generation that uses renewable energy resources such as heat and light from the sun, wind, falling water, ocean energy and geothermal heat. The main DG technologies falling under this category are wind turbines, small and micro hydro power, photovoltaic arrays, solar thermal power, and geothermal power [8].

By relying on dispersed small-scale generators, combined with other distributed resources such as flywheel storage devices and sophisticated control equipment, utilities can avoid costly investments in large, often polluting, central plants. They can also deploy generating assets more flexibly as needed, and at the same time reduce transmission and distribution losses.

Wind and biomass are constrained by the availability of wind and land, and photovoltaics will become cost-competitive only if gas prices double. Partly for those reasons, the two candidate technologies for distributed generation that are arousing the most excitement right now are fuel cells and microturbines. Companies touting novel approaches to the design of fuel cells and microturbines have been experiencing the kind of Wall Street roller-coaster rides ordinarily reserved for companies which do most of their business on the internet. In those stories there are grounds for excitement but also some cautionary tales [10].

Microturbines and fuel cells can be deployed not only in isolation but also in combination. Marrying the two technologies could have prodigious advantages. Among the gains are overall system efficiency and recovery of pollutants, including greenhouse gases [11].

One especially promising feature of distribution generation is its ability to supply the power-hungry electronics installations that account for a substantial share of demand growth. Proponents claim that they will be able to generate electricity more cheaply and efficiently than gas-fired plant, for all usable fuels to be converted, and for carbon emissions to be fully sequestered, so that the technology essentially emits no carbon.

In Europe (where the weather conditions are erratic and the forecasts are only available for limited periods of time), the Photovoltaic (PV) system needs to be over-sized and integrated with batteries and Diesel Generator Sets (DGSs) for back-up purposes. Due to these limits, the PV has rarely been chosen as the energy supply in off-grid industrial applications which require more than a few kWh/day. The wind Generator (WG), despite of its reduced cost compared to the PV solution, has not been diffused in Europe because of the weather conditions.

The European weather conditions do not allow designing PV or WG stand-alone plants, despite the availability of these technologies for off-grid generation. Instead, the High Integrated Hybrid System (HIHS) only permits the design of a power supply system that is able to guarantee the continuity of the supply by mixing from different renewable energy sources like PV, WG (even micro-hydro if possible). This currently limits the Diesel Generator Set (DGS) use to back-up purposes only. A way to increase sustainability of the system consists of substituting the DGS backup set with a fuel cell (FC). In this way, it is possible to use the energy surplus to produce, by a hydrolysis process, the hydrogen needed for the FC. In the case of FC, the costs are higher because of the absence of a real market for FC maintenance. FC costs will be reduced in the next years because of the increase in FC production. In particular, the possibility of substituting the Diesel Generator backup group with a FC for powering isolated telecommunication devices is being investigated to improve the energy balance and provide on economic investment. Using the FC technology as a backup device makes the need for periodic maintenance and refueling operation a small burden. By using a

photovoltaic-wind-fuel cell configuration, these three technologies can provide a clean, sustainable power source [12].

2.3 Fuel Cell Fundamentals

A fuel cell is similar to a battery in that an electrochemical reaction is used to create electric current. The charge carriers can be released through an external circuit via wire connections to the anode and cathode plates of the battery or the fuel cell. The major difference between fuel cells and batteries is that batteries carry a limited supply of fuel internally as an electrolytic solution and solid materials (such as the lead acid battery that contains sulfuric acid and lead plates) or as solid dry reactants such as zinc carbon powders found in a flashlight battery. Fuel cells have similar reactions; however, the reactants are gases (hydrogen and oxygen) that are combined in a catalytic process. Since the gas reactants can be fed into the fuel cell and be constantly replenished, the unit will never be discharged like a battery.

Fuel cells generate electricity through an electro-chemical process in which the energy stored in a fuel is converted into direct current (DC) electricity. The process is similar to that of a battery. Because fuel cells generate electric energy without combusting fuel, they have many advantages. Some are as follows:

- High energy conversion efficiency
- Modular design
- Very low emissions
- Low noise

- Fuel flexibility
- Cogeneration capability
- Rapid load response, relative to conventional power generation based prime movers.

Fuel cells are electrochemical devices that convert the chemical energy of a reaction directly into electrical energy. The basic physical structure, or building block, of a fuel cell consists of an electrolyte layer in contact with a porous anode and cathode on either side. A schematic representation of a fuel cell with the reactant/product gases and the ion conduction flow directions through the cell is shown in Figure 2.1.

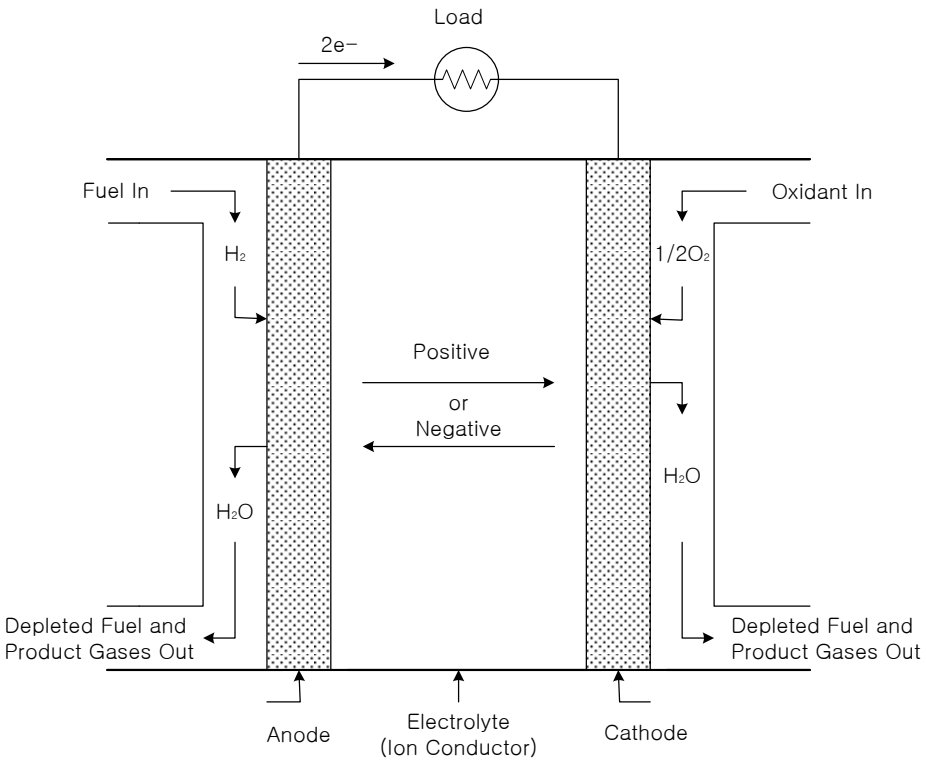

Figure 2.1. Basics of fuel cell.

In a typical fuel cell, gaseous fuels are fed continuously to the anode (negative electrode) and an oxidant (i.e., oxygen from air) is fed continuously to the cathode (positive electrode); the electrochemical reactions take place at the electrodes to produce an electric current. A fuel cell, although having components and characteristics similar to those of a typical battery, differs in several respects. The battery is an energy storage device. The maximum energy available is determined by the amount of chemical reactant stored within the battery itself. The battery will cease to produce electrical energy when the chemical reactants are consumed (i.e., discharged). In a secondary battery, the reactants are regenerated by recharging, which involves putting energy into the battery from an external source. The fuel cell, on the other hand, is an energy conversion device that theoretically has the capability of producing electrical energy for as long as fuel and oxidant are supplied to the electrodes. In reality, degradation, primarily corrosion, or malfunction of components limits the practical operating life of fuel cells.

Note that ion species and their transport direction can be different, influencing the site of water production and removal. The ion can be either a positive or a negative ion, meaning that the ion carries either a positive or negative charge (surplus or deficit of electrons). The fuel or oxidant gases flow past the surface of the anode or cathode opposite the electrolyte and generate electrical energy by the electrochemical oxidation of fuel, usually hydrogen, and the electrochemical reduction of the oxidant, usually oxygen. [13] have noted that, in theory, any substance capable of chemical oxidation that can be supplied continuously as a fluid can be burned galvanically as fuel at the anode of a fuel cell. In order to increase the rates of reactions, the electrode material should be catalytic

as well as conductive, porous rather than solid. The catalytic function of electrodes is more important in lower temperature fuel cells and less so in high temperature fuel cells because ionization reaction rates increase with temperature [14].

2.4 Types of Fuel Cells

There are four main types of fuel cells currently being developed and/or distributed. They include Phosphoric Acid Fuel Cells (PAFC), Molten Carbonate Fuel Cells (MCFC), Solid Oxide Fuel Cells (SOFC), and Proton Exchange Membrane Fuel Cells (PEMFC). Technology comparisons between these four fuel cells are outlined in Table 2.1. Zinc Air, Alkaline Fuel Cells, and Regenerative Fuel Cells are other technologies that are similar in design or output to fuel cells.

Table 2.1. Technology comparison [15].

	PAFC	**MCFC**	**SOFC**	**PEMFC**
Electrolyte	Phosphoric Acid	Molten Carbonate Salt	Ceramic	Polymer
Operating Temperature	375℉ (190℃)	1200° F (650℃)	1830℉ (1000℃)	175℉ (80℃)
Fuels	Hydrogen (H2) Reformate	H2/CO/ Reformate	H2/CO2 /CH4 Reformate	H2 Reformate
Reforming	External	External Internal	External Internal	External
Oxidant	O2/Air	CO2/O2/Air	O2/Air	O2/Air
Efficiency	40-50%	50-60%	40-80%	40-50%

Natural gas (methane) is considered to be the most readily available and cleanest fuel (next to hydrogen) for distributed generation applications, so most research for stationary power systems is focused on converting natural gas into pure hydrogen fuel. This is particularly true for low-temperature fuel cells (PEMFC and PAFC). Here, fuel reformers use a catalytic reaction process to break down the methane molecule and then separate hydrogen from carbon based gases. High temperature fuel cells such as the MCFC or the SOFC do not require a reformer since the high operating temperature of the fuel cell allows for the direct conversion of natural gas to hydrogen.

2.4.1 Phosphoric Acid Fuel Cells

Phosphoric Acid Fuel Cells (PAFC) are the most commercially developed type of fuel cell. PAFCs are being used in hospitals, nursing homes, hotels, office buildings, schools, utility power plants, and airport terminals. This type of fuel cell generates electricity at more than 40% efficiency, and 85% if co-generated heat is used. Both stationary and vehicle applications are possible. PAFCs range in size from 50 kW to 500 kW.

Developers of PAFC are targeting commercial and light industrial applications in the 100-200 kW power range, for both electric-only and cogeneration applications. For such applications, PAFC has demonstrated multiple favorable characteristics to date, including:

- Packaged systems with extremely high reliability (some have operated in the field for >9,000 hours of continuous service)
- Very low noise and vibration
- Negligible emissions

2.4.2 Molten Carbonate Fuel Cells

Molten Carbonate Fuel Cells (MCFC) promise high fuel-to-electricity efficiencies. They operate at about 1,200 degrees Fahrenheit and can reform directly. Mainly stationary devices, MCFCs range in size from 250 kW to 5 MW. Demonstration units are currently being tested.

The high efficiency and high operating temperature of MCFC units makes them most attractive for base-loaded power generation, either in electric-only or cogeneration modes.

Potential applications for MCFCs include [15]:

- Industrial
- Government facilities
- Universities
- Hospitals

2.4.3 Solid Oxide Fuel Cells

Solid Oxide Fuel Cells (SOFC) can be scaled from kW-size units to MW-size units for large high-power applications, including industrial and large-scale central electricity generating stations. They can also be use in vehicles. Power generating efficiencies in SOFCs could reach 60%, and 80% in co-generation applications.

Solid oxide fuel cells are being considered for a wide variety of applications, especially in the 5-250 kW size range [15]:

- Residential cogeneration
- Small commercial buildings
- Industrial facilities

Larger sizes in the multi-megawatt range are being considered, and would be used primarily for base-loaded utility applications.

2.4.4 Proton Exchange Membrane Fuel Cells

Proton Exchange Membrane Fuel Cells (PEMFC) operate at relatively low temperatures (i.e., about 200 degrees Fahrenheit), have high power density, and can vary output quickly. PEMFCs range in size from sub-kW to 500 kW. Both stationary and vehicle applications are available.

PEMFC technology development has been driven in large part by the automotive sector, where the PEMFCs have a compelling advantage over other fuel cell technologies in terms of their size and startup time, as shown in Table 2.2 [15].

Table 2.2. Comparison of Fuel Cell technologies [15].

Fuel Cell Technology	Peak Power Density (mW/cm^2)	Start-up Time (hours)
PAFC	~200	1-4
MCFC	~160	10+
SOFC (tubular)	150-200	5-10
SOFC (planar)	200-500	unknown
PEMFC	~700	<0.1

PEM fuel cells are currently being developed for a broad range of applications including [15]:

- Automotive
- Residential (<10 kW), both with and without cogeneration functionality
- Commercial (10 - 250 kW), both with and without cogeneration functionality
- Light industrial (250 kW and below), both with and without cogeneration functionality
- Portable power (several kW and smaller)

2.5 Applications of Fuel Cells

Fuel cells allow for a number of different types of applications, including stationary power sources, portable power sources, micro power sources, and those found in vehicles [15].

2.5.1 Stationary Power Sources

Stationary power sources are connected to the utility grid. However, these types of fuel cells have the capability of providing premium power quality that the utility grid and momentaries cannot, especially in the case of voltage sags. Dispersed small-scale generators can be combined with uninterrupted power supply (UPS) systems such as flywheel storage devices for the premium power quality. Premium power can be cleaner, less polluting, more secure, and more reliable. For these reasons, hospitals, plastic extruders, data centers, telecommunication switching centers, and cell phone towers will find fuel cell technology valuable.

Fuel cells may be used in residential homes, small commercial businesses, and larger commercial or industrial companies for emergency backup electricity, baseload/lifeline electricity, high-power quality requirements (i.e., in-home office connections), energy self-sufficiency, and remote off-grid locations. Utilities and other energy providers may also use fuel cells to ensure high customer power quality, meet transmission upgrade deferrals, and fit in with the "Green Power" market. Such distributed generation is modular, provides ease of sitting, and ensures lower capital cost [15].

2.5.2 Portable Power Sources

Portable power sources are not connected to the utility grid. These fuel cells allow consumers the opportunity for portable power for emergency equipment, hand-held power tools, and road signs [15].

2.5.3 Micro Power Sources

Like portable power sources, micro power sources are not connected to the utility grid either. These types of fuel cells have the capability of being manufactured in sizes that will comply with the smallest power requirements. Hand-held computers (i.e., 3 Whr), notebook computers (i.e., 40 Whr), and cellular telephones (i.e., 3 Whr) are a few such examples. With a great many cell phones shipped to consumers, such technological devices promise to gain consumer attention as the United States moves toward fuel cell use [15].

2.5.4 Vehicles

Fuel cells are currently being tested and marketed by many of the major automobile manufacturers. They provide an alternative to internal combustion engines, and because of their efficiency, will help reduce dependence on imported oil. Fuel cells also offer reduced vehicle emissions [15].

Chapter 3

MOLTEN CARBONATE FUEL CELL POWER PLANT OF THE SCDP

In this chapter, a model of a Direct MCFC stack is investigated as part of an ongoing study of autonomous plant-wide and distributed generation control of fuel cell power plants. The investigation is based on first principles and includes the dominant chemical reactions and simplifying assumptions used to derive the lumped parameter model. Reaction rates are included for the electrochemical reaction as well as for the reforming process. A Direct fuel cell (DFC) internally reforms methane-containing fuels into hydrogen, partially in an internal reforming unit (RU) and partially at the cells. This technology, as a mature product, has a projected net fuel-to-electricity efficiency of 55-60% and a total thermal efficiency approaching 85%.

A relatively large-scale demonstration of the MCFC technology and its commercialization potential is California's 2-MW Santa Clara Demonstration Project (SCDP). The SCDP contains 125-kW stacks of fuel cells based on DFC technology developed by Fuel Cell Energy (FCE). The DFC technology reforms natural gas into hydrogen, partially in an internal reforming unit, and partially at the cells. The control scheme of DFC power plant is based on FCE's 2-MW conceptual system design leading to the SCDP demonstration plant [16].

3.1 Principles of DFC

Conversion of fuel to a hydrogen-rich gas is conventionally carried out in an external fuel processor. In the DFC, methane-containing fuels are internally reformed

within the anode compartment of the fuel cell, which results in a simpler plant configuration with improved efficiency. The approach is a combination of indirect internal reforming (IIR) and direct internal reforming (DIR), which provides for better thermal management [17]-[19].

The basic operation of a DFC is described in Figure 3.1, taken from [38]. In the DFC, two porous electrodes are in contact with a ceramic matrix filled with molten carbonate salt as an electrolyte. Hydrogen, a fuel derived from natural gas through steam reforming, is introduced at the anode electrode while the oxidant (a mixture of O_2 and CO_2) is introduced at the cathode electrode.

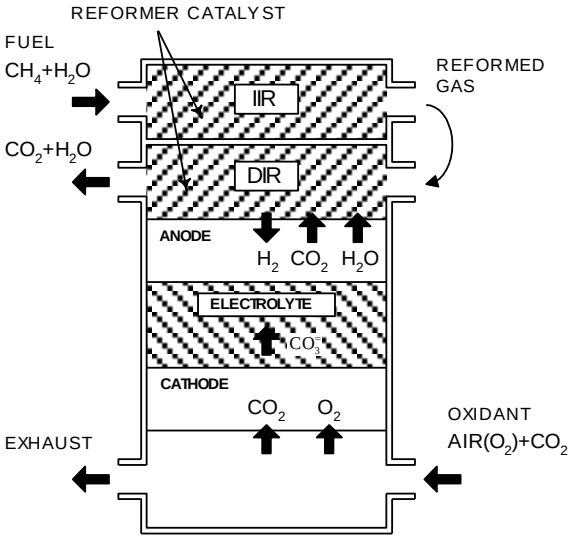

Figure 3.1. IIR/DIR structure of MCFC stack.

At the cathode electrode the oxygen and carbon dioxide in the oxidant stream undergo a reaction (nitrogen is inert) to form carbonate ions ($CO_3^{=}$). The matrix provides the ionic path for the $CO_3^{=}$ ions [27]:

$$\frac{1}{2}O_2 + CO_2 + 2e^- \rightarrow CO_3^{=} \qquad \text{Cathode} \qquad (3.1)$$

The O_2 is supplied by air and the CO_2 is made available by recycling the CO_2 from the anode compartment. This is achieved by oxidizing the anode exhaust with air in a burner.

The carbonate ions then migrate to the anode electrode through the electrolyte. The H_2 present in the fuel is reacted with carbonate ions to produce H_2O and CO_2:

$$H_2 + CO_3^{=} \rightarrow H_2O + CO_2 + 2e^- \qquad \text{Anode} \qquad (3.2)$$

For each mole of H_2 consumed at the anode, one mole of CO_2 and one mole of H_2O is produced at the anode and these gases leave the fuel cell with the anode exhaust stream.

Heat is recycled at the cathode exhaust, using a heat recovery unit, to preheat the steam-methane mixture entering the anode. In DFC technology, the following reforming chemical reactions are accomplished by placing the reforming catalyst directly in the anode of the fuel cell [20]:

$$CH_4 + H_2O \rightarrow CO + 3H_2 \qquad \text{Reforming} \qquad (3.3)$$

$$CO + H_2O \rightarrow CO_2 + H_2 \qquad \text{Water-Gas Shift} \qquad (3.4)$$

The gas-water shift reaction is assumed to be at equilibrium. This assumption imposes just an algebraic constraint on the mole fractions of species appearing in (3.4). Reactions (3.3) and (3.4) are then combined into an equivalent reforming reaction:

$$CH_4 + 2H_2O \rightarrow CO_2 + 4H_2 \qquad \text{Reforming} \tag{3.5}$$

For conciseness, both the cathode reaction (3.1) and the anode reaction (3.2) are combined into a single equation, and the stack convection losses and useful dc electrical power are identified:

$$\begin{aligned} &H_2(\text{anode}) + \tfrac{1}{2}O_2(\text{cathode}) + CO_2(\text{cathode}) \\ &\longrightarrow H_2O(\text{anode}) + CO_2(\text{anode}) + \text{Heat} + \text{Power}. \end{aligned} \tag{3.6}$$

The reaction sites are the electrodes and the voltage produced depends on the Gibb's free energy value of the fuel, the activities of the reactants, and the current drawn. Typically, a fuel cell produces less than one volt at a current that is of the order of hundreds of amperes per square foot of electrode area. Practical voltages are obtained by connection of many individual fuel cells into what is called a "cell stack." The actual performance (voltage and power) of the fuel cell for a specified current is primarily determined by partial pressures of reactants and products as well as cell temperature.

3.2 Mathematical Model of the DFC

An MCFC stack dynamic model was developed to analyze a spectrum of dynamic responses from slow to fast transients [20]. Several assumptions were made in this work: a single stack temperature, representation of mass inventory, water-gas shift reaction at equilibrium, and inclusion of appropriate kinetics for the reforming reaction.

These latter assumptions relate directly to the fast dynamics of the fuel cell stack. In [21] the model is extended by first deriving an explicit differential equation set and then representing polarization losses and temperature-dependent terms in the cell voltage. This is done by combining the basic lumped-parameter dynamic model with results from a three-dimensional cell performance model, correlated with experimental data.

A mathematical model of an internal reforming MCFC stack is developed using principles of energy and mass component balances and thermo-chemical properties. There are seven possible gas species that occur within the stack: H_2, CH_4, CO, CO_2, H_2O, N_2, O_2, where the ordering $(j = 1,2\cdots,7)$ is used to refer to individual gas species. Although these gas species don't occur simultaneously in a single location it will be convenient to define vectors implicitly representing the above ordering. There are four major reactions among the seven gas species in the DFC: the cathode reaction (3.1), the anode reaction (3.2), and the equivalent reforming reaction (3.5), whose reaction rate are denoted as r_1, r_2, and r_5, respectively.

Using the defined order at the cathode compartment, the rate vector $\vec{S}_c$ expressed in equation (3.1) can be:

$$\vec{S}_c = [0 \quad 0 \quad 0 \quad -r_1 \quad 0 \quad 0 \quad -r_1/2], \tag{3.7}$$

where the reaction rate r_1 is determined by Faraday's Law of Electrolysis [22]-[28]:

$$r_1 = \frac{-i \cdot n_{cell} A_r}{F}, \tag{3.8}$$

where i is the fuel cell current density, n_{cell} is number of cells in stack, A_r is the fuel cell active area, and F is the Faraday's constant. Since r_1 is equal to r_2, Faraday's Law (3.8) is applied to the rate vector $\vec{S}_2$ expressed in equation (3.2):

$$\vec{S}_2 = \begin{bmatrix} -r_3 & 0 & 0 & r_3 & r_3 & 0 & 0 \end{bmatrix}. \tag{3.9}$$

The rate vector $\vec{S}_5$ expressed in the equivalent reforming reaction (3.5) is

$$\vec{S}_5 = \begin{bmatrix} 4r_5 & -r_5 & 0 & r_5 & -2r_5 & 0 & 0 \end{bmatrix}. \tag{3.10}$$

At the anode compartment including the reforming unit, reactions (3.2) and (3.5) occurs. The rate vector $\vec{S}_a$ at the anode compartment is equivalently expressed:

$$\vec{S}_a = \begin{bmatrix} 4r_5 - r_3 & -r_5 & 0 & r_5 + r_3 & -2r_5 + r_3 & 0 & 0 \end{bmatrix}. \tag{3.11}$$

The equivalent reforming reaction rate r_5 follows the work presented in [29]-[31]:

$$r_5 = k \cdot p_{CH_4} \left(1 - \frac{1}{K_{Meq}} \frac{{p_{H_2}}^4 \cdot p_{CO_2}}{p_{CH_4} \cdot {p_{H_2O}}^2} \right), \tag{3.12}$$

where k is reforming rate constant and K_{Meq} is the reforming reaction equilibrium constant. The terms of p_{H_2}, p_{CO_2}, p_{CH_4}, and p_{H_2O} represent partial pressures (found by multiplying component mole fraction and total pressure) of the components H_2, CO_2, CO, and H_2O that appear in (3.5). The reforming rate constant and mass action expression are given, respectively, as [32]- [33]:

$$k = A_R A_r k_o e^{(-E/RT_s)}, \tag{3.13}$$

where k_o is a constant "frequency factor," the parameter A_R depends on total geometric cell and catalyst surface area, the constant E is an apparent activation energy for the reforming reaction, R is the universal gas constant, and T_s is stack solid average temperature. The equilibrium constant K_{Meq} is given by the general expression:

$$K_{Meq} = e^{(E_3 + E_4/T_s)}, \tag{3.14}$$

where the constants E_3 and E_4 are related to the Gibb's free energy change on the reforming reaction.

Finally, since the gas-water shift reaction is assumed to be at equilibrium, the mole fractions that appear in (3.4) are constrained by:

$$K_{Seq} = \frac{x_{CO_2} x_{H_2}}{x_{CO} x_{H_2O}}, \tag{3.15}$$

where x_{H_2}, x_{CO_2}, x_{CO}, and x_{H_2O} are the mole fractions of H_2, CO_2, CO, and H_2O, in the anode, respectively. The equilibrium constant K_{Seq} is calculated from the following equation:

$$K_{Seq} = e^{(E_1 + E_2/T^S)}, \tag{3.16}$$

and the constants E_1 and E_2 are related to Gibb's free energy change on the gas-water shift reaction [34] -[36].

The change in the concentration of each gas species that appears in (3.1)-(3.6) can be written generally in terms of input and output flows into a control volume as well as net generation due to chemical reaction. The material balance equations are written for each of the seven gas species that appear in the cathode and the anode compartments.

$$V_c \frac{d\tilde{C}_{c,j}}{dt} = N_{c,j}^{in} - N_{c,j}^{out} + S_{c,j} \ , \tag{3.17}$$

$$V_a \frac{d\tilde{C}_{a,j}}{dt} = N_{a,j}^{in} - N_{a,j}^{out} + S_{a,j} \ , \qquad \mathrm{j} = 1, \ldots, 7, \tag{3.18}$$

where $\tilde{C}_{c,j}\,(\tilde{C}_{a,j})$: cathode (anode) average molar concentration of gas species *j*,

$N_{c,j}^{in}\,(N_{a,j}^{in})$: cathode (anode) inlet molar flow rate of gas species *j*,

$N_{c,j}^{out}\,(N_{a,j}^{out})$: cathode (anode) outlet molar flow rate of gas species *j*,

$V_c\,(V_a)$: cathode (anode) compartment volume,

$S_{c,j}\,(S_{a,j})$: rate of production of gas species *j* in the cathode (anode).

The rates $S_{c,j}$ and $S_{a,j}$ are the $j-th$ element of $\vec{S}_c$ in (3.7) and $\vec{S}_a$ in (3.11), respectively. Since it is more convenient to deal with total average concentration and total flow rate, both sides of (3.17) and (3.18) are summed over all components:

$$V_\mu \frac{d}{dt} \sum_{j=1}^{7} \tilde{C}_{\mu,j} = \sum_{j=1}^{7} \left(N_{\mu,j}^{in} - N_{\mu,j}^{out} + S_{\mu,j} \right), \qquad \mu = c, a. \tag{3.19}$$

Using the definition of mole fraction as the ratio of moles of species *j* to total moles of gas mixture, the following relationships hold in the cathode and anode.

$$N_{\mu,j} = x_{\mu,j} N_\mu, \quad N_\mu \equiv \sum_{j=1}^{7} N_{\mu,j}, \tag{3.20}$$

$$\tilde{C}_{\mu,j} = x_{\mu,j} \tilde{C}_\mu, \quad \tilde{C}_\mu \equiv \sum_{j=1}^{7} \tilde{C}_{\mu,j}, \ \mu = c, a. \tag{3.21}$$

Finally, (3.20) and (3.21) are used to replace terms on (3.19), and it is assumed that the reactor is well-stirred, whereby average quantities are equal to existing quantities.

$$x_{\mu,j} \to x_{\mu,j}^{out}, \quad \tilde{C}_\mu \to \tilde{C}_\mu^{out},$$

$$V_\mu \tilde{C}_\mu^{out} \frac{dx_{\mu,j}^{out}}{dt} = N_\mu^{in}\left(x_{\mu,j}^{in} - x_{\mu,j}^{out}\right) - x_{\mu,j}^{out} \sum_{m=1}^{7} S_{\mu,m} + S_{\mu,j}, \tag{3.22}$$

$j = 1, \ldots, 7, \quad \mu = c, a.$

Each item of equation (3.22) represents a species component balance (neither individual nor total moles are generally conserved in chemical reaction) in terms of species average (or exit) mole fraction.

The rate of accumulation of total energy is divided into that of the reactor metal mass and that of the gases within the reactor volume. This equals the rate of difference in energy entering and leaving the volume minus the losses due to convection heat and useful electrical work.

$$\begin{aligned} & M_s H_s \frac{dT_s}{dt} + \sum_{j=1}^{7}\left(V_c \frac{d\bar{h}_j \tilde{C}_{c,j}}{dt} + V_a \frac{d\bar{h}_j \tilde{C}_{a,j}}{dt} \right) \\ & = \sum_{j=1}^{7}\left(\bar{h}_{c,j}^{in} N_{c,j}^{in} - \bar{h}_{c,j}^{out} N_{c,j}^{out}\right) + \sum_{j=1}^{7}\left(\bar{h}_{a,j}^{in} N_{a,j}^{in} - \bar{h}_{a,j}^{out} N_{a,j}^{out}\right) - L, \end{aligned} \tag{3.33}$$

where $M_s H_s$: stack solid mass-specific heat product,

$\bar{h}_j$: average partial molar enthalpies at stack temperature T_s ,

$\bar{h}_{c,j}^{in}$ ($\bar{h}_{a,j}^{in}$): cathode (anode) inlet average partial molar enthalpies,

$\bar{h}_{c,j}^{out}$ ($\bar{h}_{a,j}^{out}$): cathode (anode) outlet average partial molar enthalpies,

L : convection heat and electrical work.

Expanding the second term of the left-hand-side in (3.33) and using (3.17) and (3.18), the energy balance equation after rearranging becomes:

$$M_s H_s \frac{dT_s}{dt} + \sum_{j=1}^{7}\left(V_c \tilde{C}_{c,j} \frac{d\bar{h}_j}{dt} + V_a \tilde{C}_{a,j} \frac{d\bar{h}_j}{dt} \right)$$
$$= N_c^{in}\left[\sum_{j=1}^{7} x_{c,j}^{in} \left(\bar{h}_{c,j}^{in} - \bar{h}_j \right) \right] + N_a^{in}\left[\sum_{j=1}^{7} x_{a,j}^{in} \left(\bar{h}_{a,j}^{in} - \bar{h}_j \right) \right] - \sum_{j=1}^{7} \bar{h}_j \left(S_{c,j} + S_{a,j} \right) - L. \tag{3.34}$$

It is assumed that the rate of accumulation of enthalpy in the gas phase is negligible with respect to the solid components. Then, the second term of the left-hand-side in (3.34) can be neglected.

To complete the stack model dynamics, two additional state equations are used to describe anode and cathode pressure. The ideal gas law provides a simple means for replacing total concentration with measurable temperature and pressure.

$$\tilde{C}_r = \frac{P_r}{RT_r}, \tag{3.35}$$

where P_r, T_r, and $\tilde{C}_r$ are the reactor pressure, the reactor temperature, and the reactor average molar concentration of gas mixture, respectively. A dynamic equation of pressure can be obtained by differentiating the ideal gas law (3.35) with respect to time. It is assumed that stream mixture thermodynamic properties of the DFC follow the ideal gas law. Pressure models of the anode and the cathode become

$$\frac{dP_\mu}{dt} = R\left[\tilde{C}_\mu \frac{dT_s}{dt} + T_s \frac{d\tilde{C}_\mu}{dt} \right], \quad \mu = c, a. \tag{3.36}$$

The total mole concentration $\tilde{C}_\mu$ is eliminated by using (3.19) to (3.21) and at atmospheric pressure, the following version of the Nernst equation relates the electrical performance of the fuel cell to the state variables.

The model of fuel cell voltage has been represented by a static function depending only on the current regardless of whether the overall model is lumped-parameter/dynamic or two- or three-dimensional/dynamic. The Nernst equation is defined as the open voltage of the fuel cell with the standard voltage:

$$V_o = E_o + \frac{RT_s}{2F} \cdot \ln \frac{p_{a,H_2} p_{c,O_2}^{1/2} p_{c,CO_2}}{p_{a,H_2O} p_{a,CO_2}} \tag{3.37}$$

where V_o: equilibrium potential

E_o: standard potential

F : Faraday's constant

$p_{c,j}$ ($p_{a,j}$): partial pressure of gas species *j* in the cathode (anode)

Partial pressures depend on anode/cathode gas pressure and composition while standard potential is temperature dependent. Equilibrium potential is then used to find cell voltage under load current *i*:

$$V_{cell} = V_o - \eta_{act} - \eta_{conc} - iz \tag{3.38}$$

where η_{act} : activation polarization

η_{con} : concentration polarization

z : cell ohmic impedance

Current and voltage characteristics of fuel cell can be produced as shown in Figure 3.2 taken from [14] by combining the equations for each of the phenomena involved in fuel cell performance.

We refer the details of polarization and cell ohmic impedance. From the Nernst equation it is apparent that only three anode gases and two cathode gases are involved.

Anode and cathode partial pressures are required for these but have been replaced by appropriate mole fractions according to the reasoning above. Also, under the constant temperature assumption, the standard potential becomes a constant.

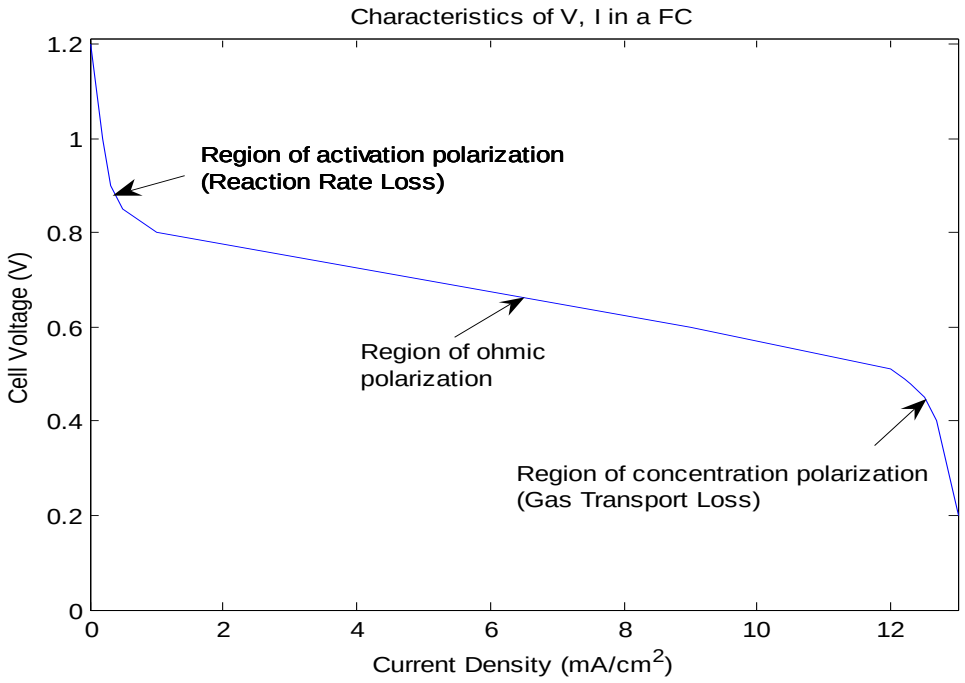

Figure 3.2. Characteristics of voltage and current in a fuel cell.

The performance of FC is affected by several operating variables of the setpoints shown in Table 3.1. Figure 3.2 shows the cell voltage as a function of the current density. The cell voltage falls rapidly on the region of activation polarization, which indicates that the fuel utilization, U_f, drops below a certain limit. If the fuel utilization increases beyond a certain value, the cell voltage also falls rapidly on the region of concentration polarization and the FC may suffer from fuel starvation and be permanently damaged.

When the current density is increased on the region of ohmic polarization, the cell voltage is decreased but the power density is increased, which means increasing the FC efficiency.

3.3 MCFC Power Plant of the SCDP

A simulation model of the Direct Reforming MCFC stack was implemented for control system applications to fuel cell power plants using the matlab/simulink software. Physical data for this model was obtained from the 2-MW system design leading to the SCDP demonstration plant and include: anode and cathode volumes, stack solid mass and specific heat, cell active area, and reforming catalyst surface area. Standard constants include the apparent activation energy for the reforming reaction and the Gibb's free energy changes on the reforming and gas-water shift reactions. Other parameters such as convection heat loss, standard reversible cell potential, and cell resistance were determined empirically.

Sixteen fuel cell stacks were used in the SCDP with each stack rated at 125-kW. For the stack, the number of cells is 258, each with a cell effective area of 4800 cm^2 and an actual area of 6000 cm^2. The distinction between effective area and actual area is necessary since part of the actual cell area is not available due to sealing at the edges. Four stacks are connected electrically in series to form a string and the system voltage is taken across a parallel connection of strings ($V_{sys} = 4 \times 258 \times V_{cell}$).

The internal reforming in the SCDP is achieved in the IIR and the DIR steps. In the IIR step, a reforming unit (RU) containing catalyst is placed between every 10 fuel

cells in the stack, converting approximately 50-60 percent of the natural gas fuel to hydrogen prior to entry into the fuel cell anode. The partially reformed natural gas undergoes further reforming (DIR step) in the fuel cell anodes, which are also loaded with reforming catalysts. This design approach ensures the benefits from the internal reforming concept, including complete conversion of the natural gas to hydrogen, reduced fuel cell heat dissipation, and simplicity in design.

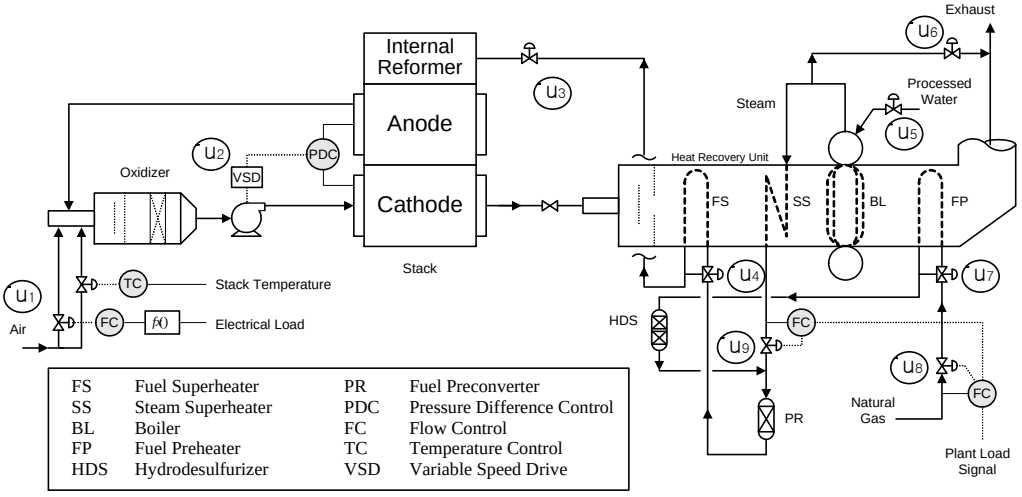

Figure 3.3. Simplified process flow diagram for the Santa Clara Demonstration Project.

A simplified process flow diagram (PFD) of the Santa Clara Demonstration Project is shown in Fig. 3.3. This consists of a lumped representation of all sixteen stacks together with the balance-of-plant (B.O.P.). A dynamic model for the SCDP including B.O.P. has been described in [37]. The principle components in the PFD are:

- Cathode gas preparation including anode exhaust oxidizer and booster blower
- Fuel processing including fuel preconverter and hydrodesulfurizer

- Heat recovery including steam generation and fuel and steam preheating

- Direct reforming (lumped) fuel cell stack

The fuel cell stack cathode exhaust gas is a mixture of CO_2, H_2O, N_2, and O_2 at a temperature of about 1250°F. The exhaust enters the heat recovery unit (HRU) and exchanges heat, in order, with the tube-side fluids of fuel superheater, steam superheater, boiler, and fuel preheater. Associated with both the fuel superheater and the fuel preheater are splitter valves used for controlling the temperature of the steam/methane fuel mixture entering the RU and the temperature of methane, respectively. Other control valves are used for boiler pressure and drum level and RU backpressure.

Fuel processing consists of both the hydrodesulfurizer and the fuel preconverter. The hydrodesulfurization reactor removes odorants and impurities from natural gas to the level required for fuel cell operation. This reactor has minimal effect on key operating conditions such as temperature and pressure because it is primarily used to remove trace amounts (parts per million, ppm) of sulfur compounds. The preconverter in the system removes higher hydrocarbons from the gas to preclude the formation of carbon in the stack during temperature transients. This is accomplished by steam reforming, (3.3) and (3.4), at lower temperature [21].

The operation and control of the SCDP is considered to produce the total stack power. Nine control points of the SCDP are also displayed as control loops from u_1 to u_9 in Figure 3.3. First, the simulation model is validated at several steady-state operating points, representative of the assumed range of operation in this part. Setpoint control laws are then derived for the proper regulation of fuel utilization and steam-carbon ratio.

Finally, the plant is subjected to cycling load changes, where all control loops are operational [38]-[39]. Table 3.1 provides a summary of the control loops along with setpoint values. We look at the individual loops in the following.

Table 3.1. Control loops in the SCDP.

Control Loop	Regulated Quantity	Setpoint (r_1~ r_{10})	Actuation (u_1~u_{10})
1	Stack Temperature	1250 ° F	Air Flow Valve
2	Stack Differential Pressure	0.012 psia	Booster Blower Speed
3	Stack RU Back Pressure	20.1 psia	Regular Valve
4	RU Inlet Temperature	Load Dependent	Fuel Superheater Bypass (Splitter Valve)
5	Steam Drum Level (Volume)	10.9 ft^3	Feedwater Flow Valve
6	Steam Drum Pressure	50 psia	Pressure Relief Valve
7	Natural Gas Temperature	700 ° F	Fuel Preheater Bypass (Splitter Valve)
8	Natural Gas Flow	Load Dependent (75% Fuel Utilization)	Flow Valve
9	Steam Flow	Load Dependent (2/1 Steam-Carbon Ratio)	Flow Valve
10	Plant DC Power	Load Dependent (Inverter Current)	PWM (pulse width modulation)

Stack temperature is regulated to prevent carbon formation and corrosion at high temperatures and degraded electrolyte properties at lower temperatures. Temperature is controlled by manipulating the amount of excess air into the oxidizer - more air results in lower temperature, and vice versa. The stack temperature setpoint is constant for all loads. The arithmetic average of cathode inlet and exhaust temperatures was the conventional measure of bulk stack temperature in the SCDP, based primarily on the much larger heat duty of the cathode.

Differential pressure between stack anode and cathode is limited to prevent gas crossover and leakage. As the variable speed driven booster blower forces more oxidant into the cathode (increasing its pressure) it draws more oxidant from the oxidizer, reducing its pressure, which draws more anode off-gas, reducing anode pressure. Thus, an increase in blower speed results in a decrease in differential pressure (anode pressure minus cathode pressure). The differential pressure setpoint is also fixed for all loads.

Splitter (bypass) valves are used for controlling both natural gas temperature (before fuel processing) and RU inlet temperature by changing the amount of bypass flow through the fuel preheater and through the fuel superheater, respectively. While the natural gas temperature setpoint is constant, the RU inlet temperature setpoint varies with load. According to the model assumptions, RU inlet temperature has an important effect on the conversion of methane to hydrogen within the RU alone. From Figure 3.3, we can see that the RU inlet temperature is equal to the fuel superheater junction temperature minus a temperature drop due to heat loss.

Drum level is controlled by varying the flow rate of processed feed water into the system through adjustment of the feed water valve. Drum pressure is controlled by adjusting the pressure relief valve. The final pressure controller in the system is the RU backpressure controller. In steady-state the RU backpressure control valve has no effect on the RU inlet flow. This can be seen by referring once again to the PFD.

Both natural gas flow and steam flow are regulated variables, implying that downstream flow (after the mixing junction) is a regulated flow. Thus, the RU backpressure valve regulates RU backpressure by increasing or decreasing pressure across the valve, although the steady-state flow through it has been fixed by upstream controllers. The two upstream flow controllers are the natural gas flow controller and the steam flow controller.

3.4 Control System for the SCDP

The control structure of the SCDP power plant is shown in the Figure 3.4, where the control system consists of SRG, nine controllers and the PCS for 10 control loops. The power conditioning system (PCS) converts Plant DC power produced by the stack array to AC power for the grid. The PCS is considered to be an ideal power converter with unity gain and first order lag dynamics. The dynamics of the stack array is adjusted by the PCS controller so that the Plant DC power responds to a 100% step change in load in about 0.05 seconds. This is consistent with the vendor design of the PCS.

The plant DC power output is forced to follow the plant DC power demand through the 9 controllers and the PCS. The SRG generates the load dependent setpoint

values in Table 3.1 according to plant DC power demand. These load dependent setpoints are r_4, r_8, r_9, and r_{10} in Figure 3.3. Other setpoints of r_1, r_2, r_3, r_5, r_6, and r_7 are the constant values represented in Table 3.1.

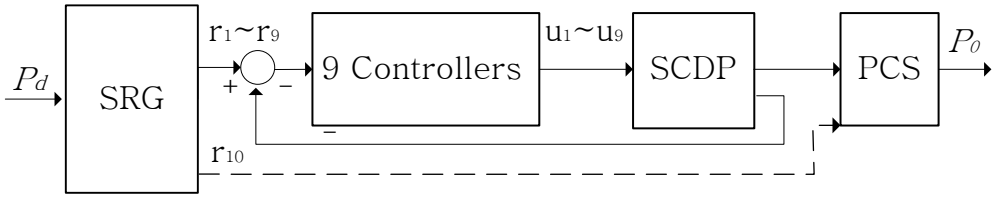

P_d : AC Power demand, P_o : AC Power Output,
SRG: Setpoint Reference Governor, PCS: Power Conditioning System,
r_1~ r_{10} : Setpoint Signals, u_1~ u_9 : Control Signals

Figure 3.4. Overall control structure of a fuel cell power plant.

Each of the nine controllers is designed on the basis of a single-loop PI controller capable of responding to the plant DC power demand. In order to avoid cheap control (large, unrealistic control action) [40], actuator constraints on all loops by limiting the control gains are observed implicitly. Generally, the PI controllers are not designed to be model-based because of nonlinear characteristics of the MCFC power plant. Control loop tuning procedures [41] are used to stabilize the nominal plant for small perturbations, followed by trial-and-error to expand the operating range.

There are details about the system control that are known only to Distributed Control System (DCS) vendors. For example, it is not known how the setpoint calculations for natural gas flow and steam flow are performed. They may be

automatically generated, or the steam flow could have been chosen to regulate the fuel utilization, leaving the natural gas flow to regulate the steam-carbon ratio. More complete information is known for some control loops, e.g., the RU inlet temperature setpoint is known for several operating points.

Five control loops; stack differential pressure, RU backpressure, steam drum volume, steam drum pressure, and natural gas temperature, are all associated with fixed setpoints given by the SRG, invariant with the plant DC power demand. The controllers associated with these control loops are therefore regulators. The SRG determines the four setpoint signal of RU Inlet Temperature, Natural Gas Flow, Steam Flow, and Stack Temperature depending on the plant DC power demand [42].

We investigate how the SRG determines the setpoints of RU Inlet Temperature, Natural Gas Flow, Steam Flow and Plant DC power according to the plant DC power demand. The setpoints of steam and natural gas flows are determined in detail in the next section. The RU inlet temperature setpoint is scheduled with the plant DC power demand. The setpoint value, known for several different power demands, is determined by steady-state optimization, taking into consideration performance goals throughout the process. For simplicity, it is assumed that the setpoint is linearly interpolated between the known, optimal setpoints. The operating range covered by the load profile includes the RU temperature setpoints: (1) rated power (1809 kW) 1056.5 °F, (2) full power (2023 kW) 1069.2 °F, (3) part load (1452 kW) 1044 °F. The RU inlet temperature is obtained from the load profile by linearly interpolating between the above temperature setpoints. Thus,

the RU inlet temperature controller is a tracking controller around this time-varying setpoint.

3.5 Setpoints of Steam and Natural Gas Flows

The setpoints of both flow controls (steam and natural gas) are based on the plant DC power demand. The molar ratio of steam to carbon entering the fuel cell is a critical variable, maintained to be roughly no smaller than 2.0 to prevent carbon formation within the stack. The magnitude of the total flow entering the fuel cell has an effect on the fuel utilization, another critical system variable. Under an assumption of a steady-state operation for a specific power level, an increase in flow into the stack anode results in a decrease in utilization. The reason is that electrochemical reaction still proceeds at the same rate, and therefore the same rate of consumption of hydrogen. But the hydrogen into the system has increased, resulting in less utilization of the available hydrogen. Thus, the flow of both natural gas and steam are a function of system load, determined by some appropriate plant load signal: power, current, throughput, etc.

In order to determine the proper flows of natural gas and steam from the net plant DC power demand in the SRG, we first need definitions for steam-carbon ratio and fuel utilization. The fuel utilization is defined as follows:

$$U_f \equiv \frac{\mathrm{H}_{2,\mathrm{in}} - \mathrm{H}_{2,\mathrm{out}}}{\mathrm{H}_{2,\mathrm{in}}} = \frac{\mathrm{H}_{2,\mathrm{consumed}}}{\mathrm{H}_{2,\mathrm{in}}} \tag{3.39}$$

where $\mathrm{H}_{2,\mathrm{in}}$ and $\mathrm{H}_{2,\mathrm{out}}$ are the molar flow rates of hydrogen at the fuel cell inlet and outlet, respectively. $\mathrm{H}_{2,\mathrm{consumed}}$ represents the rate of consumption of hydrogen in the

electrochemical reaction. $H_{2,in}$ accounts for all sources of hydrogen in an internal reforming MCFC:

$$\mathrm{H}_{2,\mathrm{in}} \equiv N_{ru}^{in}(x_{ru,H_2}^{in} + x_{ru,CO}^{in} + 4x_{ru,CH_4}^{in}) \tag{3.40}$$

where N_{ru}^{in} is the RU inlet total molar flow and the terms $x_{ru,i}^{in}$ represent RU inlet gas mole fractions.

Although both expressions for fuel utilization in (3.1) are equivalent at steady-state, only the right-most expression is applicable to transients. The right-most expression is applicable to transients, though, if we interpret $H_{2,consumed}$ as consumption at each point in time. $H_{2,consumed}$ can be eliminated using Faraday's Law for later use:

$$U_f = \frac{4 \cdot 258 \cdot I_{sys}}{2F \cdot \mathrm{H}_{2,\mathrm{in}}} \tag{3.41}$$

where F is Faraday's constant and I_{sys} is the total DC current of MCFC. F in this latter expression is equal to 96485 as a constant. Steam-carbon ratio (s/c ratio) is defined as the molar ratio of steam to methane:

$$\text{s/c ratio} \equiv \frac{x_{H_2O}}{x_{CH_4}} = \frac{N_{H_2O}}{N_{CH_4}} \tag{3.42}$$

Low fuel utilization (high concentration of reactants at the node) results in high cell voltage and implies inefficient use of available fuel. Thus, the design value of utilization is based on a compromise, and for the SCDP, is chosen as 75% over the upper power region. Steam-carbon ratio is lower-bounded in practice to avoid the formation of carbon within the fuel cell stacks. For the SCDP the s/c ratio into the fuel cell is chosen to

be no lower than 2.0. These two *degrees-of-freedom* are manipulated by two different inputs: steam and natural gas flows.

To maintain fuel utilization, the flow of reactants into the fuel cell must vary in proportion to the plant DC power load. Therefore, setpoints for steam and natural gas flows need to be determined as a function of the plant DC power demand. In addition, the setpoints should also satisfy the performance objective related to s/c ratio. Any s/c ratio greater than 2.0 is acceptable. However, as the s/c ratio increases, the plant deviates further from the design gas composition and the design efficiency. Therefore, the performance objective is set to: RU inlet s/c ratio = 2.0 as a conservative specification.

However, fuel utilization is not adequately maintained under sudden plant DC power load changes. This can be improved if both the natural gas and steam flow setpoints are determined so that the utilization and s/c ratio objectives hold during transient conditions, not just steady-state. Equation (3.39) indicates that in order to maintain fuel utilization to some value, the flow rate of equivalent hydrogen $H_{2,in}$ should be proportional to current, not proportional to the plant DC power load.

We can calculate the setpoints for steam and natural gas flows from fuel utilization of 75% and s/c ratio = 2.0. The required mass flow rate w_{ru}^{in} [lb/hr] into the RU to the molar flow rate N_{ru}^{in} [lbmol/hr]:

$$w_{ru}^{in} = N_{ru}^{in} M_{ru}^{in} \tag{3.43}$$

where M_{ru}^{in} is the average molecular weight [lb/lbmol] of the gas mixture into the RU. Combining (3.2), (3.3), and (3.5), and setting fuel utilization to 75%, a setpoint for mass flow rate into the RU is generated [38]:

$$w_{ru}^{\text{in}} = \frac{4(258)M_{pr}I_{sys}}{2F(0.75)(x_{pr,H_2} + 4x_{pr,CH_4} + x_{pr,CO})} \tag{3.44}$$

where the subscript *pr* denotes preconverter. It is known that the RU inlet gas composition is the same as the fuel preconverter exhaust gas composition. Setpoints for natural gas and steam flow still need to be determined.

From the performance objective related to s/c ratio, a second relationship is obtained:

$$2 = \frac{x_{pr,H_2O}}{x_{pr,CH_4}} \cong \frac{x_{pr,H_2O}^{in}}{x_{pr,CH_4}^{in}} = \frac{N_{steam}}{N_{nat\ gas}} = \frac{w_{steam}\text{M}_{\text{CH}_4}}{w_{nat\ gas}\text{M}_{\text{H}_2\text{O}}} \Rightarrow w_{steam} = \frac{2M_{H_2O}}{M_{CH_4}} w_{nat\ \text{gas}} \tag{3.45}$$

where it is assumed that natural gas is pure CH_4 (in practice about 95% by volume).

Equation (3.7) states that the location of the desired s/c ratio is at the preconverter exhaust (same as RU inlet) but this value is different from the s/c ratio before the preconverter due to chemical reaction within the preconverter. Justification for the approximation in (3.45) will follow subsequently. Also, gas composition is needed for terms in both numerator and denominator of (3.44) but is immeasurable on-line. Furthermore, the gas composition within the preconverter changes as the reactor temperature (affecting both the reforming and WGS equilibrium conversion), pressure (affects the reforming equilibrium conversion), and inlet composition change. Preconverter inlet temperature changes very slowly due to slow changes in cathode exhaust temperature and its effect on steam temperature.

A relationship between natural gas flow and steam flow results from static mass conservation:

$$w_{ru}^{in} = w_{steam} + w_{nat\ gas} \tag{3.46}$$

Substituting nominal values for the immeasurable variables and using (3.44) to (3.46), a setpoint for natural gas flow can be determined [38]:

$$w_{nat\ gas} = \frac{4(258)\overline{M_{pr}} I_{sys}}{2F(0.75)(1+2\mathrm{M}_{\mathrm{H_2O}}/\mathrm{M}_{\mathrm{CH_4}})(\overline{x_{pr,H_2}} + 4\overline{x_{pr,CH_4}} + \overline{x_{pr,CO}})} \tag{3.47}$$

where the "bar" denotes nominal value. The setpoint for steam flow rate then follows from (3.45). Note that the calculated setpoints for both natural gas and steam are properly in terms of measurable mass flow rates. Using these setpoints instead of the ones earlier, the utilization is much better behaved during the load disturbance transient, as compared to the case of load-dependent setpoints.

Chapter 4

INTELLIGENT CONTROL OF A FUEL CELL POWER PLANT

The major problem of a complex fuel cell power plant is optimization in operation. To reduce the complexity and provide optimal operation, an intelligent control will be developed. An intelligent setpoint reference governor (I-SRG) using a Particle Swarm Optimization (PSO) algorithm will be developed to find the optimal setpoints based on system constraints and performance objectives. This I-SRG will be implemented with a neural network to generate the setpoint profile and feedforward control inputs for the plant's DC power demand.

For the design of the I-SRG, the operating ranges of setpoints are considered to correspond to operation over the 70-100% load region of the maximum Plant DC power in the SCDP. This is because supplemental burning of natural gas at low power is necessary to maintain system temperature. For the maximum ramp rate of electrical load, a typical utility specification on desired ramp rate in grid-connected mode is around 10 %/min. The SCDP model shows that the plant, at least numerically, can be operated under automatic control during load cycling for ramp rate equal to 10 %/min.

4.1 Intelligent SGR with Feedforward Controller

In order to control distributed systems efficiently, a coordinated control scheme can be applied for a fuel cell power plant. A fuel cell power plant can be divided into three subsystems and each subsystem can be controlled in a distributed manner, called a coordinated control scheme. In a coordinated control scheme, the setpoints are required

for control loops [43]-[60]. The present system utilizes a nonlinear function which maps the plant DC power demand to load dependent setpoints of natural gas flow, steam flow, and RU inlet temperature. However, setpoints obtained by a fixed nonlinear function cannot provide optimal power plant operation. In other words, the nonlinear mapping function does not provide optimal power plant operation when the plant DC power demand is changed.

Therefore, an I-SRG will be proposed to generate an optimal mapping between the plant DC power demand and setpoints. In spite of the complexity of the system, a fuel cell power plant needs to be optimized mathematically under many conflicting requirements. To find the optimal setpoints for a plant, several conflicting operational requirements can be considered such as the plant DC power demand tracking, minimization of fuel consumption and heat loss rate, maximization of lifetime, minimization of pollutant emissions, etc. A multi-objective optimization problem in generating optimal setpoints will be solved to satisfy these conflicting requirements.

Due to the large stack thermal time constant, there is a significant delay in compensating control in a fuel cell power plant. It is desirable, thus, that PI feedback control is supplemented by additional feedforward control, which can give the advantage that a rapid change in control signal is possible, enabling a much tighter control than a slow feedback alone. The feedforward and feedback control for a fuel cell power plant are shown in Figure 4.1, where P_d and P_o is the plant DC power demand and the plant DC power output. The I-SRG contains the feedforward controllers, whose outputs are represented as $f_1 \sim f_9$. The output of the SCDP is fed back to the feedback controller,

which regulates the output variations due to load disturbances and compensates for the variation in the plant DC power demand.

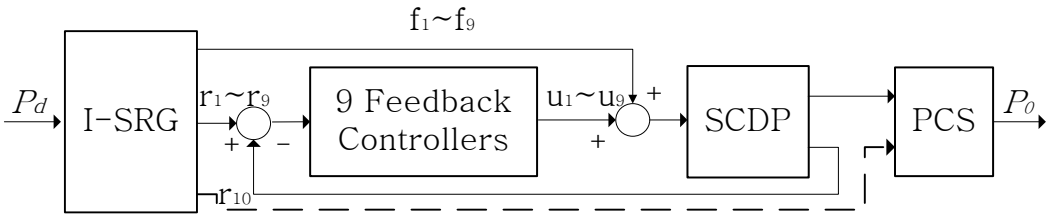

P_d : AC Power demand, P_o : AC Power Output,
I-SRG: Intelligent Setpoint Reference Governor,
PCS: Power Conditioning System, r_1~ r_{10} : Setpoint Signals,
u_1~ u_9 : Feedback Control Signals, f_1~ f_9 : Feedforward Control Signals

Figure 4.1. Overall control structure with I-SRG.

There are various performance objective functions, among which minimization of load-tracking error and fuel consumption are the most important issues to the fuel cell power plant for DG. In the SCDP power plant, the optimization objectives are considered for the plant DC power demand tracking and minimization of fuel consumption. This multi-objective optimization results in giving the setpoints of the Plant DC power and the RU inlet temperature, which are used to design the feedforward controllers. The multi-objective optimization is performed in objective functions of the I-SRG. By the optimization results, the I-SRG generates not only the load dependent setpoints of RU Inlet Temperature, Natural Gas Flow, Steam Flow and Plant DC power (r_4, r_8, r_9, and r_{10}) but also the nine feedforward control inputs (f_1 ~ f_9).

4.2 PSO Algorithm for the Development of I-SRG

For multi-objective optimization problem, optimization techniques will be applied to search for the optimal solution in the I-SRG. Standard optimization methods for Multi-Input Multi-Output nonlinear system require a heavy computational time to generate the optimal setpoints. Since traditional optimization techniques may often become computationally unattractive or even unacceptable, new optimization techniques need to be applied. As an alternative approach, an I-SRG can be developed using modern heuristic optimization techniques, such as Differential Evolutionary algorithm (DE), Genetic Algorithm (GA) and particle swarm optimization technique (PSO). Among those techniques, PSO algorithm will be used to solve the objective optimization problem, as it can provide a high quality solution with simple implementation and fast convergence [61].

The PSO is introduced briefly in Figure 4.2. Basically, the PSO was developed through simulation of birds flocking in two-dimensional space [61]. The position of each bird (called particle) is represented by a point in the X-Y coordinates and also the velocity is similarly defined. The flocking birds are assumed to optimize a certain objective function.

Each particle knows its best value and current position so far. This information is an analogy of the personal experience of a particle. Moreover, each particle knows the best value so far in the group among the best values of all particles. It is an analogy of a particle knowing how other particles around it have performed. Each particle tries to modify its position using the concept of velocity.

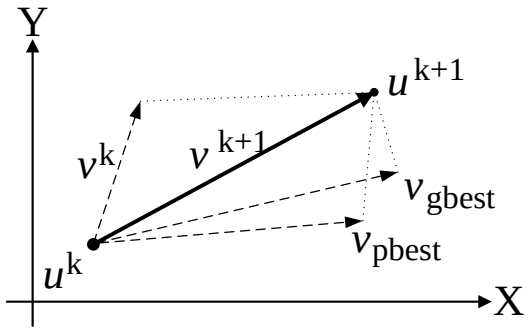

Figure 4.2. The concept of a search point by PSO.

Let $f:\Re^m \to \Re$ be the objective function. There are *n* particles at iteration $k = 1,2,\cdots,$ each with associated positions $\vec{u}_i^{\,k} = (u_{i,1}^k, u_{i,2}^k, \ldots, u_{i,m}^k) \in \Re^m$ and velocities $\vec{v}_i^{\,k} = (v_{i,1}^k, v_{i,2}^k, \ldots, v_{i,m}^k) \in \Re^m,\ i = 1,\cdots,n$. The new position of each particle is computed by adding the new velocity vector to the current position:

$$\vec{u}_i^{\,k+1} = \vec{u}_i^{\,k} + \vec{v}_i^{\,k+1}. \tag{4.1}$$

The new velocity of each particle can be updated:

$$\vec{v}_i^{\,k+1} = w\vec{v}_i^{\,k} + c_1\vec{r}_1^{\,k} \circ (\vec{u}_i^{\,*k} - \vec{u}_i^{\,k}) + c_2\vec{r}_2^{\,k} \circ (\vec{u}^{\,*} - \vec{u}_i^{\,k}), \tag{4.2}$$

where w is weighting function, c_1 and c_2 are weighting factors, $\vec{r}_1^{\,k}$ and $\vec{r}_2^{\,k}$ are two random vectors that are generally uniform random numbers between 0 and 1 with each component. The operator "∘" indicates element-by-element multiplication. Usually *c*1 and *c*2 are taken around 2. Let $\vec{u}_i^{\,*k}$ be the current best position of each particle and let $\vec{u}^{\,*} = (u_1^*, u_2^*, \ldots, u_m^*)$ be the global best among $\vec{u}_i^{\,*k}$.

$$\vec{u}^{*} = \min_{\vec{u}_i} f(\vec{u}_i^{*k}) \quad \text{for} \quad i = 1, \cdots, n. \tag{4.3}$$

Initialize $\vec{u}_i^{*0} = \vec{u}_i^{0}$ and $\vec{v}_i^{0}$ for all *i*. One common choice is to take $a_j \le u_{i,j}^{0} \le b_j$ and the concept of a search point by PSO $\vec{v}_i^{0} = \vec{0}$ for all *i* and $j = 1, \cdots, m$, where a_j, b_j are the limits of the search domain in each dimension. At iteration $k(\ge 1)$, the current best positions are updated and the global best position at iteration (k+1) is modified by using (4.3) with $\vec{u}_i^{*k+1}$.

The first term in the right-hand side of (4.2) is for diversification in the search procedure, which keeps on trying to explore new areas. The second and third terms are for intensification in the search procedure. They help in moving toward the $\vec{u}_i^{*k}$ and/or $\vec{u}^{*}$. The method has a well-balanced mechanism to utilize diversification and intensification efficiently in a search procedure. The following weighting function in (4.4) is usually utilized:

$$w = w_{max} - ((w_{max} - w_{min}) / (iter_{max})) \times iter, \tag{4.4}$$

where w_{max} is the initial weight, w_{min} is the final weight, $iter_{max}$ is the maximum iteration number, and *iter* is the current iteration number. Using above equations, a certain velocity which gradually brings particles close to their current best positions and the global best position can be calculated.

4.3 Implementation of the I-SRG

Among 10 setpoints of the SCDP in Table 3.1, 4 setpoints are load-dependent such as RU Inlet Temperature, Natural Gas Flow, Steam Flow, and Plant DC power. The

fuel utilization U_f and the steam-carbon ratio (s/c ratio) are set to 75% and 2.0, respectively for the SCDP as a conservative specification. Then, Steam Flow and Natural Gas Flow can be calculated as (3.42) and (3.47), from a given plant DC power. Therefore, optimization of setpoints for RU Inlet Temperature and Plant DC power will be considered to solve the multi-objective optimization problem.

The function of the I-SRG is to design optimal mappings from the plant DC power demand to the setpoints of RU Inlet Temperature and Plant DC power. Setpoint mappings are designed by solving a multi-objective optimization problem that takes into account the specified operational objectives and the steady-state model of the plant. The I-SRG can be realized by finding all feasible operating points which satisfy all imposed constraints. When the system response is in steady-state, the admissible power outputs can be obtained within appropriate performance of objective optimization requirements.

The I-SRG performs the design process in three steps shown in Figure 4.3.

• Determination of the feasibility regions $(\Omega_1,\Omega_2,\ldots,\Omega_{10})$ for the decision variables $\vec{u}=(u_1,u_2,\ldots,u_{10})$

• Solution of the multi-objective optimization problem to find optimal steady-state control inputs $\vec{u}^*=(u_1^*,u_2^*,\ldots,u_{10}^*)$

• Calculation of the RU Inlet Temperature and Plant DC power setpoints through the evaluation of the steady-state model of the unit.

The decision variables are candidate steady-state control inputs for control valves, $\vec{u}=(u_1,u_2,\ldots,u_{10})$ which are shown in Table 3.1.

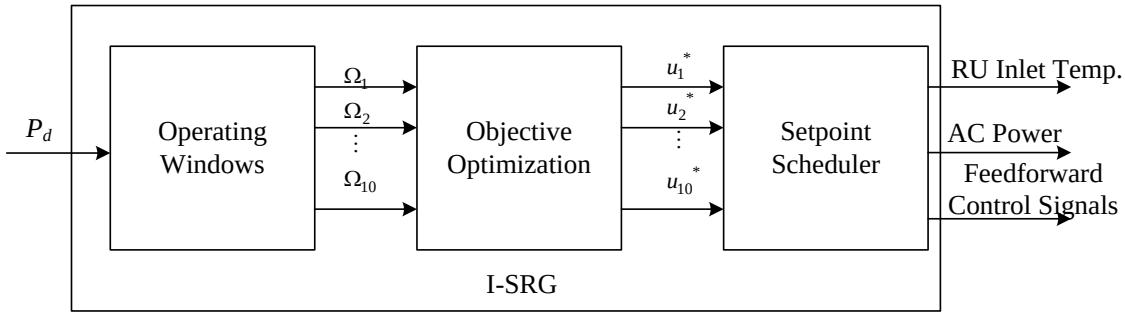

Figure 4.3. Configuration of the I-SRG.

To obtain feasibility regions $(\Omega_1, \Omega_2, \ldots, \Omega_{10})$, the value of the plant DC power demand is changed from 70% (1,498 kW) to 100% (2,128 kW) by 5% (106 kW). The maximum temperature of the stack is limited to 1,250 °F and the temperature of the rated power is set to 1056.5°F. For every 5% of power, the effective range of RU Inlet Temperature is set below 1,250 °F and changed by 10 °F. For every temperature setpoint, the fuel utilization is set to 75%. In order to obtain the steady state value for setpoints, the plant simulation model was run for 20,000 sec. The operating range of RU Inlet Temperature is found to be 730 ~ 1,130 °F for desired power demands. Fig. 4.4 shows the Power-control input operating windows, where each one is normalized corresponding to the full power range.

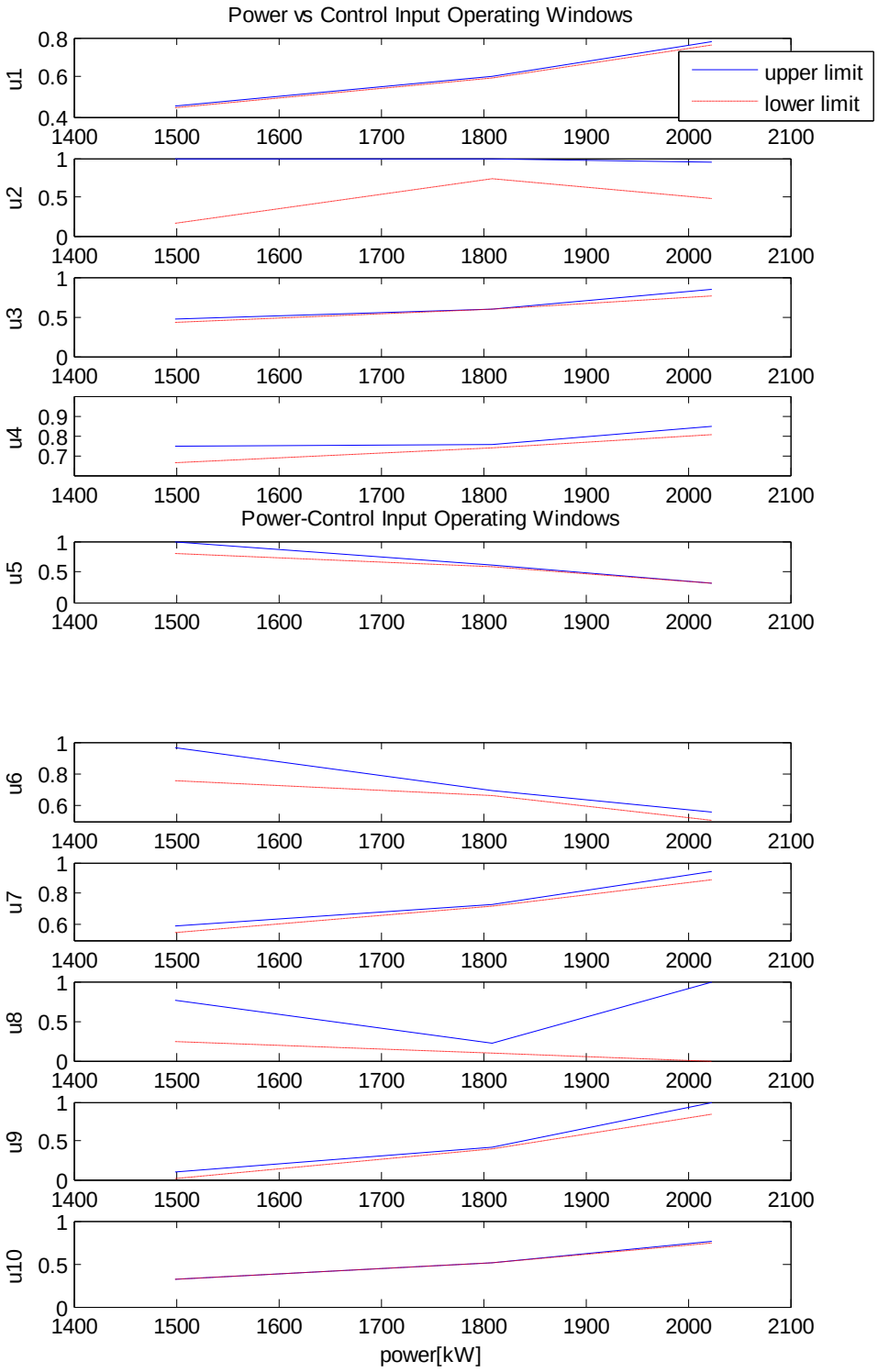

Figure 4.4. Power-control input operating windows

For the first step, it is necessary to find the steady-state model for calculation of the setpoints by using the obtained feasibility regions $(\Omega_1,\Omega_2,\ldots,\Omega_{10})$. A Neural Network modeling which is known to make the best approximation for nonlinear systems can be used to generate the steady-state models as follows:

$$\textit{Power:}\quad E(\vec{u}) = E(u_1,u_2,\ldots,u_{10}) \tag{4.5}$$

$$\textit{RU Inlet Temperature:}\quad T(\vec{u}) = T(u_1,u_2,\ldots,u_{10}) \tag{4.6}$$

In most control applications, the real-time implementation is very important, and thus the neuro-controller also needs to be designed such that it converges with a relatively small number of training cycles. Since this model is a static mapping rather than dynamic response, the network model can be simplified to a feedforward NN. In the network, 21 neurons are used for the hidden layer neuron by a rule of thumb, and it showed fast convergence within 2,000 iterations.

Fig. 4.5 shows the validation of NN setpoint scheduler for Plant DC power and RU Inlet Temperature. Performances represent successful results, showing very small errors between the steady-state output responses and the estimated values of setpoint scheduler.

For the second step, the optimal solution, $u_1^*,u_2^*,\ldots,u_{10}^*$, is found using the PSO, which is processed to solve the multi-objective optimization for load tracking and fuel conservation. In this thesis, an objective function for minimization of load-tracking error is formulated as follows:

$$J_1(\vec{u}) = \mid P_d - E(\vec{u}) \mid . \tag{4.7}$$

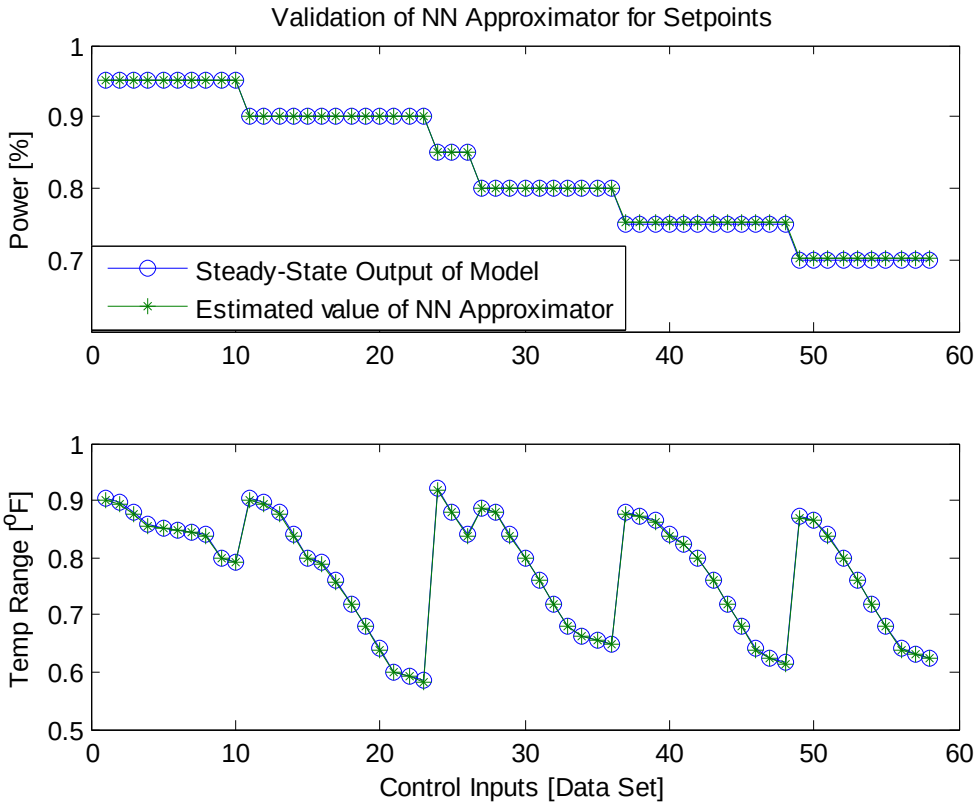

Figure 4.5. Validation of NN approximation for setpoints.

The plant DC power setpoint $E(\vec{u})$ can track to the plant DC power demand (P_d) as closely as possible by minimizing the objective function $J_1(\vec{u})$. With the operating windows and performance objective function (4.7), the PSO technique will be used to find the optimal inputs $\vec{u}^*$.

The plant efficiency can be defined as follows:

$$\eta = \frac{P_o}{P_{fuel}}, \quad P_{fuel} = M_{CH_4} \cdot LHV_{CH_4} \cdot N = 800\,N\,, \tag{4.8}$$

where N is the molar flow of natural gas, M_{CH_4}=16 kg/kmol, and Lower Heating Value LHV_{CH_4}=50[3] kJ/kg. An objective function for the plant efficiency is formulated as follows:

$$J_2(\vec{u}) = u_7, \tag{4.9}$$

where u_7 is the natural gas flow control input. $J_2(\vec{u})$ is required to be minimized to increase the plant efficiency.

In the multi-objective optimization, the objective functions are often in conflict with one another when performing the optimization. Thus, it is proposed to minimize the maximum deviation of the objective functions instead of directly minimizing the multi-objective functions [65]. The maximum deviation of multi-objective functions is defined as follows:

$$\delta_m = \max_{i=1,2} \delta_i, \quad \delta_i \geq 0, \tag{4.10}$$

$$\delta_i = \beta_i \mid J_i(\vec{u}) - J_i(\vec{u})^* \mid, \quad i = 1,2, \quad \vec{u} \in \Omega, \tag{4.11}$$

$$J_i(\vec{u})^* = \min\{ J_i(\vec{u}) ; \vec{u} \in \Omega \}, \quad i = 1,2. \tag{4.12}$$

Here δ_m is the maximum deviation of the multi-objective functions, δ_i is the weighted deviation, β_i is the preference value, $J_i(\vec{u})^*$ is the minimum possible value of the single objective function J_i, and Ω is the solution space. The preference values give the relative priorities of the objectives in searching for the optimal solution.

The PSO algorithm is used to solve the multi-objective optimization problem (4.11) with a given vector of preference value $\vec{\beta} = [\beta_1, \beta_2]$. After finding the optimal

solution, $\vec{u}^* = (u_1^*, u_2^*, \ldots, u_{10}^*)$, the setpoint scheduler is applied to map the optimal solution into Plant DC power $E(\vec{u}^*)$ and RU Inlet Temperature $T(\vec{u}^*)$. Finally, the setpoint scheduler outputs the optimal solution ($u_1^* \sim u_9^*$) as the feedforward control input ($f_1 \sim f_9$).

4.4 Simulations of the I-SRG

A plant DC power demand profile for the I-SRG operation is given in Figure 4.6. The plant DC power demand profile has different rising and falling slopes and levels of constant powers. By using the power-control input operating windows of Figure 4.4, the solution spaces $(\Omega_1, \Omega_2, \ldots, \Omega_{10})$ can be generated with respect to the plant DC power demand profile. Figure 4.7 shows the generated solution spaces $(\Omega_1, \Omega_2, \ldots, \Omega_{10})$.

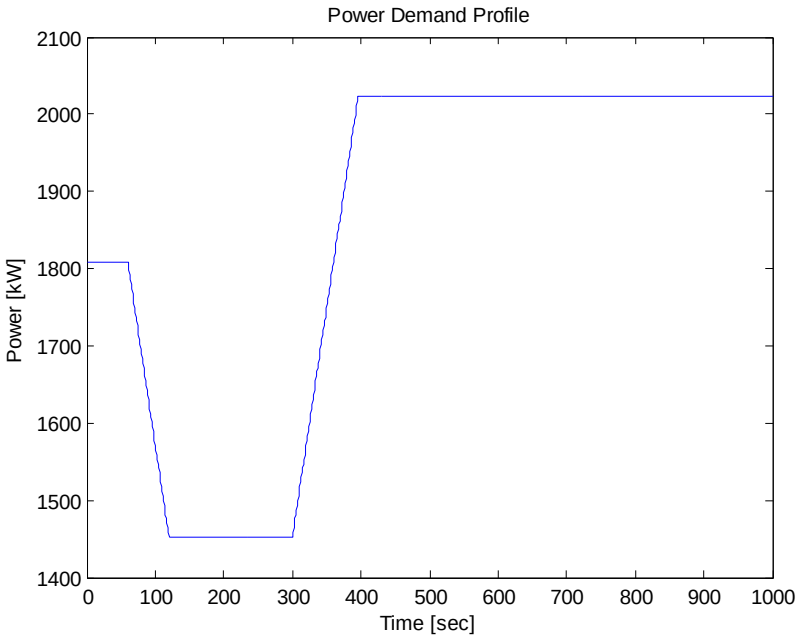

Figure 4.6. The plant DC power demand profile.

The I-SRG is operated on the given plant DC power demand profile with two different cases.

- Case 1: minimize $J_1(\vec{u})$
- Case 2: minimize $J_1(\vec{u})$, $J_2(\vec{u})$.

The Case 1 means $\vec{\beta}$ =[1, 0], and in the Case 2, $\vec{\beta}$ is set to [1, 0.001] to put more weights on the load tracking than plant efficiency objective. The PSO is processed for the multi-objective optimization with predefined objective functions and the preference values.

The plant DC power and RU Inlet Temperature setpoints are obtained by the I-SRG and they are shown in Figure 4.8 and Figure 4.9, respectively. The plant DC power setpoint $E(\vec{u}^*)$ are almost the same for both cases as the plant DC power demand of Figure 4.6. However, the conflicting requirements cause slight difference between the plant DC power setpoint and the plant DC power demand. The RU Inlet Temperature setpoint $T(\vec{u}^*)$ in Figure 4.9 is mapped for a different number of objective functions. Different temperatures of RU can produce the same amount of power. All the plant DC power setpoint results show that the I-SRG can perform well in the multi-objective optimization problem since the temperature setpoints need to be adopted only when the unit load demand is changed during the load cycle.

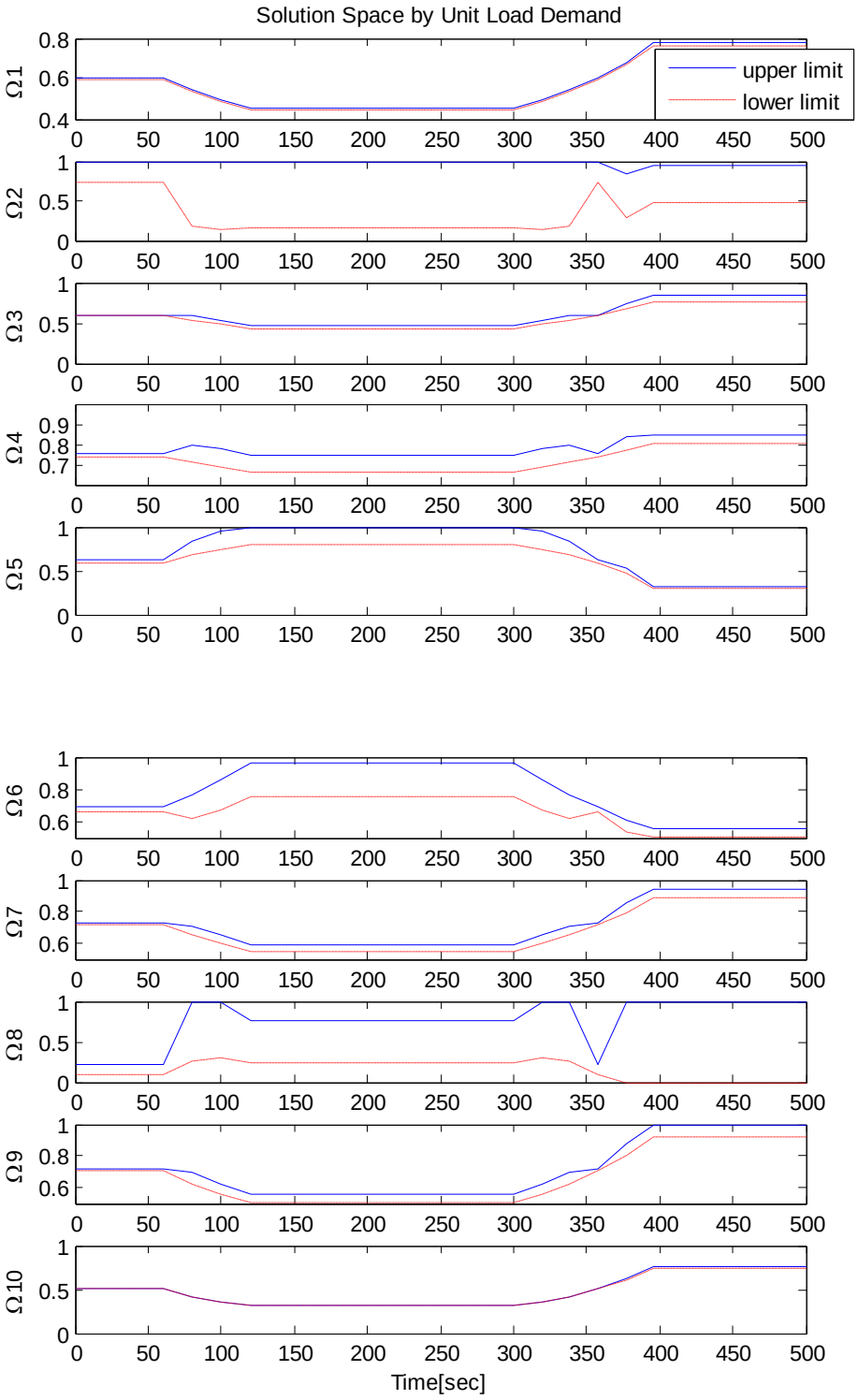

Figure 4.7. Solution space by the given plant DC power demand.

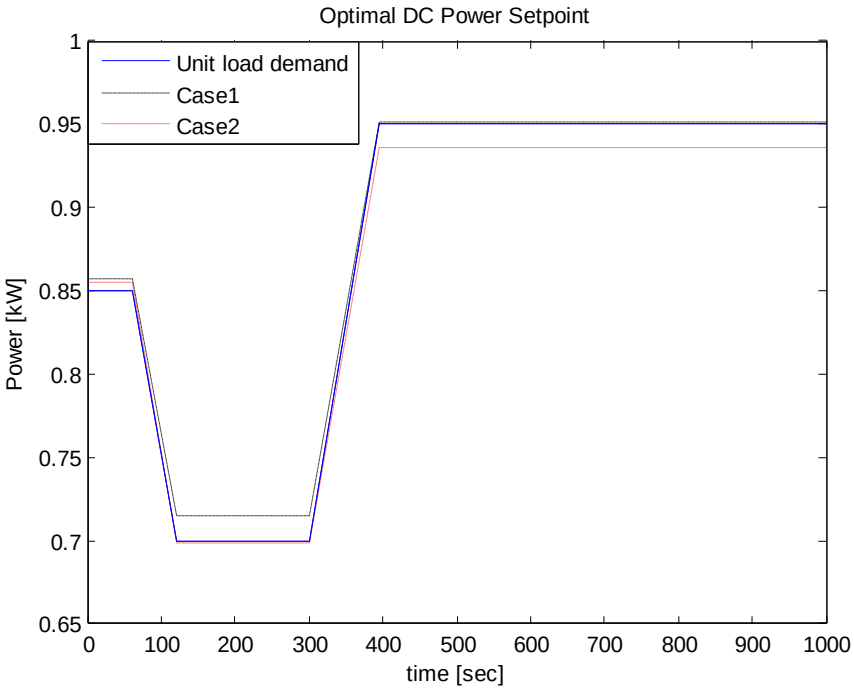

Figure 4.8. Plant DC power setpoint trajectories (70-100%).

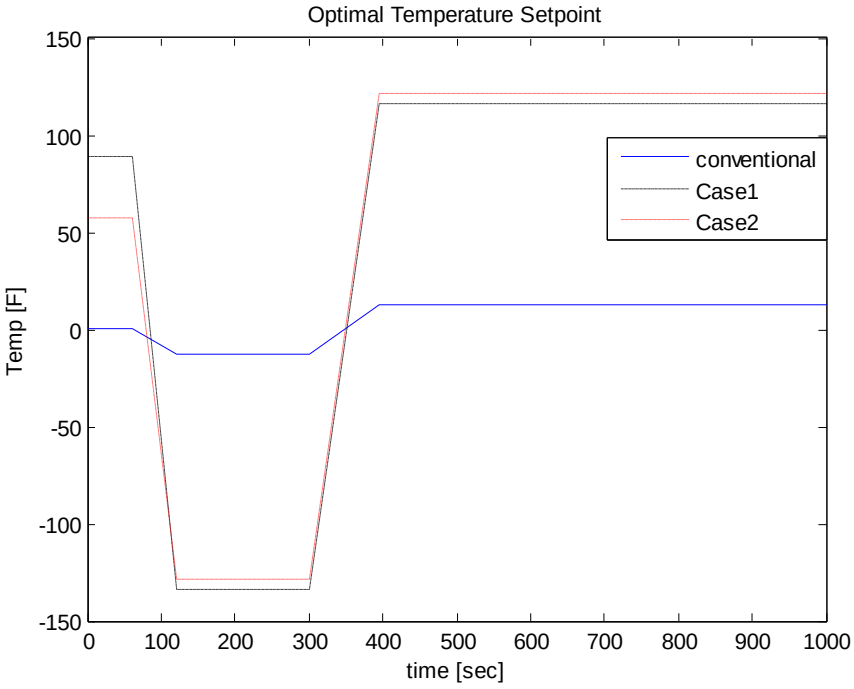

Figure 4.9. RU Inlet temperature setpoint trajectories.

The SCDP power plant is simulated with the obtained setpoints $E(\vec{u}^*), T(\vec{u}^*)$ and feedforward control inputs $f_1 \sim f_9$. The plant DC Power output (P_o) and RU Inlet Temperature output (T_o) are calculated from the simulation. Fig. 4.10 shows the plant DC power demand and the output, which proves satisfactory results for load tracking. RU Inlet Temperature outputs are shown in Fig. 4.11.

When the RU temperature setpoints are varied in Case 1, stack temperature outputs were close to the conventional ones. However, when two setpoints with additional fuel utilization setpoint (U_f) are varied, stack temperature showed some fluctuations being different from conventional ones. As shown in Figure 4.12 of the simulation results, the plant efficiency of the fuel cell power plant can be improved by using the I-SRG. When two setpoints (RU Inlet temperature T_d and fuel utilization U_f) are varied to use the I-SRG, the plant efficiency was improved significantly as shown in the figure. However, some control inputs showed abnormal values, which seems to be caused by the fact that parameters of this mathematical simulation model are not exact expressions but approximates. Therefore, only RU temperature setpoints are tried to be varied to improve the plant efficiency in this simulation model. In real power plant, however, if the control inputs allow admissible values, the setpoint of fuel utilization could be varied to improve the plant efficiency to expected levels.

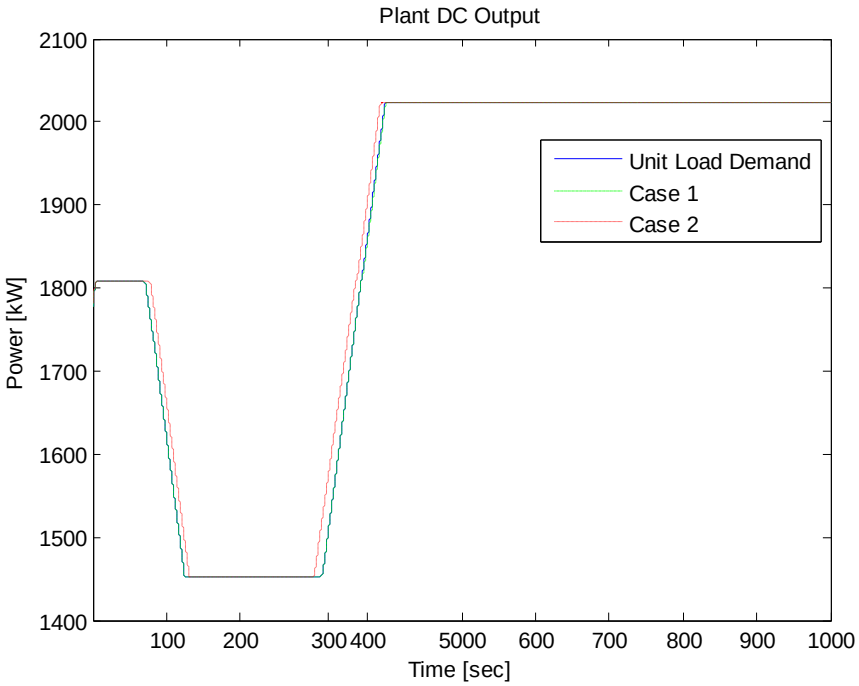

Figure 4.10. Plant DC power outputs of the simulation results.

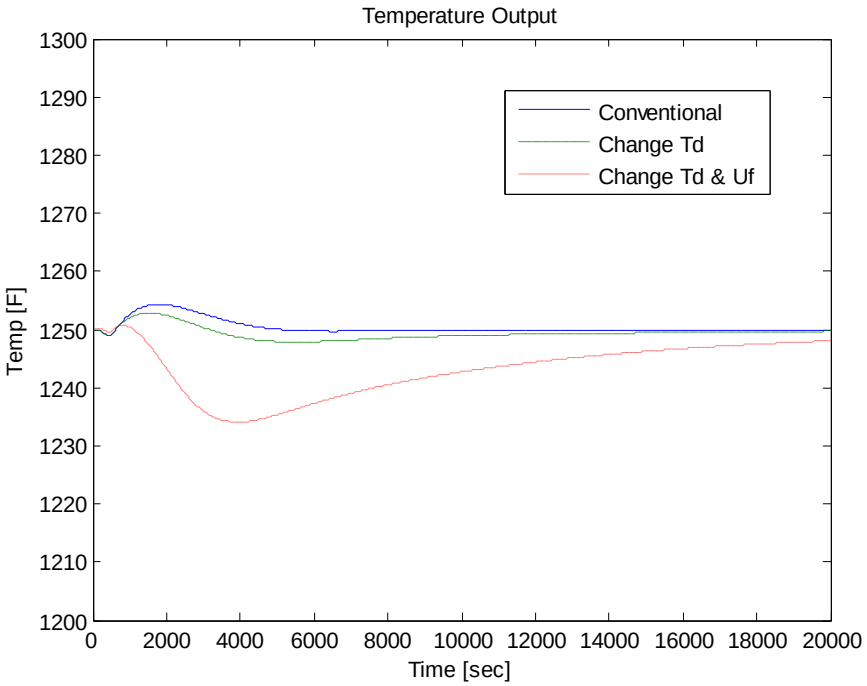

Figure 4.11. RU Inlet temperature outputs of the simulation results.

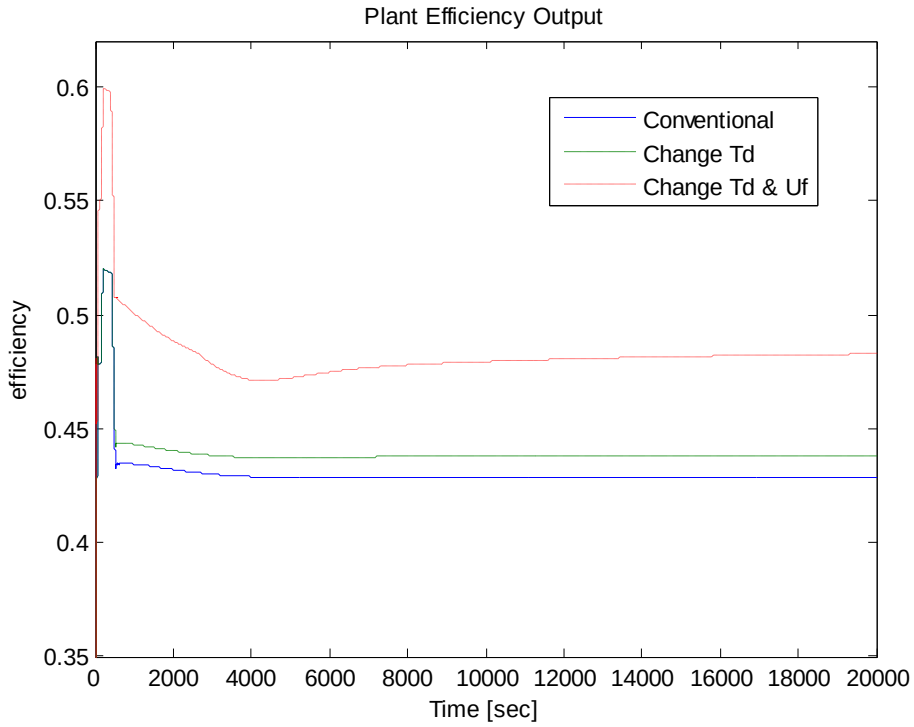

Figure 4.12. Comparison of Fuel Cell Efficiency.

4.5 Implementation of Intelligent Neural Network Supervisor

The development in control has been fueled by three major needs: the need to deal with increasingly complex systems, the need to accomplish increasingly demanding design requirements, and the need to attain these requirements with less precise advanced knowledge of the plant and environment [62]. The recent revival in neuro-engineering research, which started in the early 1980's, has focused mainly in the field of pattern recognition and signal processing. Only a few efforts have dealt with applications to control engineering [63]. The massive parallelism, natural fault tolerance and implicit programming of neural network computing architectures suggest that they may be good

candidates for implementing real-time controllers for large-scale, nonlinear dynamic systems [64].

Since a recurrent neuron already has an internal feedback loop, it captures the dynamic response of a system without external feedback through tapped delays; thus the network model can be simplified. In most control applications, the real-time implementation is very important, and thus the neuro-controller also needs to be designed such that it converges with a relatively small number of training cycles. In view of the complexity of the fuel cell model, it is proposed to adopt the recurrent neural network as the possible candidate architecture for the neural network controller.

A new concept of intelligent controller, Intelligent Neural Network Supervisor (INNS), is proposed to mimic the function of I-SRG in generating the set point profile and feedforward control signals for a fuel cell power plant. The INNS is developed for the asynchronous computation and on-line adaptive identification. The I-SRG generates setpoints for a given load profile and generates feedforward control signals corresponding to the setpoints provided by itself. Since a heuristic algorithm, for instance PSO, requires considerable computation time, the optimization can be done off-line and the resulting mappings can be learned by a neural network for on-line application.

Since the fuel cell power plant model is a simple approximate of the real power plant, model parameters are only estimates. Therefore, since the INNS is trained based on the nominal model used in the optimization, the real time adjustment of the INNS is almost inevitable in achieving the performance objectives. The configuration of the

learning system for off-line and on-line adjustment of the INNS is shown in Figures 4.13 and 4.14, respectively.

When the output of the system is not matching the setpoint profile generated by the INNS, the tracking error of the setpoint is integrated and used as a training signal to adjust the INNS weight parameters. Using the error criteria defined for the INNS, the on-line performance monitoring system requires an adjustment of the INNS which do not meet the criteria. If the error shows an abnormally large value, the INNS needs to be redesigned after being decided whether it was caused by a fault or not.

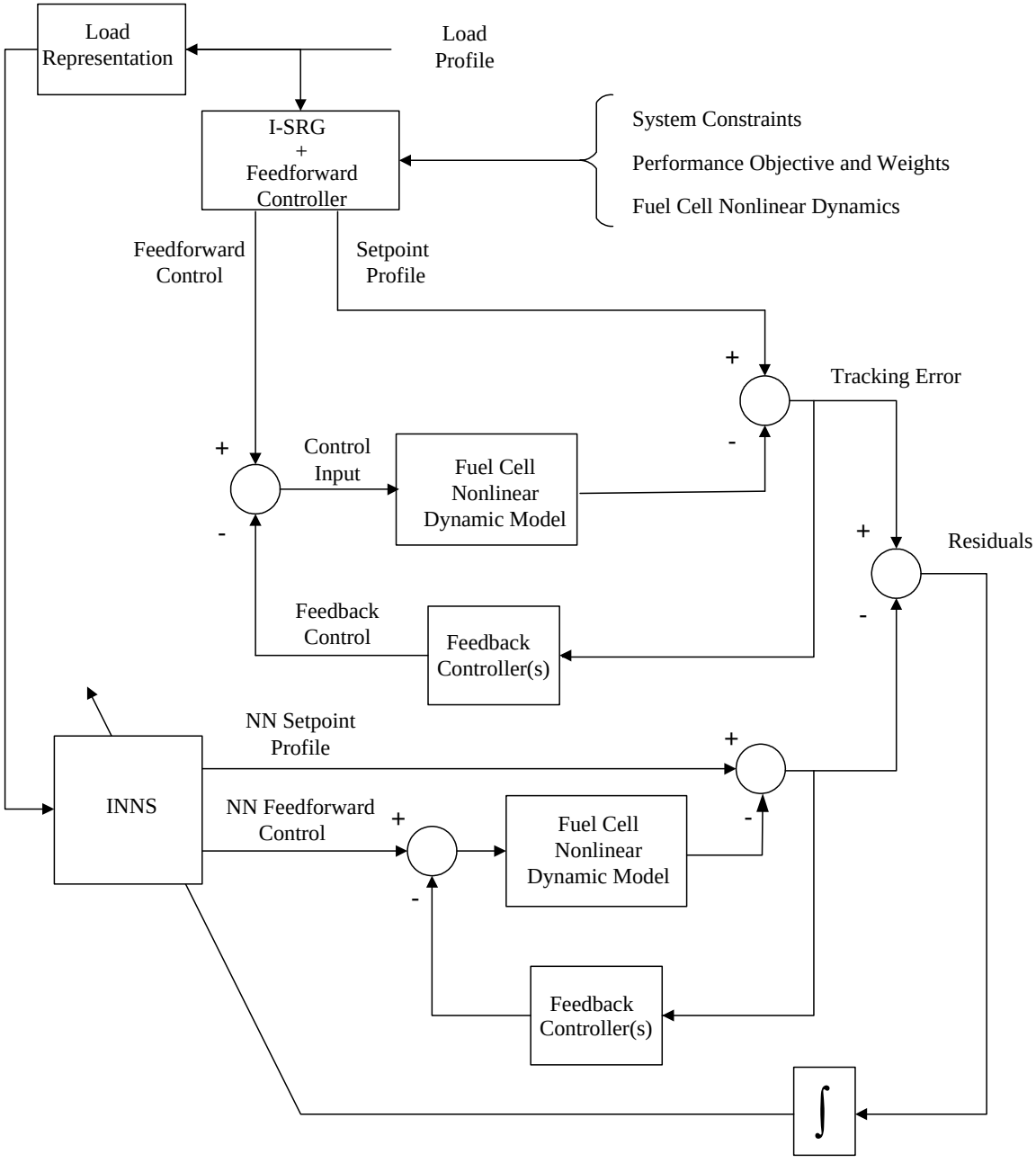

Figure 4.13. Off-line training of the INNS.

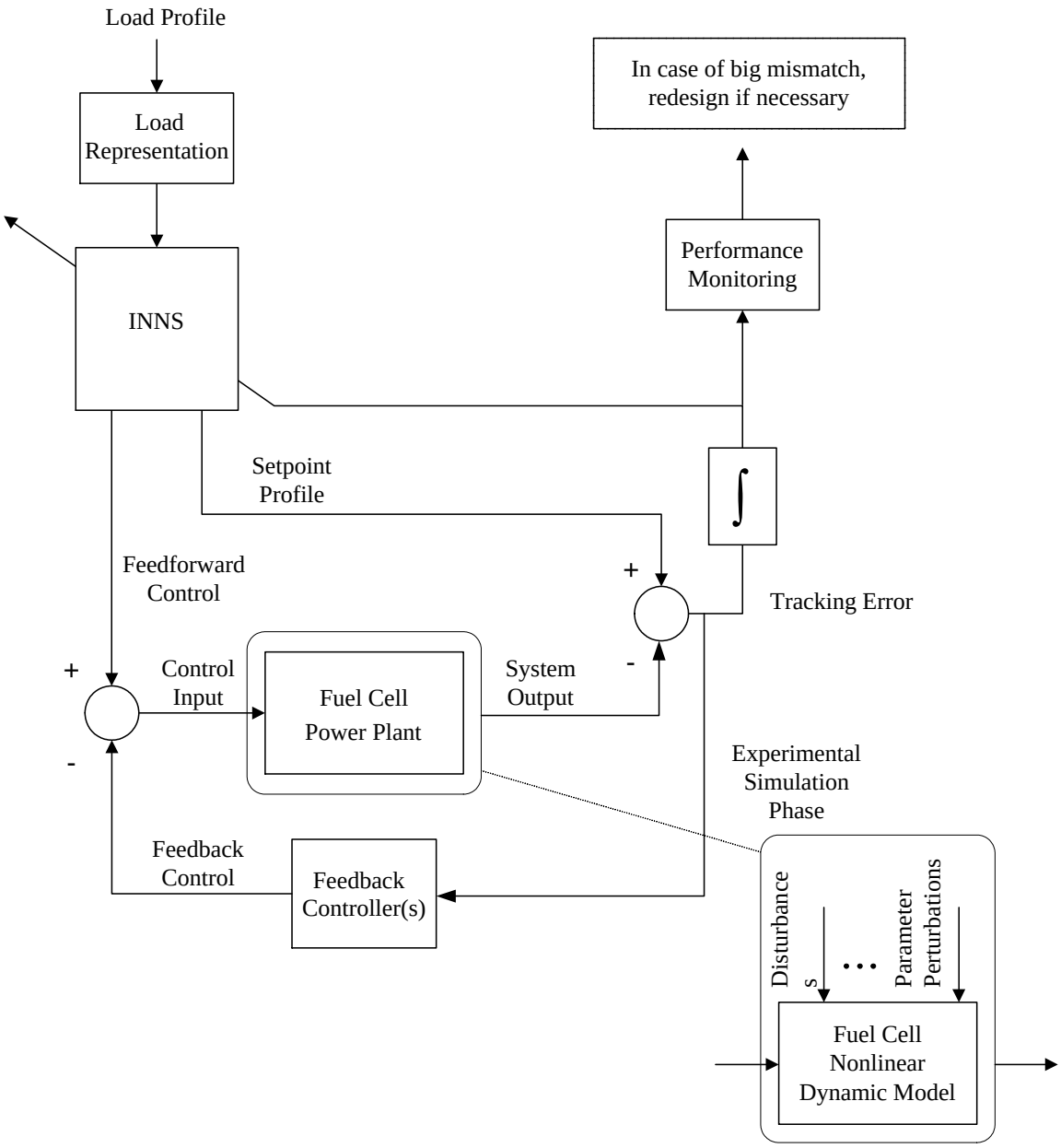

Figure 4.14. On-line training of the INNS.

Chapter 5

NN MODELING OF A MCFC POWER PLANT

Detailed modeling of an MCFC power plant has been of considerable interest in predicting the fuel cell performance and also for use in various systems engineering activities such as control and fault-diagnosis. In the design of control systems for a fuel cell power plant, an identifier is one of the components for power plant control that provides information about the plant to controllers. On the other hand, fault-diagnosis is an important function for power plant monitoring to detect incipient faults for accommodation [65].

It is very difficult to model an MCFC power plant because of non-linearities and computational fluid dynamics. Therefore, computations of existing models are too complicated to be used for on-line control design and fault-diagnosis. The massive parallelism, natural fault tolerance and implicit programming of neural network computing architectures suggest that they may be good candidates for implementing real-time dynamic models for large-scale, nonlinear dynamic systems [64]. This leads to the adoption of the neural network identification method for developing a quantitatively good multi-input and multi-output (MIMO) model for an MCFC power plant. The simulation results on the MIMO model show that neural network identification is feasible for modeling an MCFC power plant.

5.1 Subsystems of an MCFC Power Plant

For the system identification, a NN identifier must be chosen to have a small number of parameters, i.e., fewer weights for neural network model. This is because the more parameters we use, the higher the random influence on the model. A fuel cell power plant can be divided into three major subsystems to handle high computational complexity. The subsystems, as shown in Fig. 5.1, are the Oxidizer Subsystem, Fuel Cell Stack Subsystem, and Heat Recovery Unit Subsystem. Each subsystem is modeled by a seperate neural network. Three subsystems are introduced in the following sections.

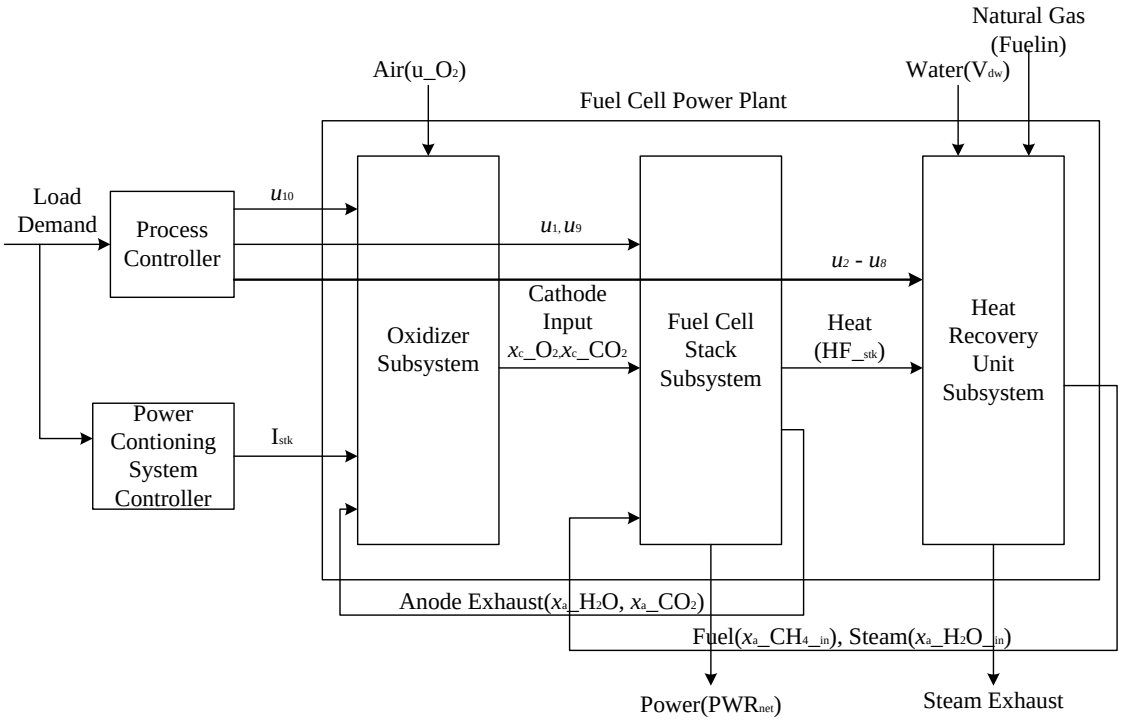

Figure 5.1. Subsystem model of SCDP.

5.1.1 Oxidizer Subsystem

The oxidizer model had been simplified by assuming a single equivalent air inlet flow. We assume that stack temperature is controlled by this single air flow. Control of stack temperature is achieved by adjusting the air flow into the oxidizer. Due to the large (equivalent) stack thermal time constant there is a significant delay in compensating control. Thus, additional feedforward control is introduced to supplement feedback control. This modified subsystem is shown in Figure 5.2. For simplicity, we assume two air flow actuators - one under feedforward control and the other (necessary for robustness) under stack temperature feedback control. The function *f*(x) can be implemented by the I-SRG as a mapping between the steady-state electrical power and steady-state excess air flow; this provides a flow setpoint corresponding to any measurable stack power. This mapping is obtained by running steady-state simulations at different load levels (using feedback-only control), obtaining the steady-state values of excess air flow and curve-fitting the points.

The following equation represents the main input/output of the oxidizer subsystem:

$$(x_{c\_o_2}, x_{c\_CO_2}) = f_{OX}(u\_O_2, x_{a\_H_2O}, x_{a\_CO_2}, I_{stk}, T_{stk}), \tag{5.1}$$

• input (5) : u_O_2 (Air flow rate), $x_{a\_H_2O}$ (Anode off-gas H2O), $x_{a\_CO_2}$ (Anode off-gas CO2), I_{stk} (Stack current), T_{stk} (Stack temperature),

• output (2) : $x_{c\_O_2}$ (Cathode input-gas O2), $x_{c\_CO_2}$ (Cathode input-gas CO2),

where "x" is represented as the mole fraction of the corresponding subscript gas.

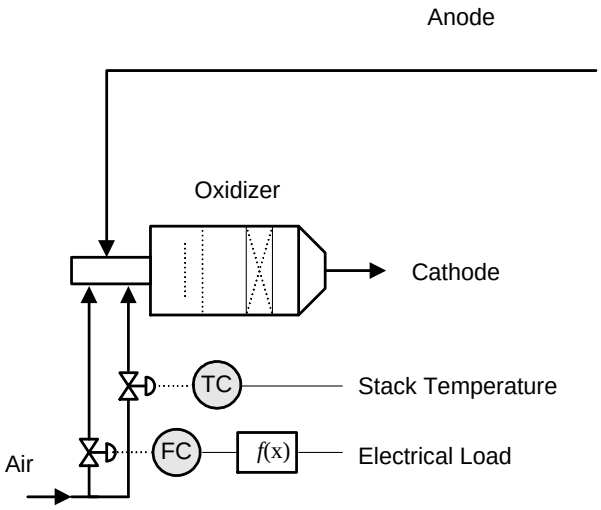

Figure 5.2. Oxidizer Subsystem.

5.1.2 Fuel Cell Stack Subsystem

A schematic of the integrated stack-oxidizer-booster blower is shown in Figure 5.3. This subsystem is evolved with some assumptions. The first is that regulated RU backpressure is replaced by a constant pressure (same regulated value for all plant loads). Secondly, gas composition into the RU is set as a constant, whose value is equal to the gas composition into the RU at nominal conditions. Thirdly, temperature into the RU is assumed to be a static function of system load—in the complete plant model the setpoint of temperature into the RU is a static function of system load. Finally, fuel utilization is regulated by adjusting the gas flow into the RU. Concerning the gas flow leaving the cathode and entering the Heat Recovery Unit (HRU), it is assumed that HRU flow is dependent on constant downstream atmospheric pressure. For now, it is sufficient to say that both temperature and pressure into the system of Figure 5.3 are rapidly controlled in the complete system. Gas composition at the same point is nearly invariant with load in

the complete system. As far as the control of fuel utilization is concerned, the proper gas flow rate is rapidly controlled. Steam-carbon ratio (ratio of moles of H_2O to moles of CH_4) is automatically fixed by virtue of the fixed gas composition.

The following equation represents the main input/output of the Fuel Cell stack subsystem:

$$(x_{a\_H_2o}, x_{a\_CO_2}, TF_{stk}, PWR_{net}) = f_{FC}(x_{c\_O_2}, x_{c\_CO_2}, x_{a\_CH_4\_in}, x_{a\_H_2O\_in}, P_{ru}, DP_{stk}), \quad (5.2)$$

- input (6) : $x_{c\_O_2}$ (Oxidizer output-gas O_2), $x_{c\_CO_2}$ (Oxidizer output-gas CO_2), $x_{a\_CH_4\_in}$ (Fuel CH_4), $x_{a\_H_2O\_in}$ (Steam H_2O), P_{ru} (RU Back pressure), DP_{stk} (Stack differential pressure).
- output (4) : $x_{a\_H_2O}$ (Anode exhaust H_2O), $x_{a\_CO_2}$ (Anode exhaust CO_2), TF_{stk} (Heat), PWR_{net} (Electric Power).

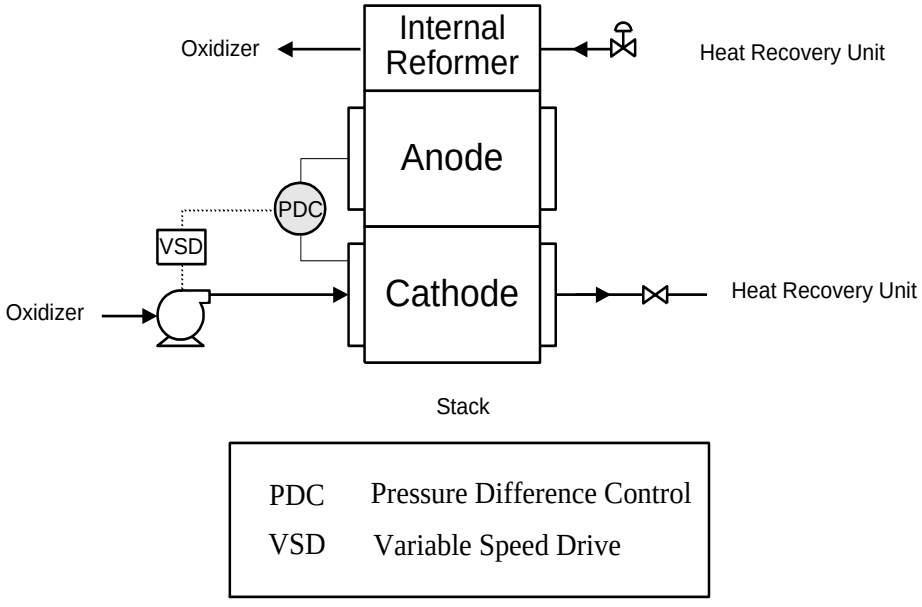

Figure 5.3. Fuel Cell Stack Subsystem.

5.1.3 Heat Recovery Unit Subsystem

Figure 5.4 shows a schematic of the Heat Recovery Unit. Stack cathode exhaust gas is a superheated mixture of CO_2, H_2O, N_2, and O_2 at a temperature of about 1250 °F. The exhaust gas exchanges heat with the tube-side fluid in each of the following: reformer (RF), fuel superheater (FS), steam superheater (SS), boiler (BL), and fuel preheater (FP). Processed city water is converted to saturated steam within the boiler and then converted to superheated steam within the steam superheater. Natural gas is preheated within the fuel preheater and then mixed with the superheated steam where the mixture is again heated in the fuel superheater to the design conditions of the RUs. The remaining heat exchanger is the reformer, used to provide a small slipstream of hydrogen necessary for proper operation of the hydrodesulfurizer. This is accomplished by another steam reforming reaction where the necessary steam is bled from the main steam line and the necessary methane is continuously recycled from the hydrodesulfurizer exhaust. The control objectives of the Heat Recovery Unit subsystem are the natural gas flow and temperature, the Drum level and pressure, the RU inlet temperature, the steam flow, and the exhaust temperature.

The following equation represents the main input/output of the Heat Recovery Unit subsystem:

$$(x_{a\_CH_4\_in}, x_{a\_H_2O\_in}) = f_{HR}(V_d, P_d, w_{ng}, w_{steam}, H_t^{in}, T_{gas}^{in}, T_{ru}^{in}, T_t), \tag{5.3}$$

- input (8) : V_d (Steam drum volume), P_d (Steam drum pressure), w_{ng} (Natural gas flow rate), w_{steam} (Steam flow rate),

H_t^{in} (Specific enthalpy of inlet), T_{gas}^{in} (Temperature of input natural gas),

T_{ru}^{in} (Temperature of RU inlet), T_t (Temperature of superheater exhaust),

• output (2) : $x_{a\_CH_4\_in}$ (Fuel CH_4), $x_{a\_H_2O\_in}$ (Steam H_2O).

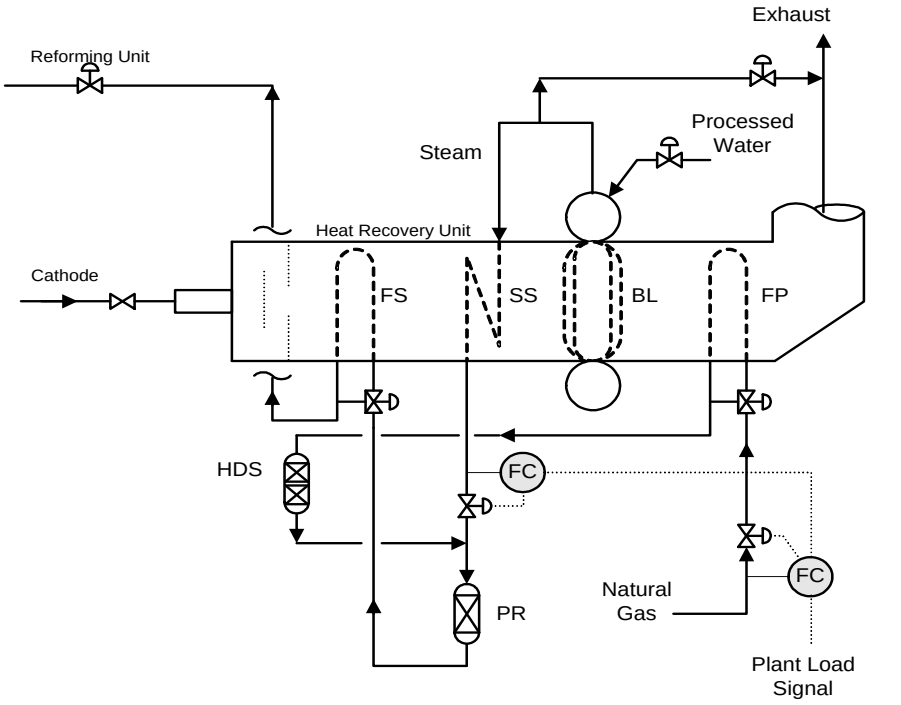

FS	Fuel Superheater	PR	Fuel Preconverter
SS	Steam Superheater	FC	Flow Control
BL	Boiler	TC	Temperature Control
FP	Fuel Preheater	VSD	Variable Speed Drive
HDS	Hydrodesulfurizer		

Figure 5.4. Heat Recovery Unit Subsystem.

5.2 NN Architecture for Modeling of Subsystems

Increasingly complex dynamic systems with significant uncertainty have led to a revolution from conventional control and system identification methods. The importance

of studying neural network-based control architectures is revealed in fundamental difficulties of the current adaptive control techniques.

It is well known that the ability to learn is one of the main advantages that make the neural networks so attractive. In addition to the learning ability, another key advantage of neural networks is their interpolation/extrapolation properties. The NN model can provide output for a load which may not have been included in the training data set. Neural networks can also provide, in principle, significant fault tolerance, since damage to a few links need not significantly impair the overall performance.

Several neural network models and neural learning schemes were applied to system controller design and system identification during the last three decades, and many promising results were reported. Most people used the feedforward neural network (FNN), combined with tapped delays, and the back-propagation training algorithm to solve the dynamic problems; however, the feedforward network is a static mapping and without the aid of tapped delays it does not represent a dynamic system mapping. On the other hand, recurrent neural networks have important capabilities not found in feedforward networks, such as attractor dynamics and the ability to store information for later use. Of particular interest is its own natural temporal operation. Thus the recurrent neural network (RNN) is a dynamic mapping and better suited for dynamic systems than the feedforward network.

The desire for a simple RNN and a shorter training time for the neural network model has led to the development of diagonal recurrent neural networks (DRNN) [68]. It can be shown that the DRNN model is a dynamic mapping in the same way the fully

connected recurrent neural network (FRNN) is dynamic [70]. Since there are no interlinks among neurons in the hidden layer, the DRNN has considerably fewer weights than the FRNN and the network is simplified considerably. Figure 5.5 shows the FNN and DRNN with one hidden layer. The DRNN was used successfully for nuclear reactor temperature control, load forecasting, and synchronous machine control [66]-[70].

In view of the complexity of each subsystem, DRNN is adopted as a possible candidate architecture for the neural network model, which has one hidden layer. In the neural network structure, more hidden neurons are needed as the function being fitted increases in complexity [71]. The number of neurons in the hidden layer is chosen as 2n + 1 by a rule of thumb, where n is the number of input. Each subsytem has NN models as many as the number of its output. The NN model structure for the subsystems are summarized in Table 5.1.

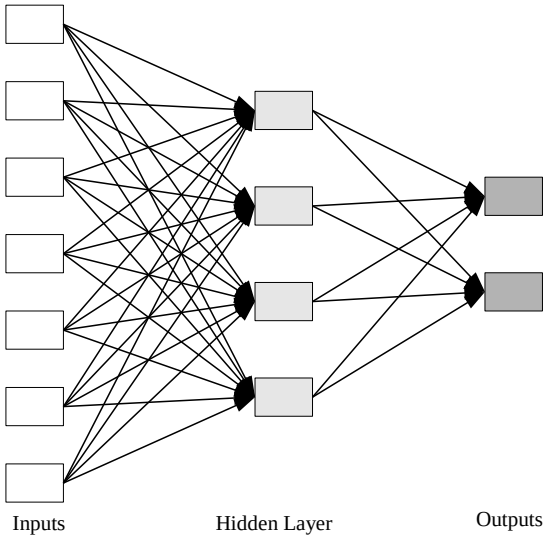

(a) Feedforward NN

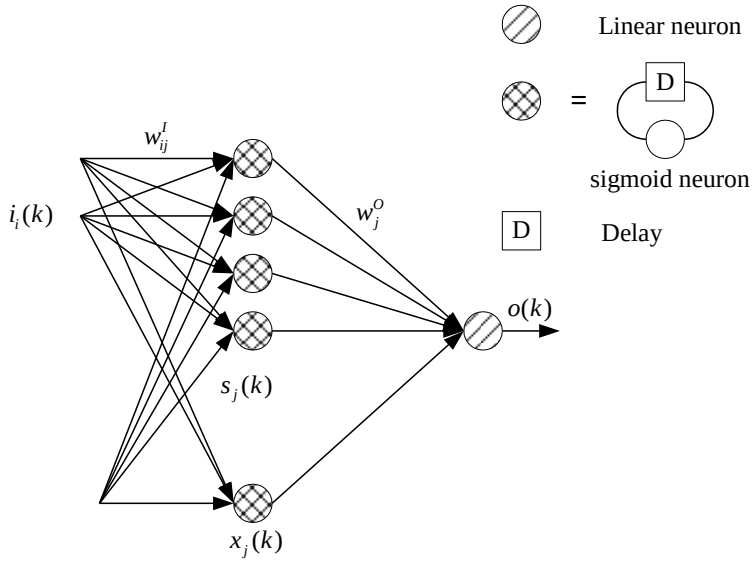

(b) Diagonal Recurrent NN

Figure 5.5. Structures for neural networks (a) FNN (b) DRNN.

Table 5.1. Summary of the NN models for the subsystems.

Subsystem	Number of input	Number of output	Number of hidden layer	Number of hidden neuron
Oxidizer	5	2	1	11
Fuel Cell Stack	6	4	1	13
Heat Recovery	8	2	1	17

5.3 Neural Network-based Subsystem Model

In order to obtain training data for each subsystem NN model, a wide range of operating data for fuel cell power plant needs to be obtained. The data for a wide range of operation can be extracted by changing the power demand setpoint. The power setpoints from the dynamic unit load demand are between 70 % and 100 %, in the increment of 5%. To run the matlab/simulink model of the fuel cell power plant, the ode15s solver is used

and the maximum step size is set to 0.2 to solve stiff differential equations. Thus, the data for the fuel cell power plant was sampled in every 5 sec to train NNs.

After training the NN-based subsystems, the outputs of the NN-based subsystems are post-scaled to obtain actual outputs with minimum and maximum values which were used for pre-scale. The results of training were evaluated based on the following indices for the normalized values:

- Mean Absolute Error:

$$MAE = \frac{1}{n}\sum_{i=1}^{n}\left|y_i - \hat{y}_i\right|, \tag{5.4}$$

- Mean Square Error:

$$MSE = \frac{1}{n}\sum_{i=1}^{n}(y_i - \hat{y}_i)^2, \tag{5.5}$$

where y_i is the output sequence of training data and $\hat{y}_i$ is the output sequence of its corresponding NN model. Table 5.2 shows that the errors between outputs of NN-based subsystems and original data from plant simulator are very small. The outputs of trained NN-based subsystems are plotted in Figures 5.6-5.8, and show satisfactory results for NN modeling.

Table 5.2. Evaluation with trained data.

Subsystem	Oxidizer		Fuel Cell Stack				Heat Recovery Unit	
Output	Cathode input-gas O2	Cathode input-gas CO2	Anode exhaust H2O	Anode exhaust CO2	Heat	Electric Power	Fuel CH4	Steam H2O
MAE	0.2266	0.3223	0.1481	0.1517	0.1477	0.2091	0.4916	0.3011
MSE	0.2735	0.6393	0.1566	0.1178	0.0315	0.2928	0.4095	0.3827

5.3.1 Oxidizer Subsystem

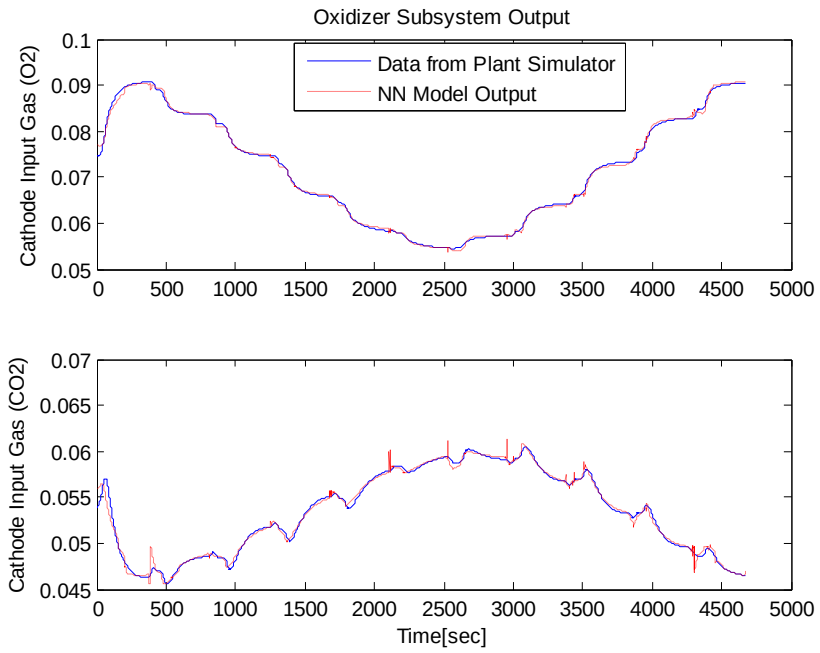

Figure 5.6. Outputs of oxidizer subsystem.

5.3.2 Fuel Cell Stack Subsystem

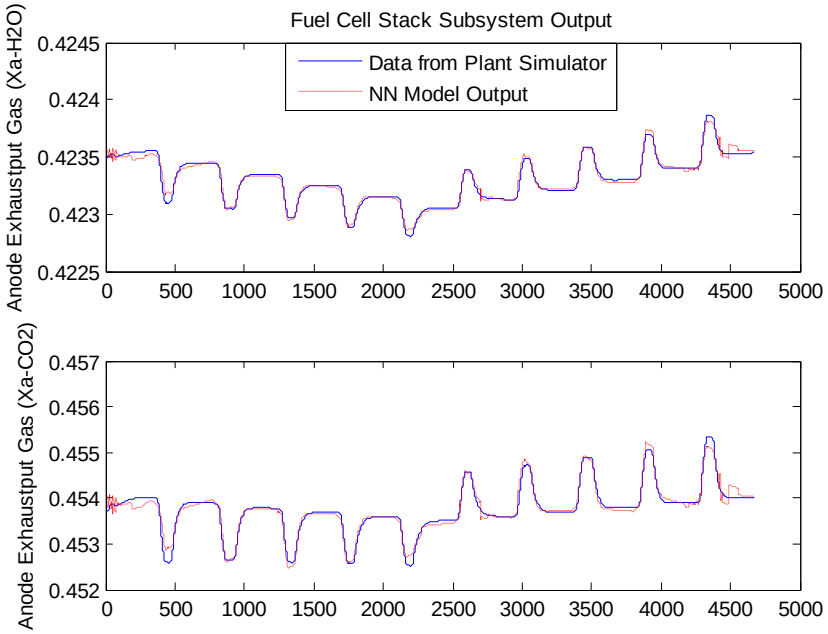

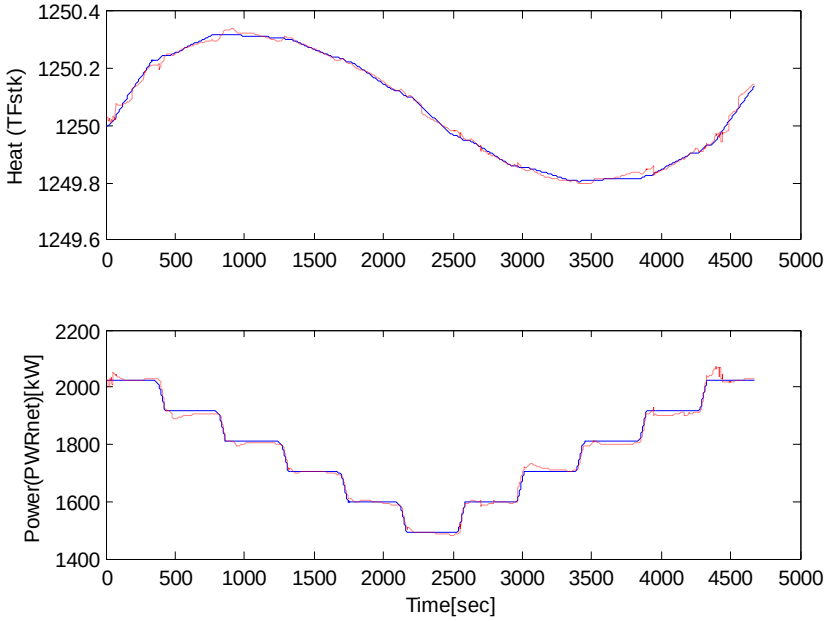

Figure 5.7. Outputs of fuel cell stack subsystem.

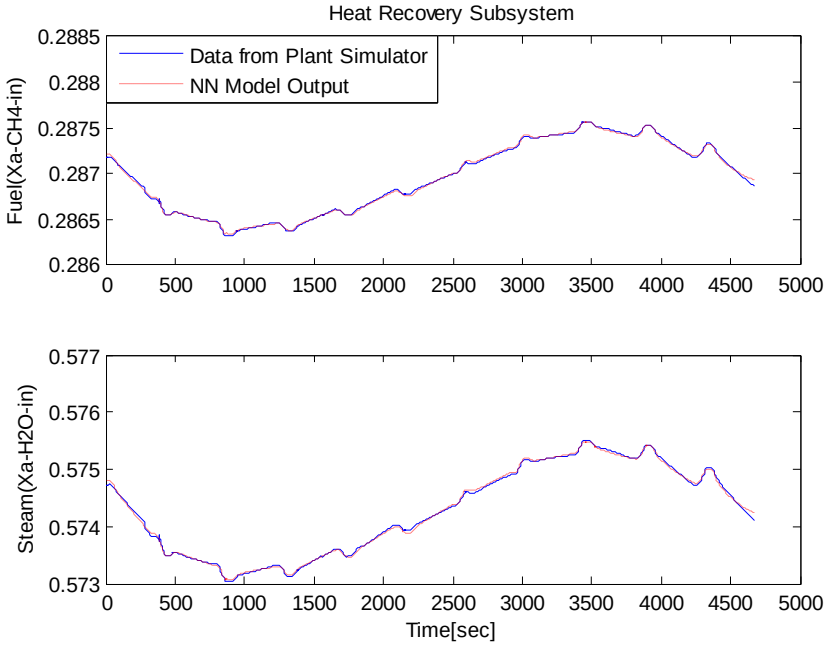

Figure 5.8. Outputs of heat recovery unit subsystem.

5.3.3 Heat Recovery Unit Subsystem

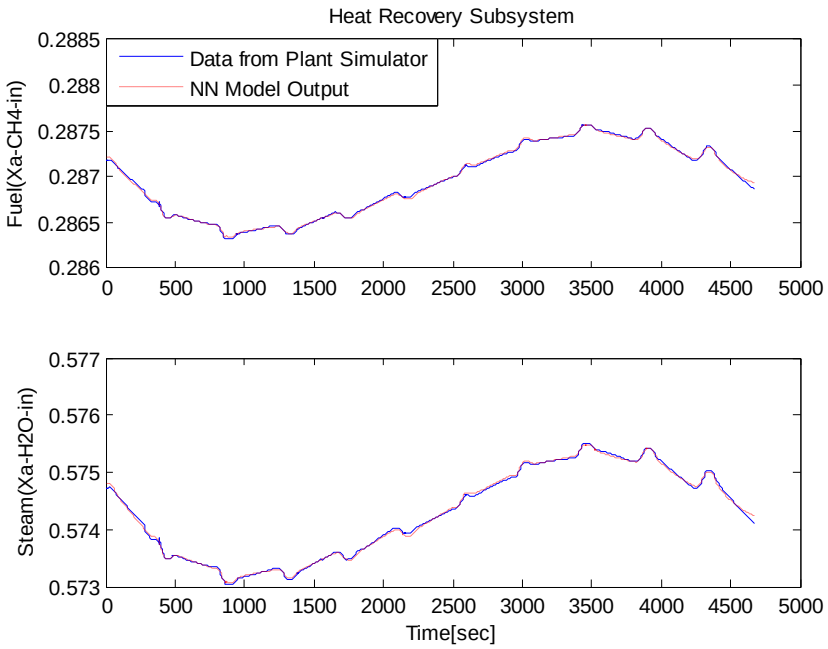

Figure 5.9. Outputs of heat recovery unit subsystem.

5.4 Neural Network based- Combined Fuel Cell Power Plant Model

The NN-based subsystems are combined to complete a NN-based combined model (NNCM) of the fuel cell plant. The NNCM can be constructed by using each subsystem output as an input to an other subsystem. The NNCM has one output of power and three external inputs to fuel cell plant in addition to the control inputs: air, water, and natural gas. The following equation represents the main input/output of the NNCM:

$$PWR_{net} = f_{NNCM}\,(u\_O_2, w_{ng}, w_{steam}), \tag{5.6}$$

• input (3) : u_O_2 (Air flow rate), w_{ng} (Natural gas flow rate), w_{steam} (Steam flow rate),

• output (1) : PWR_{net} (Electric Power).

Using trained data, the output of the NNCM is obtained and plotted in Figure 5.9, which is almost the same as PWR_{net} of Figure 5.7.

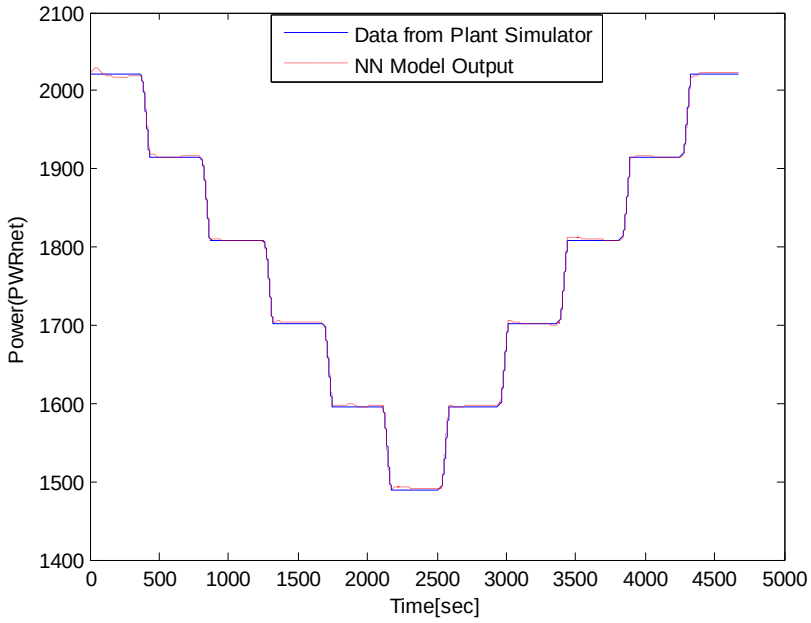

Figure 5.10. Power output of NN combined model.

For the validation of the NNCM, an arbitrary AC power demand (P_d) is applied. For validation purposes the new P_d should allow the plant to reach steady-state for several different power demands. Once steady-state has been reached, the new P_d should maintain that value for at least 30 minutes. This P_d replicates a typical P_d that would be seen in real applications. Fig. 5.10 shows a candidate P_d that was used to validate the NNCM. The new P_d begins at 100% and decreases to 70%, then increases to 80%, and

finally back to 100% of the Maximum Guaranteed Rating (MGR). In the decreasing section of Figure 5.10, the new P_d is changed at a rate of 10 kW/minute.

The output result of the NNCM is the total power output. Observing the error between the simulation data and the NNCM output gives a good idea of the allowable accuracy of the NNCM. These outputs were chosen because they are important in the production of power. The primary goal for following the AC power demand has been achieved, while maintaining the secondary objectives for keeping the pressure and temperatures within the operating windows. With the proposed NNCM, the NN control systems generate the optimal control action very efficiently. Since the PI-based plant simulator has many control loops, the failure of a single loop could adversely effect the operation of the rest of the system. Moreover, under a changing environment, PI control systems have to properly tune gains and time constants continuously. However, NN model generates optimal control action by minimizing load-tracking error without consideration of complicated control loops or adjusting of gains and time constants. The NN model also preserves stability by predicting the outputs of the plant, while PI control uses the actual error from the real plant. Therefore the NN model can be used as an advanced control methodology for real applications.

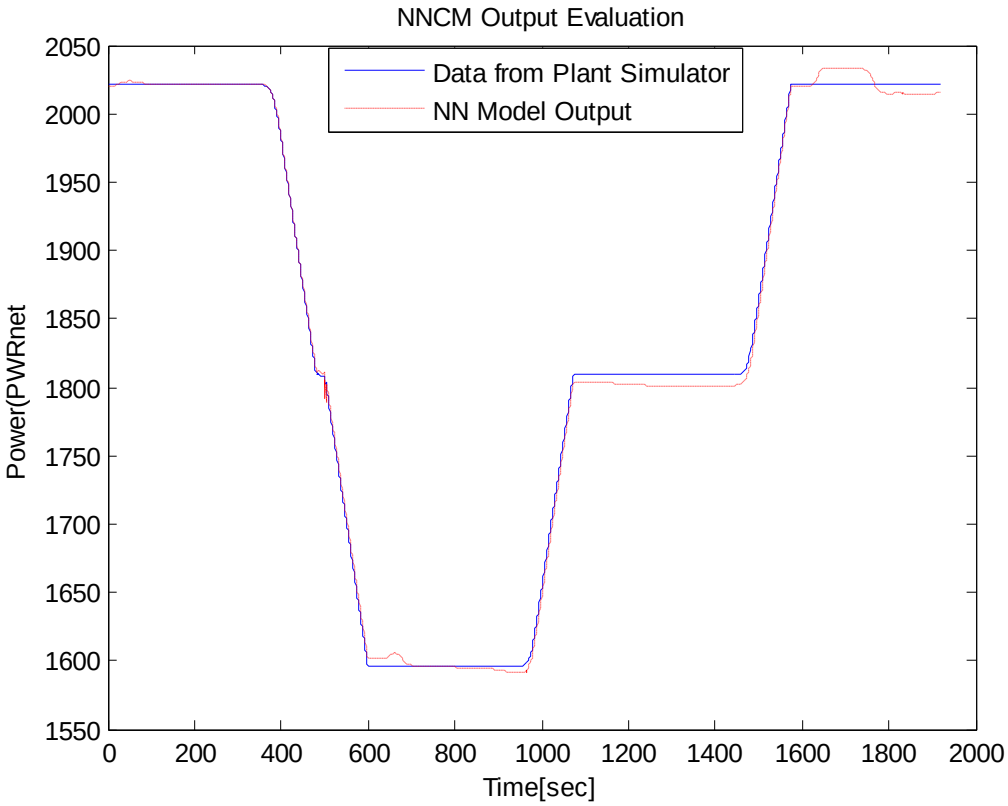

Figure 5.11. Output evaluation of NNCM.

Chapter 6

INTERFACE OF A FUEL CELL DISTRIBUTED GENERATOR TO THE UTILITY SYSTEM

Distributed generation (DG) systems such as microturbines, wind-turbines, photovoltaics and fuel cells can help to improve power quality, power supply flexibility and expandability, and maintain system stability while reducing the transmission and distribution cost. There are many issues on interconnecting the utility grid with DGs. Presently; IEEE developed a uniform standard for the interconnection of distributed resources with electric power systems along with requirements relevant to the performance, operation, testing, safety considerations, and maintenance of the interconnections [2]. Most of the issues can be resolved through design of the Power Conditioning System (PCS) which inverts DC voltage to AC grid voltage for the grid interface.

A fuel-cell DG is more debatable than other DGs. It has more potential to save energy and reduce emissions than a micro-turbine DG, and its generation power is controlled flexibly compared to wind-turbines and photovoltaics. As the fuel cell stack operates at low DC voltage ranges, the PCS must be introduced to boost and invert the DC voltage to an AC grid voltage for grid-connected operation. The grid-interactive PCS also controls power flow and quality [84]-[86].

6.1 Operating Issues on Distributed Generators

Current distribution systems are not designed for two-way power flow. In a radial feeder, the power flows unidirectionally from a single source to the loads. The penetration of DG into the feeder can cause a flow reversal. This flow reversal violates the concept of "radial design" and can have a significant impact on the operation of the feeder. As a result, utilities have begun to investigate the operating conflicts on their systems.

6.1.1 Fault Processing

Most distribution systems are operating in a radial configuration, in which there is one source and the feeders extend radially from the source [87]. In this set up, fault clearing requires then the opening of only one device. With DG, there are multiple sources. Therefore, opening only the utility breaker does not guarantee the fault clearance. Because of the huge infrastructure of existing distribution systems, the DG must adapt to the way the utility works. All DG protection devices must then detect the fault and separate to allow the normal fault-clearing process to proceed.

Due to the fact that many faults are temporary, reclosing is common throughout North America and Asian countries which enable the power to be restored to the customers within seconds. DG must disconnect early in the reclose interval to allow time for the arc to dissipate in order to have a successful reclose [87]-[89]. If the DG is still connected upon reclosing, the DG equipment itself is subject to damage. Instantaneous reclose, to improve power quality, increases the conflict where the reclose interval is

nominally 0.5s but can be as short as 0.2s, which is in the range of relaying and opening times for DG breakers. A reclose interval of at least 1s is safer in the presence of DG and many utilities now use 2 or 5s for the first reclose interval fault to reduce the chances that the DG will fail to separate in time, but this results in reduced power quality.

Utility breakers and reclosers are set to see a certain distance down the radial feeder referred to as the "reach" of the device and determined by the minimum fault current the device will detect. DG can reduce the current seen by the relay due to the opposite current flow, and hence shortening its reach [72]-[87]. High impedance (low current) faults will go undetected until they turn into larger faults with more damage to the utility equipment and more risk of sustained interruption to customers. It was mentioned earlier that DG increases the system reliability; however, in some circumstances, when there is a fault in the distribution system, the presence of DG might have a negative impact on the system reliability.

The fault contribution from a single small DG unit is not large; however, the aggregate contributions of many small units, or a few large units, can alter the short circuit levels enough to cause mis-coordination of fuse-breaker. This could affect the reliability and safety of the distribution system. If DG units are added to the system, the fault current may become large enough that the lateral fuse no longer coordinates with the feeder circuit breaker during a fault. This would lead to unnecessary fuse operations and decreased reliability on the lateral. For inverters, the fault contributions will depend on the maximum current level and duration for which the inverter manufacturer's current

limiter is set to respond. On some inverters, fault contributions may last for less than a cycle, in other cases it can be much longer.

When a single generator is added to the system, a manual calculation of the peak fault currents based on manufacturer's data can be performed to screen for a serious impact on the existing short circuit levels. For multiple generation devices scattered throughout the system or for large generators, the only accurate approach is to perform a software based short circuit analysis which correctly models the short circuit behavior of the generators. In many cases, the DG units will not pose a threat to existing coordination; only a relatively few cases may require changes in protection settings. A ground fault analysis in a real power system model is performed using a software program to examine the impact to the distribution network when the FC DG is added. Detailed simulation results are explained in Figures 6.24 ~ 6.29 of section 6.5, showing no serious problems with the addition of a FC power plant.

6.1.2 Grounding and Transformer Interface

Distributed generation must be applied with a transformer configuration and grounding arrangement compatible with the utility system to which it is to be connected. Otherwise, voltage swells and over-voltages may be imposed on the utility system that damage utility or customer equipment.

Use of a DG source that does not appear as an effectively grounded source connected to such systems may lead to over-voltages during line to ground faults on the utility system. This condition is especially dangerous if a generation island develops and continues to serve a group of customers on a faulted distribution system. Customers on

the unfaulted phases could in the worst case see their voltage increase to 173% of the prefault voltage level for an indefinite period. At this high level, utility and customer equipment would almost certainly be damaged. Saturation of distribution transformers will help slightly to limit this voltage rise. Nonetheless, the voltage can still become high (150% or higher). For example, marginally rated lightning arresters would probably fail in less than 5 seconds if the voltage reached just 150% of the prefault condition [88].

To avoid problems, all DG source on multi-grounded neutral systems that are large enough to sustain an island should present themselves to the utility as an effectively grounded source. If they do not, they should use appropriate protective relaying to detect primary side ground fault over-voltages and quickly trip off-line (instantaneous trip). The former approach is preferred since it limits by design the voltage swells that the system will see during a fault. The latter approach, while used successfully in many installations, could subject the customer to many cycles of severe over-voltage prior to the DG unit being cleared from the system. If the DG is not cleared quickly enough, equipment could be damaged.

Transformer configurations with Wye-grounded (High Side)/Delta(Low Side) typically provide effective grounding regardless of generator grounding arrangement. Use of an adjacent grounding transformer bank is an approach for creating a DG source that behaves as an effectively grounded source when the step-up transformer does not provide effective grounding. It should be noted that any additional grounding source on the system, whether it is by a grounding bank or by using an appropriate step-up transformer

winding arrangement, will have the effect of reducing (diverting) the zero sequence return current seen at the substation that arises from line to ground faults on the fault.

The amount of current diverted is determined by the ratio of the DG grounding source impedance to the substation grounding impedance. This effect has the impact of desensitizing the ground fault relaying at the substation since the substation will see less current for a given magnitude line to ground fault out on the feeder. To assess the impact of this problem, the grounding source impedance of the DG site must be analyzed to insure that it won't divert more than a small fraction of the fault current (perhaps 10% as a rule of thumb). For small DG units it usually is not an issue.

For a larger unit acting as a ground source or for cases involving many small units acting together as ground sources, the short circuit studies need to identify the impact of this and see if any changes are required in relay pickup setting. A grounding resistance can be used on the DG ground source neutral connection to limit the impact. This also helps to reduce circulating current in any delta winding of the transformers that are caused by zero sequence voltages on the feeder.

Proper review of the generator characteristics and utility system design prior to installation of the DG unit can insure that grounding compatibility problems are dealt with appropriately. Grounding compatibility is crucial to insure that power quality and reliability are not degraded by the addition of DG units. In a real distribution simulation of Figure 6.20, the transformer between the distribution line and the FC power plant is configured with Y(High)/Δ(Low) to provide effective grounding. Simulation results of

Figures 6.24 ~ 6.29 prove that the FC power plant with the Y/Δ transformer configuration is not affected by the line to ground fault.

6.1.3 Ferroresonance

Many modern loads are served with underground cable as shown in Figure 6.1, which is commonly run from an overhead line, where it is nearly universal to apply fuses at the riser pole to protect the overhead line from faults on the cable. The fuses are sized to blow quickly because it is assumed that all cable faults are permanent and there is no reason to attempt fuse saving.

Requiring the DG to disconnect at the first sign of trouble will leave the service transformer isolated without load and served with an open phase. This is a classical ferroresonance condition where the capacitance of the cable appears in series with the magnetizing inductance of the transformer [89]. This results in very irregular high voltages which have to be interrupted by the distribution breaker.

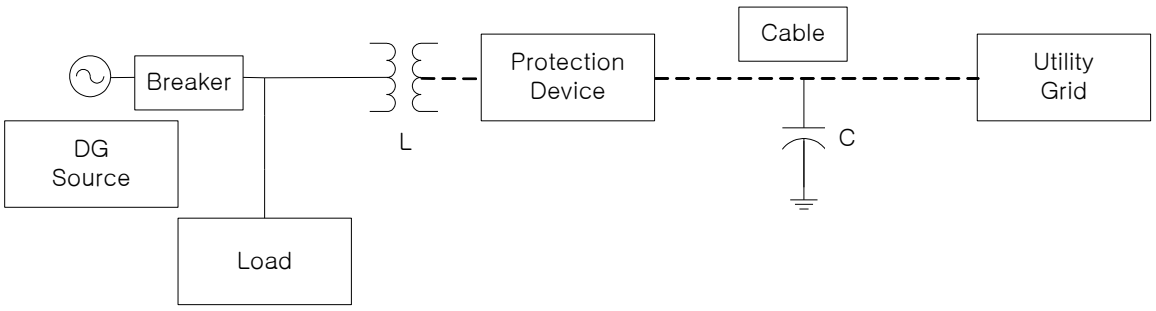

Figure 6.1. Ferroresonance condition in a distribution network.

6.1.4 Islanding

DG relaying might fail to detect that the utility breaker has opened and continue to energize a portion of the feeder forming what is called an "island". "Islanding" is defined in the IEEE standards [90] as a condition in which a portion of the utility system that contains both load and distributed resources remains energized while isolated from the remainder of the utility system. The following problems might take place:

· Low power quality for customers on the island.

· Reclosing.

· Safety concerns of a generator accidentally energizing the line resulting in injuries to the public and the utility personnel.

More attention has been paid to factors that forces islands to become unstable so that they can be detected, such as a deviation in voltage and frequency.

To prevent islanding, a DG unit operating in parallel with the utility system senses a significant voltage sag or discontinuity of service on the utility side and disconnect from the system in a timely manner. Many utilities have standards which require that this time be about 10 cycles or less for serious feeder disturbances (deep voltage sags or interruptions). Voltage and frequency relays are used as a means of anti-island protection. In most cases, if a generator becomes islanded, it will not be able to satisfy the sudden change in its load without a significant change in voltage and/or frequency, and relays will trip the unit off line. This type of anti-islanding protection is called "passive." Passive protection can be fooled if the generator is able to carry the load of the island without a substantial change in voltage or frequency. Therefore, as a further safeguard,

many smaller inverters today also use what is called “active” anti-islanding protection. One common “active” approach is for the inverter to be “tuned” to operate while islanded at a frequency other than 60 Hz.

While the utility signal is present, the inverter is “forced” to operate at 60 Hz. During an interruption, it will drift to its natural “tuned” frequency, once the “forcing utility voltage function” disappears (that is when it becomes islanded). In the process of drifting to the natural inverter frequency, the unit will trip its internal frequency relays, which are set to trip for a deviation from power frequency outside the range of 59.3 to 60.5 Hz. Active anti-islanding is more active than passive, but even it cannot guarantee that an island will not develop in some rare cases. Since islanding can cause severe voltage quality and reliability problems, the proper use and setting of anti-islanding controls is one of the more important issues for DG installations.

The implementation of DG can increase reliability of electric service if units are configured to provide “backup-islands” during upstream utility source outages. To be effective this requires reliable DG units and careful coordination of utility sectionalizing and protection equipment. Any time such a scheme is implemented it needs to be well planned to avoid causing problems. Figure 6.2 shows one scheme where an upstream automatic switch is used to island a section of a distribution feeder. For this approach to work the switch must open during upstream faults and the generators must be able to carry the load on the islanded section maintaining suitable voltage and frequency levels at all islanded loads. Unless a static switch is employed, this scheme would usually result in

a momentary interruption to the island since the DG would trip during the voltage disturbance caused by the upstream fault.

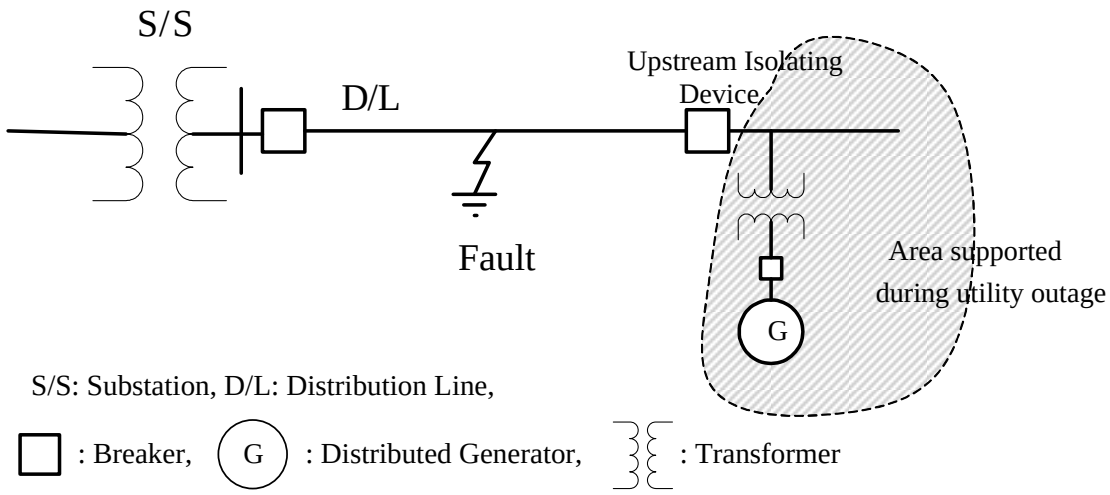

Figure 6.2. Intentional islanding of a portion of a distribution feeder with a DG.

A DG assigned to carry the island must be able to restart and pickup the island load after the switch has opened. Power flow analysis of island scenarios must be performed to insure that proper voltage regulation is maintained and to establish that the DG can handle inrush during "starting" of the island. The DG unit must be able to follow the load during islanded operation and the switch will need to sense if a fault current has occurred within the island zone. When utility power is restored on the utility side, the switch must not close unless the utility and "island" are tightly in synchronism. This requires measuring the voltage on both sides of the switch and transmitting that information to the DG unit supporting the island so that it can "synchronize" with the utility and allow reconnection. Overall, this is complicated, but new automated switch

technologies and communications approaches make this scheme much more practical than in past years [91].

6.2 Power Quality Control on Distributed Generators

In general, back-up generation and on-site power supply provided by DG improve the system power quality. However, some issues might arise when distributed generators, with different types and technologies, are interconnected to the utility distribution system [7]. As the penetration level of DG into the distribution systems increase, the impacts are becoming more apparent and can no longer be neglected.

Harmonics are introduced into the grid, causing distortion that exceeds the total harmonic distortion (THD); reverse power flows caused by the unused power generated by DG are creating more complications for protection engineers; flickers occur because of the switching operations of the DG or the change of the output during normal operation. Due to its design, DG has no intentional attempt to regulate the voltage on the power system. However, it is well known that injecting power into any power system will cause the voltage to change because current is flowing into the system impedance. These impacts are studied, and the methods of controlling and/or eliminating them have been presented.

6.2.1 Loading Concerns

Most of the distributed generators were installed in the network for backup generation, in case of power interruption, or to cover for contingencies when part of the

delivery system is out of service. This will significantly improve the system reliability. However, not all DG technologies might be capable of supplying the load when the utility system cannot. A renewable DG, for example, with an uncontrolled-inverter and lack of storage capacity might not be capable of operating in stand-alone mode.

When the DG is interconnected in parallel with the utility distribution system, some operating conflicts might arise that affect the system reliability. An example is the incompatibility between instantaneous reclosing and DG, or the interference with utility relaying and reducing the devices' reach.

IEEE 1547 serves as a guideline where electric utilities may or may not choose to follow. Many major utilities in California (i.e. PG&E, SDG&E, SMUD, etc.) have chosen to follow it. California Public Utilities Commission (CPUC) Rule 21 technical committee has also adopted this standard. One of the requirements for DG interconnection under Rule 21 is the 15% line section peak load.

This rule is meant to prevent any potential problems that can occur as the level of DG penetration increases. The reason behind this thinking is that a typical line section can be safe to assume to have a minimum load at least 30% of the peak load. At 15% aggregate, the generating capacity would not be more than 50% of the minimum load of the line section, and thus the generation would not have the potential of islanding or to cause any operational problems [92]. In the simulation of Figure 6.20, the maximum capacity of a FC power plant is assumed to be the 3,000 kW considering the regulation of distribution network: 30 % of a maximum distribution line capacity. The load sharing between the FC and distribution line is shown in Figures 6.21 ~ 6.23.

6.2.2 Voltage Regulation

Synchronous generators are capable of providing real and reactive power and, hence, can be used to regulate the voltage in the distribution system to which they are interconnected. Generator controls are much faster and smoother than conventional tap-changing transformers and switched capacitor banks. A conflict might, however, arise due to the interference of these generators with the existing utility voltage regulation equipment. Special communications and control are then required to overcome this conflict and allow these generators to work properly with the utility voltage regulating equipments.

Radial distribution systems are normally regulated using load-tap-changing transformers at substations, supplementary line regulators on feeders, and switched capacitors on feeders. If a DG unit is applied just downstream of a voltage regulator or LTC transformer that is using considerable line drop compensation, then the regulation controls will be unable to properly measure feeder demand.

Note that with distributed generation, the voltage becomes lower on the feeder because the DG reduces the observed load at the line drop compensator control. This confuses the regulator into setting a voltage lower than is required to maintain adequate service levels at the tail end of the feeder. This is the opposite effect of “voltage support”, a commonly touted benefit of DG.

DG may also result in high voltage at some electric customers. For example, a small residential DG system that shares a common distribution transformer with several other residences may raise the voltage on the secondary enough to cause high voltage at

these customers. This can occur if the distribution transformer serving these customers is located at a point on the feeder where the primary voltage is near or above the ANSI upper limit.

Normally, without DG, there would be voltage drop across the distribution transformer and secondary conductors and voltage at the customer service entrances would be less than the primary. The presence of the DG may introduce reverse power flow to counteract this normal voltage drop, perhaps even raising voltage somewhat, and the service voltage may actually be higher at the customer service than on the primary side of the distribution transformer; it may even exceed the ANSI upper limit.

To determine if the DG will cause a significant impact on the feeder voltage, the size and location of the DG, the voltage regulator settings, and impedance characteristics of the line must be considered.

Distribution generation will also impact losses on the feeder. DG units can be placed at optimal locations where they provide the best reduction in feeder losses. Siting of DG units to minimize losses is like siting capacitor banks for loss reduction. The only difference is that the DG units will impact both the real and reactive power flow. Most generators will be operated between 0.85 lagging and 1.0 power factor, but some inverter technologies can provide reactive compensation.

On feeders where losses are high, a small amount of strategically placed DG with an output of just 10-20% of the feeder demand can have a significant loss reduction benefit for the system. Unfortunately, most utilities don’t have control over the siting locations, since DG is usually customer owned.

Larger DG units must be sited with consideration of feeder capacity limits. In some cases, overhead lines and cables may be thermally limited meaning that the DG can inject power that exceeds the line's thermal limit without causing a voltage problem on the feeder. In general, a DG at a location that is thermally limited is not connected at the optimal point from a power loss perspective.

To regulate voltage with DG interconnected to the grid, one of the cheapest and easiest methods is to move the DG generator closer to the load instead of regulator. If a line-drop compensator is used, we should reduce or completely eliminate the line-drop compensator settings and raise the voltage set-point slightly. In the case of diverse loads, use a multiple line-drop compensator (MLDC) [79].

The ability of a DG to counteract voltage sags depends on its type and location. Large synchronous generators can help support the voltage and reduce voltage sags on local facilities. However, impedance of interconnection transformers might prevent any impact on adjacent loads on the feeder. Inverter-based distributed generators can be controlled to supply reactive power for voltage support during the voltage sag. In the real distribution network simulation of Figure 6.20, the FC power plant is installed at the section B_03: load center of five distribution line sections B_01~B_05 to minimize the voltage drop effectively. Table 6.4 and 6.5 show that the FC power plant successfully compensates the voltage drop and maintains adequate service levels within 2% regulation.

6.2.3 Voltage Flicker

Flickers, also known as fast voltage changes, are rapid variations of the rms value between two consecutive levels [94]. This phenomenon is caused by the switching operation of the DG or by the changes of power output during normal operation. DG may cause voltage flicker as a result of starting a machine (induction generator) or step change in the DG output, which results in a significant voltage change on the feeder. In case of wind and solar energy systems, the output fluctuates as the wind and sun intensity change and in case of a fuel cell, abrupt change of load can cause a voltage flicker.

The addition of DG into the feeder can cause a flow reversal, if the loading exactly balances or is less than the generation of DG. When this happens, a "zero point" or "null point" will exist on the feeder. If the "zero point" exists, the reversal of power flow will cause a voltage rise between the "zero point" and the DG unit. This voltage rise can cause the generator to trip offline abruptly. Once the generator is off, voltage will drop where it rose before. Since voltage regulators cannot respond instantaneously, voltage flickers will occur.

To avoid disturbing or damaging other nearby equipment, utilities and IEEE 519 set a limit for these voltage flickers. In the case of switching operations, the voltage level of the consumer's connections, the size of the DG and the frequency of the operations determine the imposed limits. One approach is to determine the magnitude and number of changes of voltage occurring per unit time and see if these are above the visibility or irritation threshold levels of the GE (General Electric) flicker curve in IEEE standard 141. If above the threshold, or if customer complaints occur, mitigation must be considered.

Mitigation approaches include reduced voltage starts on induction generators as well as speed matching. Synchronous generators might require tighter synchronization and voltage matching. Inverters might be controlled to limit inrush currents and changes in output levels. A less technical approach to reduce flicker involves placing constraints on when and how often DG operators may start and change the output of DG systems. Below are some ways that can resolve flicker problems:

- Reconfigure the feeder (synchronous or induction)
- Install a static variable control
- Update the feeder voltage
- Construct a new feeder
- Construct a new substation
- Reduce the starting current of large motors using voltage stator or solid-state motor stator
- Run the DG unit leading (absorbing VAr's)
- Use capacitors and set them in series with the inductance of the distribution feeder (distribution series capacitor [95]).

These methods are sound engineering solutions, but some of them are not economically feasible. Therefore, they may not be employed. In the simulations with FC switching and line to ground fault, any significant impact on system is not detected in Figures 6.21 ~ 6.29.

6.2.4 Harmonics

Distributed generators may introduce harmonics. The type and severity will depend on the power converter technology and interconnection configuration. In the case of inverters, there has been particular concern over the possible harmonic current contributions they may make to the utility system. Fortunately, these concerns are in part due to older SCR type power inverters that are line commutated and produce high levels of harmonic current. Most new inverter designs are based on IGBTs that use pulse width modulation to generate the injected "sine" wave. These newer inverters are capable of generating a very clean output and they should normally satisfy the IEEE 519-1992 requirements [92]-[93].

Harmonics, unlike some transient events such as lightning and or voltage sags that can last from a few to several cycles, are steady-state periodic phenomena that produce continuous distortion of voltage and current that can significantly affect the true power factor of the system. True power factor is defined as the average power divided by the product of rms voltage and rms current, and since harmonic quantities increase rms values of voltage and current, they have a significant impact on the true power factor. Table 6.1 shows the theoretical maximum true power factor of a distorting load as a function of current THD.

Table 6.1. Maximum true power factor of a nonlinear load.

Current THD (%)	20	50	100
Maximum True PF	0.98	0.89	0.71

In the case of a balanced three-phase power system, harmonics fall into the phase sequence pattern shown in Table 6.2. This means the conventional way of viewing "balanced power systems can have no negative- or zero-sequence components" is no longer valid when harmonics are present. Thus, it is important to note that harmonic multiples of three are zero-sequence. This fact accounts for neutral conductor overheating.

Table 6.2. Harmonics phase sequence (Three-Phase Power System).

Harmonic	1st	2nd	3rd	4th	5th	6th	…
Phase Sequence	+	-	0	+	-	0	…

Harmonic effects are categorized into two terms: short- and long-term. Short-term effects are easily noticeable and are the cause of excessive voltage distortion. On the other hand, long-term effects can go undetected and are the cause of increased resistive losses or voltage stresses. Short-term effects also cause the tripping of sensitive loads because some computer-controlled loads are sensitive to voltage distortion. Voltage distortions below 5% are not usually a problem. Voltage distortions above 10% can definitely cause tripping and/or transformer overheating. Overheating usually occurs when a dedicated transformer serves only a large, nonlinear load.

Another impact caused by harmonics is degradation of meter accuracy. The long unanswered question in metering is how active power should be defined and measured when distortion is present.

Harmonics also contribute to blown capacitor fuses and failed capacitors. Harmonic voltages produce excessive harmonic currents in capacitors because of the inverse relationship between capacitor impedance and frequency. Voltage distortions of 10% can easily increase rms currents by 50%. A 10% harmonic voltage for any odd harmonic above the third increase the peak voltage by approximately 10% because the peak of the harmonic usually coincides with the peak of the fundamental voltage.

The harmonic impacts can be detrimental to the distributed circuit. Utility engineers must plan ahead and be able to predict the maximum DG units that can be connected to an existing feeder before harmonic problems are encountered. Other methods of controlling harmonics are:

- To control the harmonic current injection from nonlinear loads and inverter-base generation, transformer connection in a three-phase system should be connected parallel, delta-delta and wye-delta transformers to yield net 12-pulse operation, or delta connected transformers to block triplen harmonics.

- To avoid adverse interaction between harmonic currents and system frequency response, some filtering equipment may be added. Many utilities do this by feeder sectionalizing, adding or removing capacitor banks, changing the size of the capacitor banks, or adding shunt passive filters made of reactors that have low impedance at a tuned frequency for shunting the harmful harmonics off the power system [96]-[97].

- To limit harmonic currents at the load or on the system with shunt filters, a number of devices are used. Here, the nature of the problems will determine which devices are to be used. Solutions can be as simple as an in-line reactor (i.e., a choke) as in

pulse width modulation (PWM) based adjustable speed drive applications, or as complex as an active filter.

6.3 Power Conditioning System for a Fuel Cell Power Plant

A power conditioning system (PCS) is introduced to control energy flow of the DC sources, which is corresponding to an arbitrary power source such as wind-turbine, micro-turbine, photovoltaic cell and fuel cell. The grid-interactive PCS also controls power flow and quality.

6.3.1 Interface Technologies to the Utility System

Distribution generators are interconnected with the utility to operate in parallel with its distribution system. There are three types of electrical system interfaces such as synchronous machines, asynchronous (induction) machines, and power electronic inverters [7].

The majority of DGs interconnected for parallel operation with the utility distribution system are three-phase synchronous machines. Synchronous generators use a DC magnetic field for excitation, and hence they can produce controllable real and reactive power. Emergency back-up generators using fossil-fuel combustion engines are normally synchronous machines. The machine can follow any load within its design capability with suitable field control. Besides, the inherent inertia allows it to tolerate any step changes in the load.

Being capable of producing reactive power, large synchronous generators, relative to the utility system capacity, might act as voltage regulators to improve the voltage profile across the distribution feeder to which they are connected. This is considered as a power quality advantage in weak systems. However, these generators should be coordinated with the utility voltage regulators and protection equipment to avoid any operating conflicts.

Asynchronous generators are induction motors driven slightly faster than the synchronous speed. They are often started as a motor using the utility power line. For weak systems, the prime mover is started and brought to near synchronous speed before the machine is interconnected. Induction generators are typically smaller than 500kW and they are suitable for wind DG. They are easily interfaced to the utility as no special synchronizing equipment is required. Unlike synchronous generators, induction generators are capable only of producing real power and not reactive power. They require reactive power from the power system to which it is connected to provide excitation. This might affect the utility voltage and result in a low-voltage problem. Capacitors are therefore installed on the generator side to supply the required reactive power to avoid any problems.

An inverter is a solid state device that converts DC electricity to AC electricity at a desired voltage and frequency. DG technologies that generate either dc (wind, fuel cell and photovoltaic) or non-system frequency ac (micro-turbines) must use an inverter to interface with the utility grid. However, doubly fed asynchronous machines require no utility interface. The system frequency is a frequency in the range used for supplying

power (commonly 50 or 60 Hz). The inverter technology has changed from the early thyristor-based, line commutated inverters to switched pulse width modulation (PWM) inverters using insulated gate bipolar transistor (IGBT) switches. This shift in technology has greatly reduced the amount of harmonic interference injected by these inverters to the utility system.

Power electronic inverters produce power at unity power factor to allow the full current-carrying capability of the switch to be used for delivering real power. When trouble is detected, the inverter can be switched off very quickly (in milliseconds), unlike the rotating machines, which may require several cycles to respond.

The configuration of a basic inverter interfaced generation system is shown in Figure 6.3. The key components of the system are: energy source, dc link capacitor, voltage source inverter (VSI), and coupling inductance [98].

- If the energy source is a fuel cell, then the voltage across the capacitor is more or less constant, and in modeling and simulation it is often modeled as a constant voltage source.

- The function of the dc link capacitor is to make an energy balance when the energy demand is not exactly the same as the one which is supplied by the energy source. When the real power which is supplied by the inverter or absorbed by the load exceeds the instantaneous supply of the energy source, the dc link capacitor will discharge and cover the remaining power. Similarly, if the load is lower than that of the real power which is supplied by the energy source, the surplus energy will charge the capacitor. This process can be summarized in a short term called “load tracking.”

• In some cases, battery storage is used instead of capacitors. However it should be pointed out that the battery storage is more appropriate for long term use whereas the capacitor is suitable for transient stability.

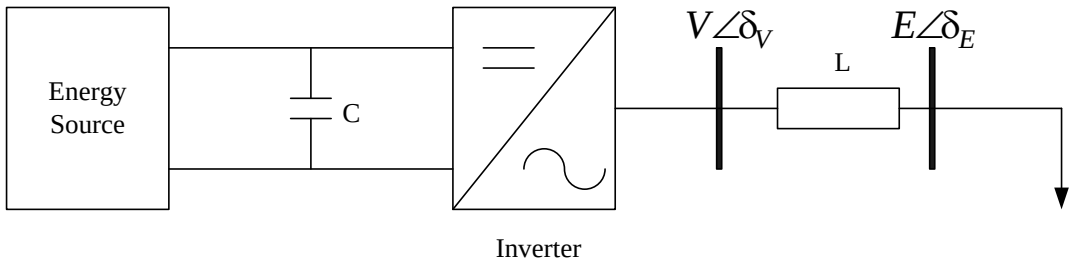

Figure 6.3. Basic inverter interfaced generation system.

6.3.2 PCS Interface between Fuel Cell Stack and the Utility Grid

As the fuel cell stack operates at low DC voltage ranges, the PCS must be introduced to boost and invert the DC voltage to an AC grid voltage for grid-connected operation, and the transformer interface is also possible. The energy flowing from the DC sources to the grid must be controlled in order to track the maximum power point and to maintain a sinusoidal grid current with low harmonic distortion and a high power factor. Currently, the design of PCSs is based on IGBTs that use PWM technology, and on a DSP processor that enables various control algorithms to be used. Hence, they are capable of generating clean output that satisfies the IEEE Standards for harmonics.

Figure 6.4 shows a block diagram of the FC power plant interfaced with the utility grid via PCS, which is composed of boost DC/DC converters, a PWM converter, and a

line filter. The boost converter is a device that accepts a DC input voltage and produces a DC output voltage. Typically the output produced is at a different voltage level than the input. In addition, the boost converters are used to provide noise isolation and power bus regulation.

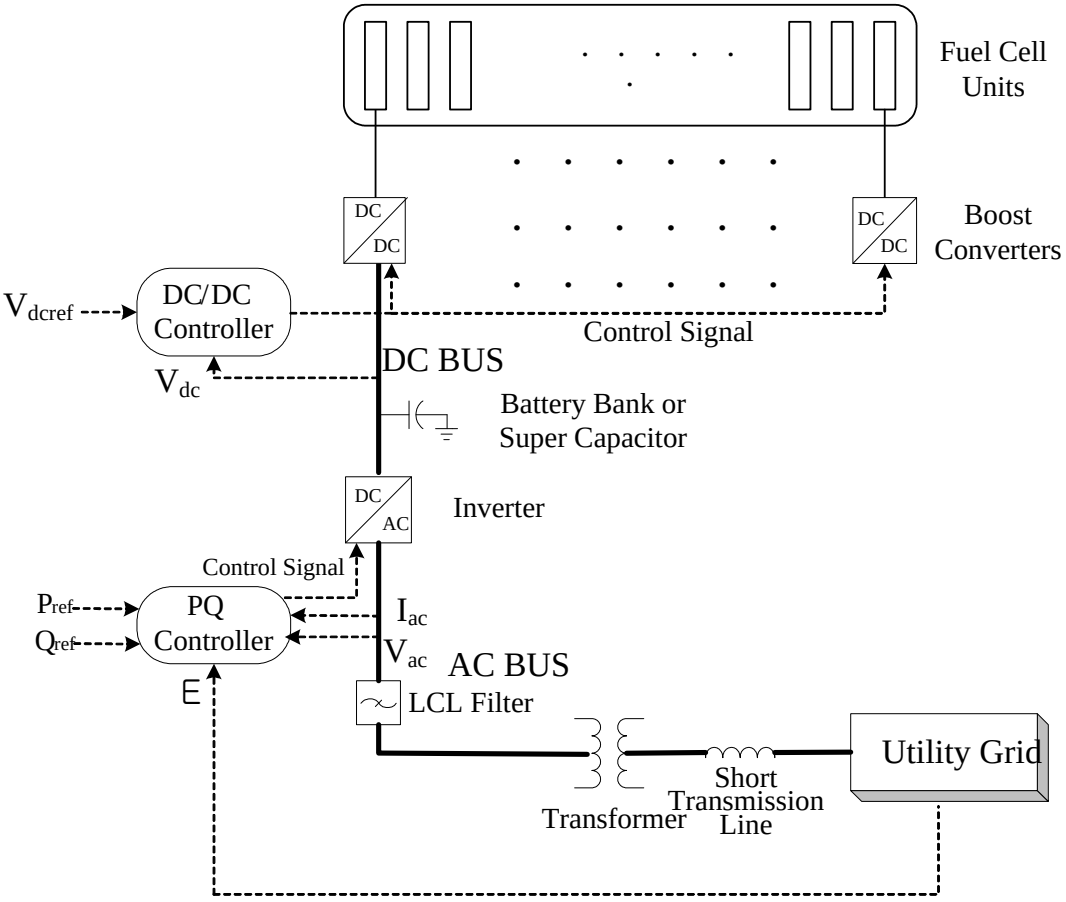

Figure 6.4. PCS-based interface to the utility grid.

The DC/AC inverter is a low cost inverter switched at the grid-line frequency. New solutions on the market are using PWM DC/AC inverters with IGBT switched typically at 10 to 20 kHz, leading to better power quality performance. The line filter

such as an L or LCL band pass filter is used to eliminate (or at least reduce) undesired harmonics of the PWM switching frequency. An energy storage device, e.g., a battery bank or super capacitor, is used to improve the performance of the FC power system under transient disturbances such as motor starting [72].

It is desirable for the PCS to provide galvanic isolation between the FC terminals and the grid. Hence, the PCS may include an inverter at the output of the FC, followed by a 50 or 60 Hz transformer (AC-AC voltage gain), or a switch-mode DC-DC converter at the FC (DC-DC voltage gain), followed by the grid-connected inverter. A switch-mode DC-DC converter employs high frequencies in the range of 20 to 100 kHz in order to keep the magnetic components compact.

FC can deliver the desired real and reactive power to the grid through a PCS, when a utility is operating under heavy load. With a FC power plant, a certain amount of power may be scheduled to be delivered to a load center from the utility grid, and the rest to be supplied by the FC system. A proper load-tracking controller can be used to ensure that the scheduled power is delivered from the grid, and that the FC system follows the remainder of the load demand.

The chemical response in the fuel processor is usually slow, as it is associated with the time needed for the chemical reaction parameters to change after a change in the flow reactants. The overall time constant of the combined FC and processor system is typically on the order of several tens of seconds and therefore is at least two orders of magnitude slower than the typical response times of the power converters in the PCS. Hence, to control the setpoint variables of the FC in power demand variations it is

customary to ignore the fast dynamics of the PCS, which can be represented as a first order lag with a time constant not exceeding 0.1 s.

6.3.3 Control Schemes of the PCS

The control block diagram of the PCS is illustrated in Figure 6.5, where there are two control systems [73]. One is related to control the FC current and the other is related to the grid interface. Input to the FC current controller for the DC/DC converter is the FC current reference I_{sys_ref}, which is the setpoint value, $r_{10,}$ of the tenth control loop at Table 3.1 in the Chapter 3. Generally, the FC current controller is a type of PI or PID controller.

The voltage controller for the DC/AC inverter maintains the DC-link capacitor voltage at a given rated value for the AC grid voltage. Its output is the desired grid current, proportional to the inverter output power. In order to synchronize the injected grid current with the grid voltage (to achieve unity power factor), the phase of the reference current is taken from the grid voltage, calculated by the Phase Lock Loop (PLL) block. The AC current controller controls the grid current output to follow the reference of PQ (real and reactive) powers. The details of PQ power control will be addressed in the next section.

A FC stack can be performed to operate at an optimal fuel utilization point, which is 75% in the SCDP power plant. This optimal fuel utilization can be achieved from (3.41) by controlling the DC current of the FC power plant, I_{sys_act}. The current reference input I_{sys_ref} is obtained by dividing the power demand of the FC power plant with the stack output voltage. Hence, the FC control problem is translated into an output current

control requirement in order to ensure optimal operation for a given fuel flow rate. Under these conditions, the fuel cell output power is directly related to its fuel consumption at the selected operating point of the V-I characteristic in Figure 3.2.

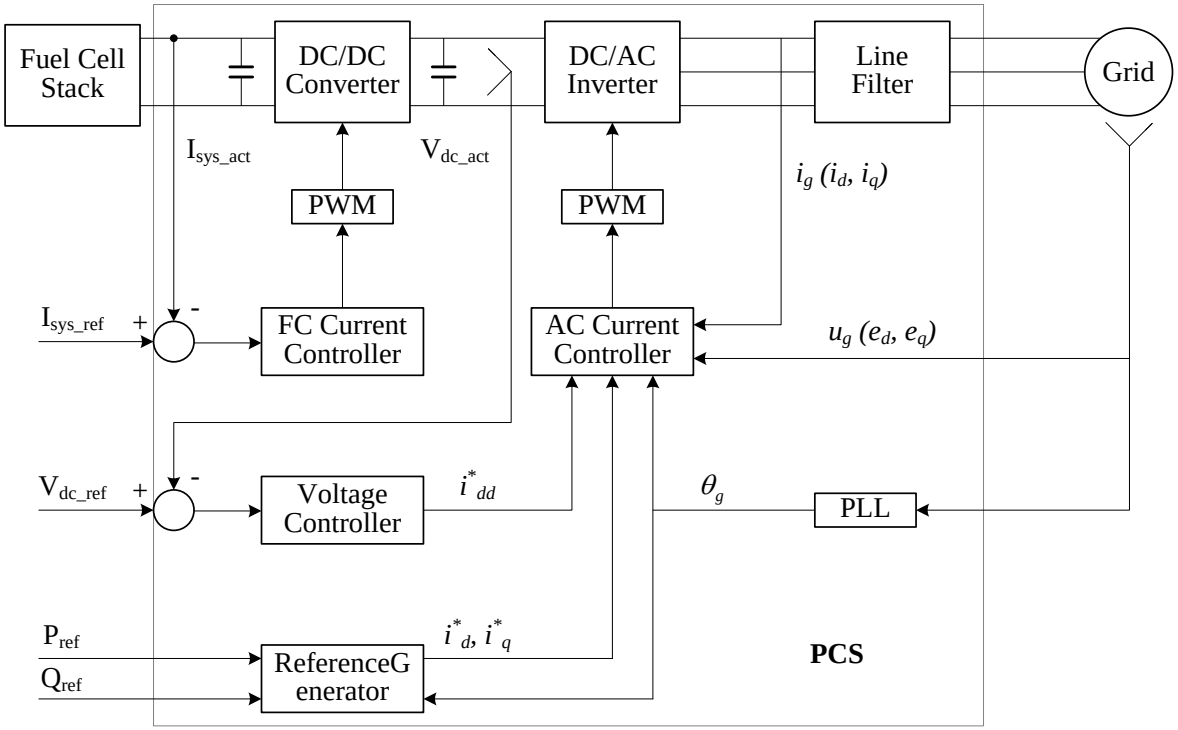

Figure 6.5. Basic control schemes of the PCS interface to the utility grid.

6.3.4 Reduction of THD and PWM Switching noises

In order to lower the transmitted high frequency current ripple caused by the PWM switched operation of the inverter, L or LCL filters are inserted between the inverter and the grid. The L-filter is a first order filter, and its attenuation is 20dB/decade over the whole frequency range. Using this filter, the switching frequency of the inverter

has to be high to obtain sufficient attenuation of the harmonics caused by the PWM inverter.

The new trend is to use an LCL filter as shown in Figure 6.6 [74]-[75]. I*c* is the output current from DC/AC inverter and it becomes the input current to the LCL filter. The drawback is that due to its own resonance frequency it can produce stability problems, and special control design is required.

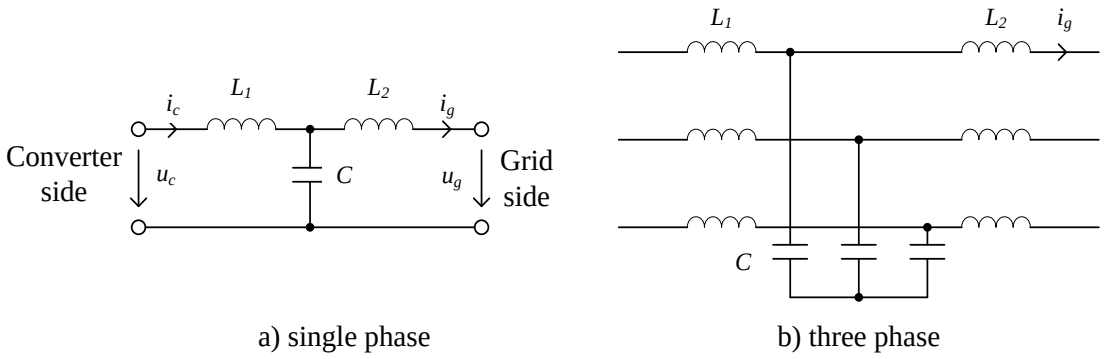

a) single phase b) three phase

Figure 6.6. The LCL line filters.

The transfer function of the LCL filter given by the grid side current to the converter side voltage is:

$$G(s) = \frac{I_g(s)}{U_c(s)} = \frac{1}{L_1 L_2 C s} \frac{1}{s^2 + \omega_{res}^2}, \tag{6.1}$$

where the resonance frequency $\omega_{res} = 2\pi f_{res}$ depends only on values of the filter components.

$$f_{res} = \frac{1}{2\pi} \sqrt{\frac{L_1 + L_2}{L_1 L_2 C}}. \tag{6.2}$$

The series resistances of inductors are neglected for simplicity. The main advantages of the LCL filter are low grid distortion and reactive power production, attenuation of 60dB/decade for frequencies above the resonance frequency, and the possibility of a relatively low switching frequency.

The frequency responses of L and LCL filters are plotted in Figure 6.7. It is shown that the two filters have the same attenuation below the resonance frequency. For this frequency range, the LCL-filter can be regarded as an L filter with an inductance of $L_1 + L_2$. However, the difference in the attenuation indicates that the sum $L_1 + L_2$ is smaller than the L filter inductance L. Consequently, the voltage drop across the LCL filter, caused by the injected current harmonics, is lower compared to the L filter case.

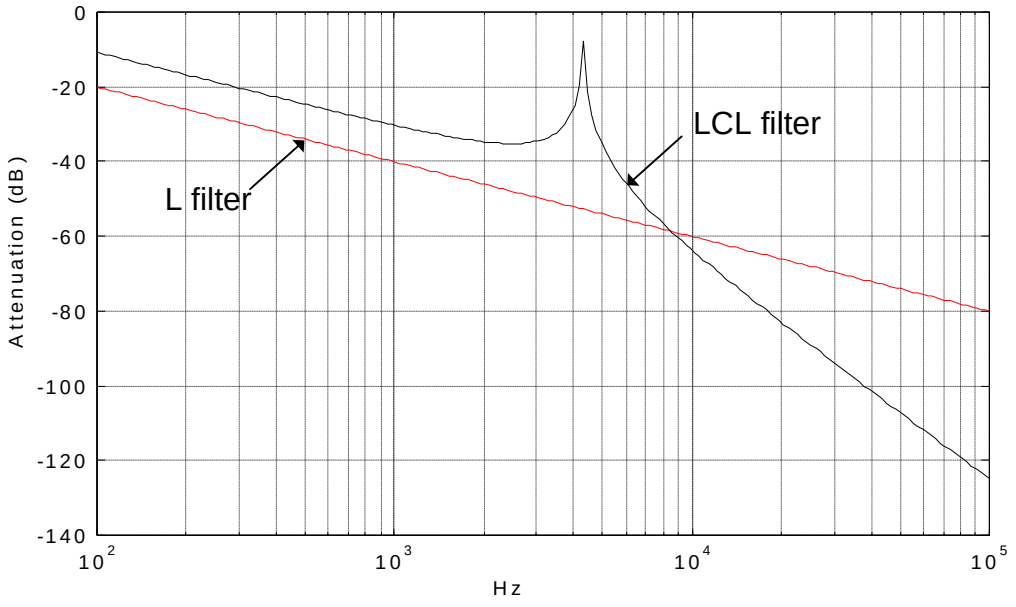

Figure 6.7. Frequency responses of L filter and LCL filter.

6.3.5 Reduction of harmonic frequencies

The grid voltage is usually affected by a background distortion that can result in a high harmonic distortion of the grid current. Harmonic levels of the grid-line frequency is still a controversial issue for FC inverters. Total harmonic distortion (THD) of the grid-line frequency, which applies to both current and voltage, is defined as the ratio of the rms value of harmonics and rms value of the fundamental grid-line frequency. THD of voltage calculation is as follows:

$$V^2 = V_1^2 + V_H^2, \tag{6.3}$$

where V , V_1 and V_H are the rms value of a voltage waveform, the fundamental and harmonic components, respectively. THD is calculated as the ratio of harmonic voltage to fundamental expressed as a percentage:

$$\text{THD} = \frac{\text{V}_\text{H}}{\text{V}_1} \times 100\,. \tag{6.4}$$

Voltage THDs below 5% are widely considered to be acceptable, but values above 10% are unacceptable and will cause problems for sensitive equipment and loads. The IEEE 529 standard allows a limit of 5% for the current THD factor with individual limits of 4% for each odd harmonic from 3rd to 9th and 2% for 11th to 15th. These levels are far more stringent than other domestic appliances such as IEC 61000-3-2, as photo-voltaic systems are viewed as generation sources and so are subject to higher standards than load systems.

The AC current controller in Figure 6.5 requires an improved control algorithm in order to obtain compliance with the power quality standards IEEE 529. A classical proportional integral (PI) controller will fail in the case of voltage harmonic distortion

[76]. The use of a second order integrator offers higher performances than the PI, considering the theoretically infinite gain at the resonant frequency. Thus, by choosing the resonant frequency in an appropriate manner, it can be used also for selective harmonic compensation.

Proportional resonant (PR) and harmonic compensation (HC) controllers as reported [76]-[77] can instead be used both for a good tracking performance of the grid-line frequency reference and for harmonic compensation. They do not exhibit stationary error and provide rejection of higher harmonic disturbances. The AC current control loop using the PR and the HC controllers is shown in Figure 6.8, where ε is current disturbance for the system and u_g is the grid voltage. A processing delay typically equal to the switching time interval for the PWM inverters is introduced in $G_d(s)$. The transfer function of the PR controller $G_r(s)$ is expressed as

$$G_r(s) = K_p + K_i \frac{s}{s^2 + \omega_0^2}, \tag{6.5}$$

where K_p is the proportional gain, K_i is the integral gain, and ω_0 is the resonance frequency [76]-[77]. The transfer function of the HC controller $G_h(s)$ for harmonics third, fifth, and seventh is defined as

$$G_h(s) = \sum_{h=3,5,7} \frac{K_h s}{s^2 + (h\omega_0)^2}, \tag{6.6}$$

where K_h $(h = 3,5,7)$ are the compensation Gains and are the most prominent harmonics in the current spectrum [76].

The current error–disturbance ratio rejection capability at null reference (i^*_g = 0) is defined as [76]

$$\frac{\varepsilon(s)}{U_g(s)} = \frac{G_f(s)}{1+(G_r(s)+G_h(s))\cdot G_d(s)\cdot G_f(s)} \tag{6.7}$$

where G_f(s) is the transfer function of the LCL filter given by the converter side current to the converter side voltage in Figure 6.6:

$$G_f(s) = \frac{I_c(s)}{U_c(s)} = \frac{1}{L_1 L_2 C s}\frac{s^2+1/L_1C}{s^2+\omega_{res}^2}. \tag{6.8}$$

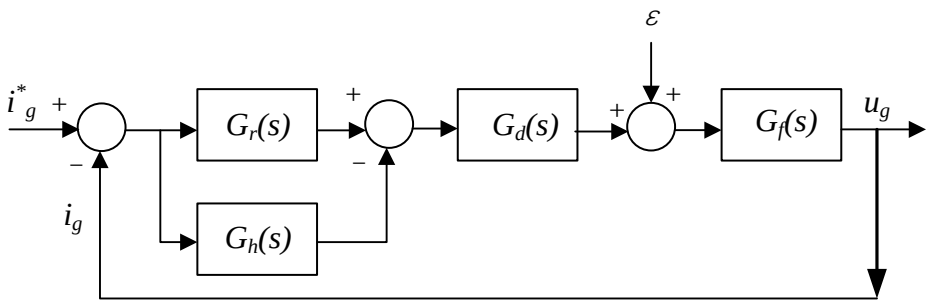

Figure 6.8. Current loop of FC-inverter with PR and HC controllers.

Frequency responses of the disturbance rejection for the PR and HC controllers are shown in Figure 6.9, where frequency responses of the disturbance rejections for PI controllers are also shown for comparison purposes. The double integrators of the PR and HC controllers in (6.5) and (6.6) achieve an infinite gain at the resonance frequency and its third, fifth, and seventh harmonics. As it can be observed, the PR and HC controllers provide much higher attenuation for the fundamental and harmonic frequencies than PI controllers. Hence, an HC controller can be used as a notch filter in order to compensate the harmonics in a very selective way. Thus, the FC inverter with PWM can reduce the

THD effectively without alteration of the system dynamics by adding the harmonic compensators for selected harmonics frequencies.

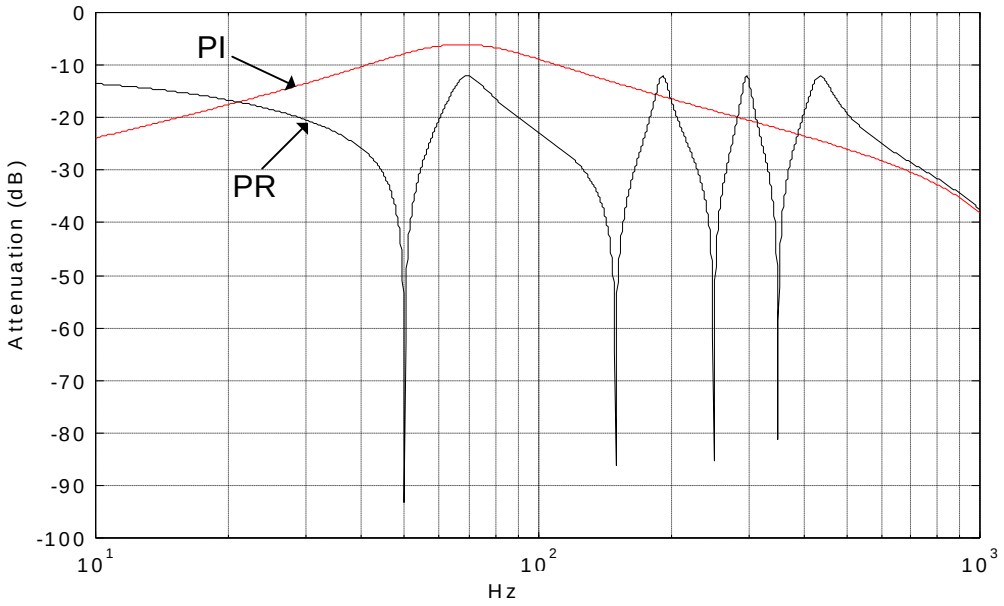

Figure 6.9. Frequency responses of disturbance rejection (current error ratio disturbance)

6.4 Power Control of a Fuel Cell Power Plant

The real and reactive powers in the FC plant are controlled quantities by means of the inverter. To prevent over-loading of the inverter and the fuel cell plant, it is important to ensure that load changes are taken up by the inverter in a predetermined manner.

The control of inverters used to supply power to an AC system in a distributed environment should be based on information available locally at the inverter. In a system with many micro-sources, the communication for information between systems is impractical. The communication for information may be used to enhance system

performance but must not be critical for system operation. Essentially this implies that the inverter control should be based on terminal quantities.

6.4.1 Basic Structure of the Power Control

The basic structure of the Voltage Source Inverter (VSI) P-Q controller in the simplest way is shown in Figure 6.10 [78]-[81]. If the details of inverter switching are considered, then extra effort would be required to compensate for the undesired effects of generated harmonics, and the result would be a slower computer simulation. Therefore, an ideal model is considered for VSI, and the inverter voltage is represented using three controlled sinusoidal voltage sources defined as [78]-[79]:

$$\begin{aligned} v_a &= \sqrt{2}\ V\sin(wt+\delta_V), \\ v_b &= \sqrt{2}\ V\sin(wt+\delta_V-2\pi/3), \\ v_c &= \sqrt{2}\ V\sin(wt+\delta_V+2\pi/3). \end{aligned} \tag{6.9}$$

Here, V and E are the voltages (rms value) of the inverter output and the AC system, respectively. δ_V and δ_E is the phase angles of inverter output voltage and AC system voltage, respectively.

Real and reactive powers can be controlled independently to a good extent. Two PI controllers would suffice to control the flow of real and reactive powers by generating the proper values for two variables of V and δ_V. The vector is controlled so as to have a specified magnitude and a specified position relative to the AC system flux. This control forms the innermost control loop and is very fast. The inverter and AC

system voltage space vectors are obtained from instantaneous voltage measurements and are available locally.

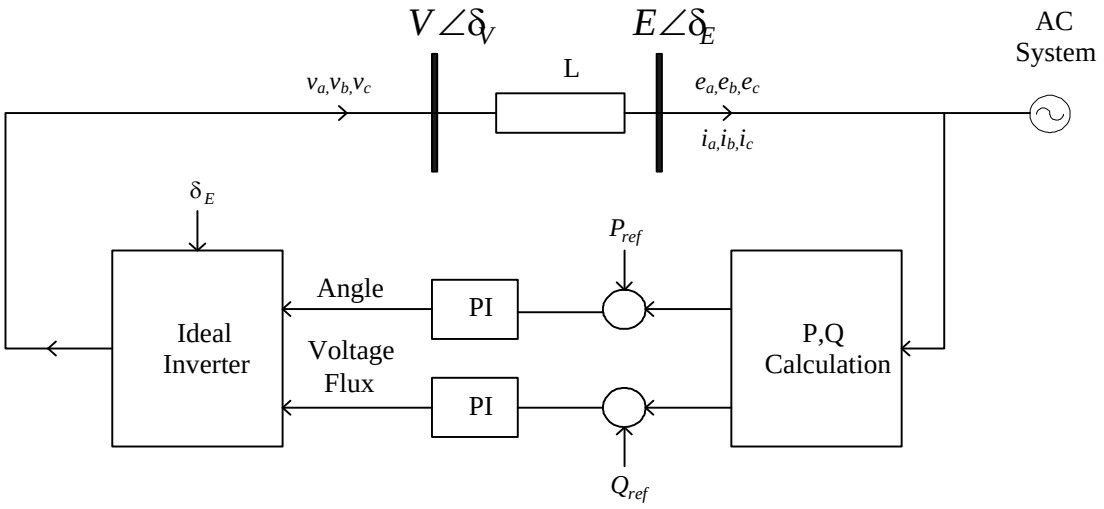

Figure 6.10. Basic structure of the inverter control scheme.

The P-Q theory implements a transformation from a stationary reference system in a-b-c coordinates, to a system with coordinates α-β-0, where coordinates α-β are orthogonal to each other, and coordinate 0 corresponds to the zero-sequence component.

$$\begin{bmatrix} v_\alpha \\ v_\beta \\ v_0 \end{bmatrix} = \sqrt{\frac{2}{3}} \begin{bmatrix} 1 & -1/2 & -1/2 \\ 0 & \sqrt{3}/2 & \sqrt{3}/2 \\ 1/\sqrt{2} & 1/\sqrt{2} & 1/\sqrt{2} \end{bmatrix} \begin{bmatrix} v_a \\ v_b \\ v_c \end{bmatrix} \tag{6.10}$$

The α-β coordinates are transformed to the d-q coordinates that rotate at the angular fundamental frequency ω of the grid voltage waveform. The state-vectors which express the inverter electrical quantities are projected on the d-axis and q-axis.

$$\begin{bmatrix} v_d \\ v_q \end{bmatrix} = R(-\omega t) \begin{bmatrix} v_\alpha \\ v_\beta \end{bmatrix}, \quad R(\omega t) = \begin{bmatrix} \cos\omega t & -\sin\omega t \\ \sin\omega t & \cos\omega t \end{bmatrix}. \tag{6.11}$$

If the inverter is connected to the grid through L-filter as shown in Figure 6.8, then in the d-q frame rotating at the angular speed ω,

$$\frac{d}{dt}\left(R(\omega t)\begin{bmatrix} i_d \\ i_q \end{bmatrix}\right) = \frac{1}{L} R(\omega t)\left(\begin{bmatrix} v_d \\ v_q \end{bmatrix} - \begin{bmatrix} e_d \\ e_q \end{bmatrix}\right). \tag{6.12}$$

The above equation can be rewritten as follow:

$$\frac{d}{dt}\begin{bmatrix} i_d \\ i_q \end{bmatrix} = \frac{1}{L}\begin{bmatrix} v_d \\ v_q \end{bmatrix} + \omega\begin{bmatrix} i_q \\ -i_d \end{bmatrix} - \frac{1}{L}\begin{bmatrix} e_d \\ e_q \end{bmatrix}. \tag{6.13}$$

The inverter is controlled using the time-integral of the d-q space vector. The resulting d-q components are time integrated, resulting in the flux vectors in PI controller inputs, for the inverter and AC system voltages. The P-Q power control is implemented through the AC current controller in Figure 6.5. The block diagram of the P-Q controller is shown in Figure 6.11.

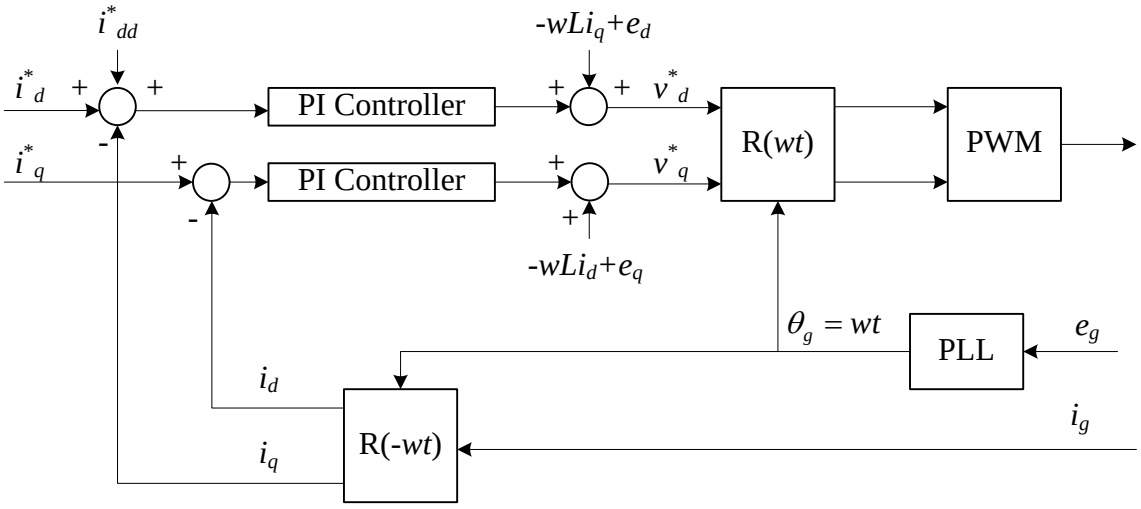

Figure 6.11. The PQ Power Control based on the Use of a Rotating d-q Frame.

6.4.2 Theoretical Considerations on P-Q Control

The basic requirement of voltage source inverters is to control the flow of real and reactive powers between the fuel cell and AC power system. Therefore, the first step in studying the subject of generation control is to see which variables influence the flow of real and reactive powers.

The voltage source inverter controls both the magnitude and phase of its output voltage (V in Figure 6.10). The vector relationship between the inverter voltage (V) and the local microgrid voltage (E in Figure 6.10) along with the inductor's reactance determines the flow of real and reactive power from the microsource to the microgrid. The corresponding mathematical relations for P & Q magnitudes are as follows:

$$P = \frac{VE}{X}\sin(\delta_V - \delta_E), \tag{6.14}$$

$$Q = \frac{V^2}{X} - \frac{VE}{X}\cos(\delta_V - \delta_E) = \frac{V}{X}[V - E\cos(\delta_V - \delta_E)] \tag{6.15}$$

where P is the real power, Q is the reactive power, and X is the reactance.

Concerning the above expressions, the following points can be raised [72]-[81]:

- For small changes in angle, P is predominantly dependent on the power angle difference $(\delta = \delta_V - \delta_E)$, and Q is dependent on the voltage magnitude difference (V-E). As a consequence, the control of real and reactive power flow is reduced to the control of the power angle and the voltage level of the inverter. Therefore, power angle and voltage level would be the critical variables for real and reactive power flow control.

- Although the flow of real and reactive power is not completely decoupled, they are fairly independent. In other words, the control of each one has only a minor impact on the other one.

In the case of the d-q frame, if the d-axis is aligned to the grid voltage, the reference current d-component i^*_d is controlled to manage the real power flow, while the reference current q-component i^*_q is controlled to manage the reactive power flow. The reference current q-component should be zero in order to have the grid currents in phase with the grid voltage.

A high harmonic distortion of the grid current usually has an effect on the grid voltage. This problem can be solved both in a stationary α-β frame and in a rotating d-q frame. In the case of the stationary α-β frame, it is sufficient to plug in controllers of PR in (6-5) and HC in (6-6). If the AC current controller adopts a rotating d-q frame approach, it is possible to introduce other d-q frame rotating at multiple speed respect to the fundamental one and adopting standard PI in each of them.

6.4.3 P-Q Control Simulation of a FC power Plant

Figure 6.12 shows the matlab/simulink model of the inverter-connected SCDP fuel cell power plant model. The inverter simulink model is connected to the original SCDP model and simulated together using the same solver and step size. A detailed scheme of this inverter model is shown in Figure 6.13, including the voltage regulator, Pulse Width Modulation (PWM) generator, and Insulated Gate Bipolar Transistor (IGBT) inverter models.

Once the desired P and Q values are set for three different cases, the corresponding control values of voltage and angle are calculated using equation (6.14) and (6.15). Figure 6.14 shows a simulation diagram and the corresponding voltage and angle are calculated according to P and Q values previously set for each case. The inverter control variables of voltage and angle are converted to Vd_ref and Vq_ref using equation (6.11). These reference d-q components of desired P and Q value are regulated with PI controllers in Figure 6.11 and the diagram of the PQ regulator is shown in Figure 6.15. The gains of PI controllers are determined by trial and error for each case. The simulation results also indicate that P and Q values are under damped as the proportional gain of Kp is greater than 3.6 for each different cases.

As the P-Q control using current controllers requires considerable computational time connected to the SCDP model, a simplified method using (6.14) and (6.15) is used for a matlab/simulink model. Figures 6.16-18 show the simulation results for three different cases according to the load change of the utility grid as follows:

1) Case 1

For the first case study, the real power is set to P = 0.8 pu and the reactive power Q = 0.0 pu. According to the simulation diagram of Figure 6.14, the corresponding voltage and angle are calculated as Vs = 1.0335 pu and δ =0.2554 radians. For the following step, the inverter control variables of voltage and angle are converted to Vd_ref and Vq_ref using equation (6.11). These reference d-q components for the desired P and

Q values are regulated in the voltage regulator of Figure 6.15 using a PI controller. The gains of the PI controller are Kp= 3.0 and Ki=0.00001.

2) Case 2

For the second case study, the real power is increased to P = 1.0 pu and the reactive power is set to Q = 0.2 pu for an inductive load. According to the simulation diagram of Figure 6.14, the corresponding voltage and angle are calculated as Vs = 1.0841 pu and δ =0.2432 radians. The inverter control variables of voltage and angle are converted to Vd_ref and Vq_ref using equation (6.11). These reference d-q components for the desired P and Q values are regulated in Figure 6.15 using PI controller. The gains of PI controller are Kp= 2.6 and Ki=0.00001.

2) Case 3

For the third case study, the real power is set to P = 1.0 pu and the reactive power is changed to Q = - 0.2 pu for a capacitive load. According to the simulation diagram of Figure 6.14, the corresponding voltage and angle are calculated as Vs = 0.9831 pu and δ =0.2688 radians. The inverter control variables of voltage and angle are converted to Vd_ref and Vq_ref using equation (6.11). These reference d-q components for the desired P and Q values are regulated in Figure 6.15 using PI controller. The gains of PI controller are Kp= 3.6 and Ki=0.00001.

For each different case, the inverter controller shows satisfactory results following the real and reactive power change of a load.

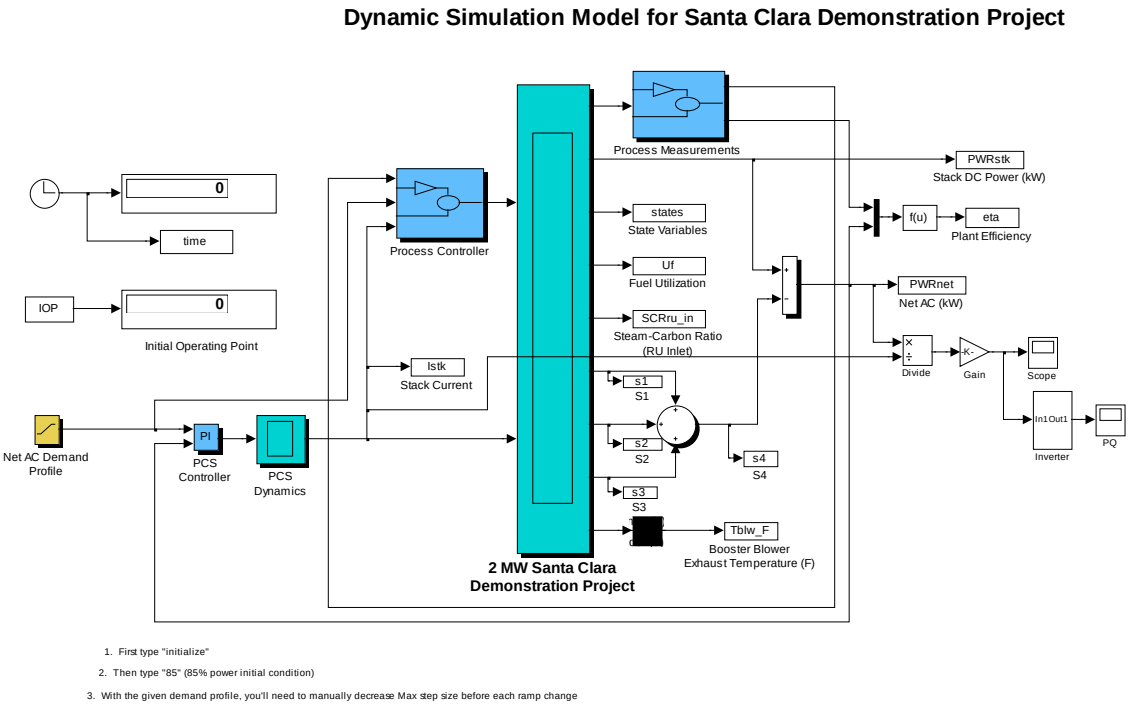

Figure 6.12. Inverter-connected SCDP FC power plant model.

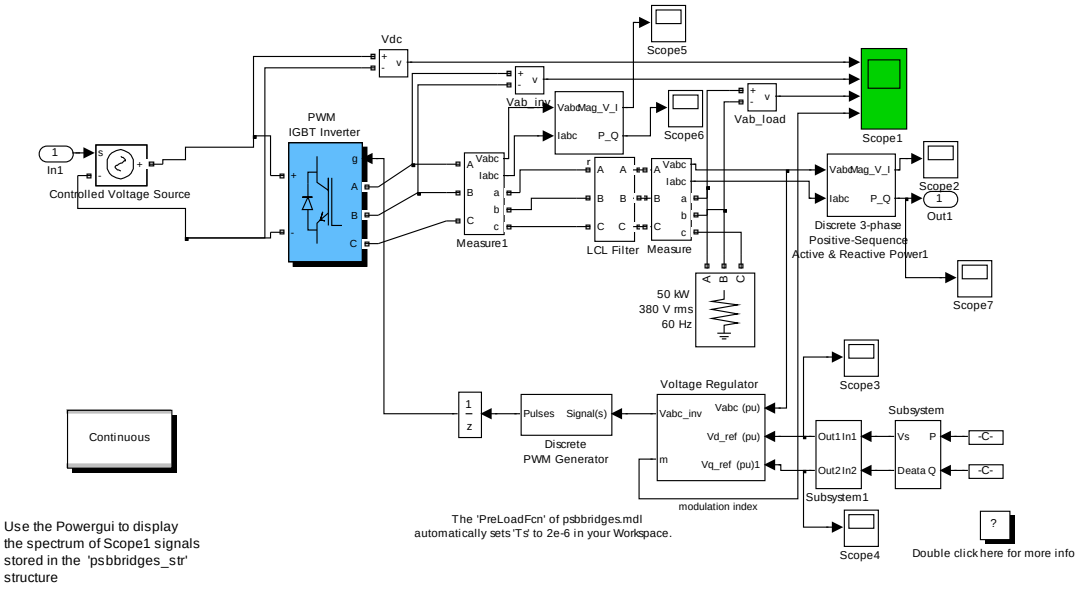

Figure 6.13. Detailed scheme of inverter model.

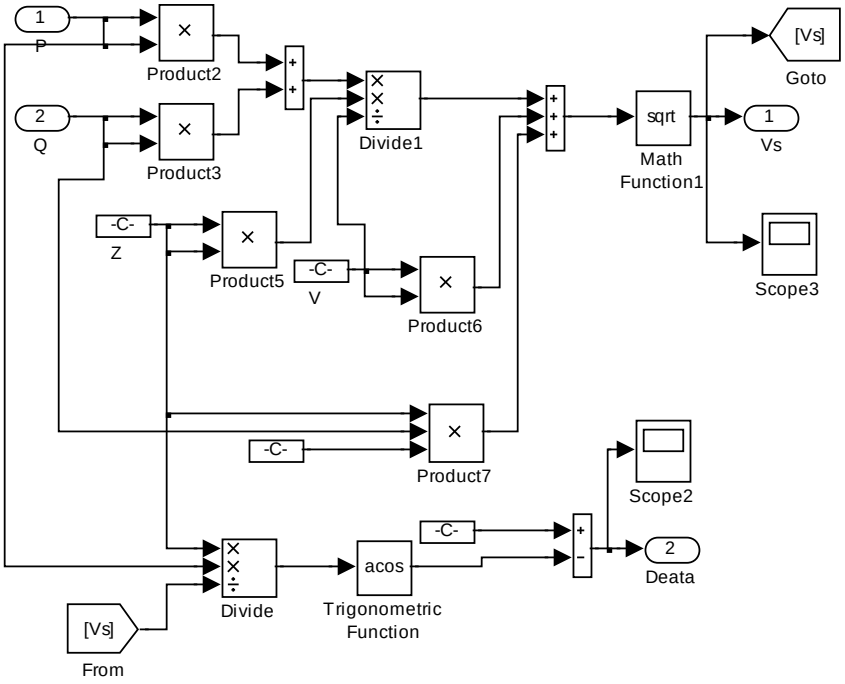

Figure 6.14. Measurement of voltage and angle.

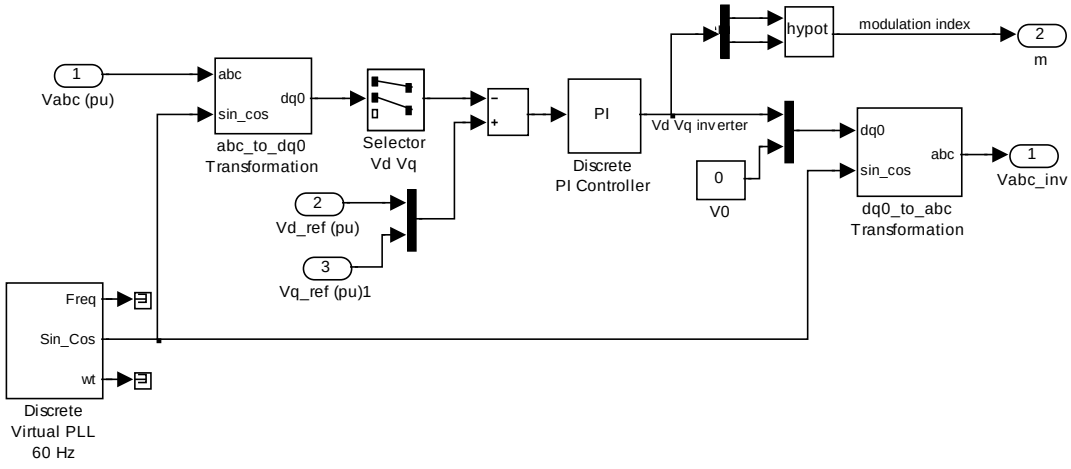

Figure 6.15. Diagram of PQ regulation with PI voltage controller.

Case study 1 : P = 0.8 pu, Q = 0.0 pu

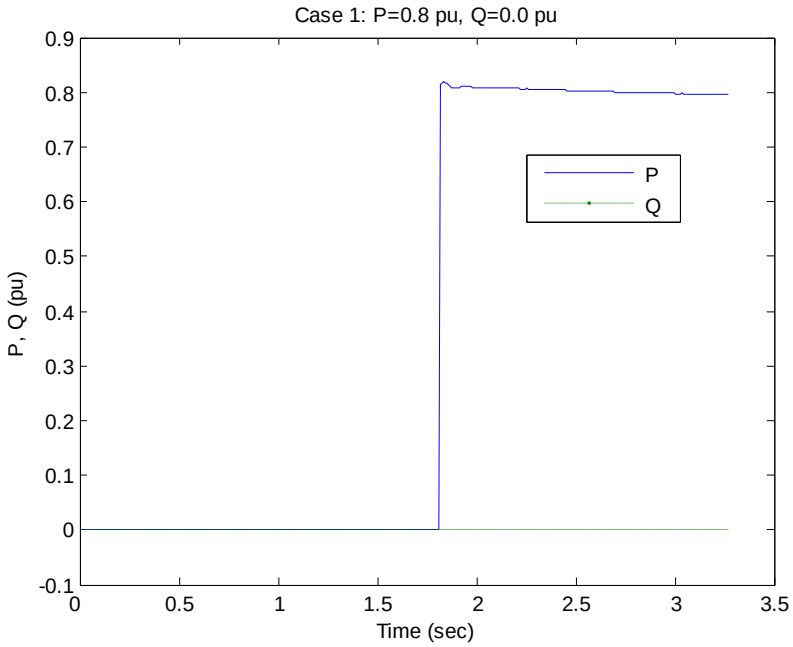

Figure 6.16. Case study 1: P = 0.8 pu, Q = 0.0 pu

Case study 2: P = 1.0 pu, Q = 0.2 pu

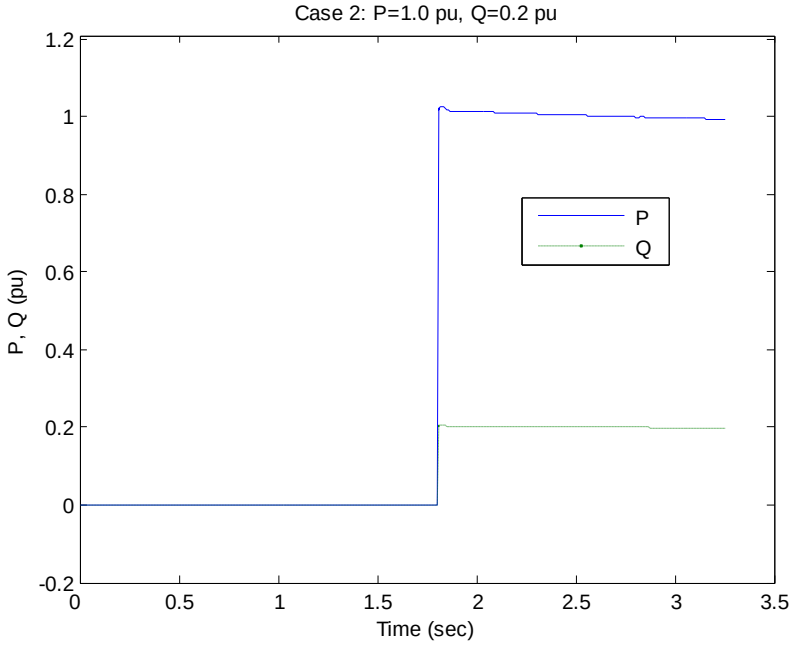

Figure 6.17. Case study 2: P = 1.0 pu, Q = 0.2 pu.

Case study 3: P=1.0 pu, Q= -0.2 pu

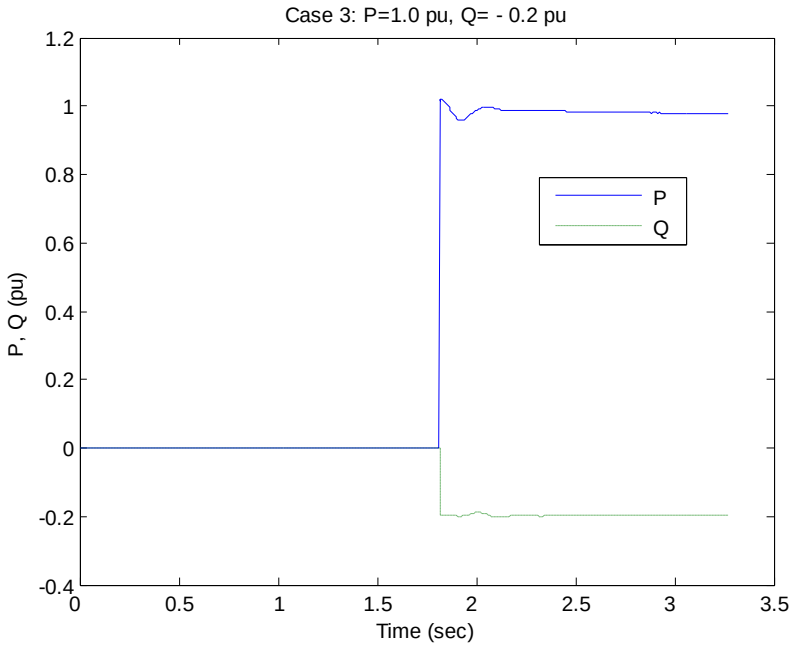

Figure 6.18. Case study 3: P = 1.0 pu, Q = - 0.2 pu

6.5 Simulations of FC Power Plants in a Real Distribution Network

The performance of a FC power plant is simulated through a real distribution network when it is connected to the utility grid. The simulations are performed using Hypersim software program, which is developed for power flow simulation based on matlab/simulink software. A branch office of Korea Electric Power Corporation (KEPCO) is used as the real distribution network for the simulations.

6.5.1 Simulation Environments

Figure 6.19 shows a real distribution network of a Goyang Branch Office of KEPCO, and a simulation model from Hypersim is plotted in Figure 6.20. A FC model is specially designed for this program using several parameters including generating capacity and time constant. The maximum capacity of a FC DG is assumed to be 3,000 kW considering the regulation of KEPCO: 30 % of a maximum distribution line capacity. Therefore, a fuel cell power plants with two different capacities of 1,000 kW and 3,000 kW are supposed to be installed in a 22,9 kV distribution network.

Distribution line impedance and load data are shown in Table 6.3. Positive sequence and zero sequence values are given according to the wire: CN (Concentric Neutral) cable and EW (Extra High Voltage Aluminum Wire). The distribution line is divided into 5 load sections, and their power factors are assumed to be 0.9.

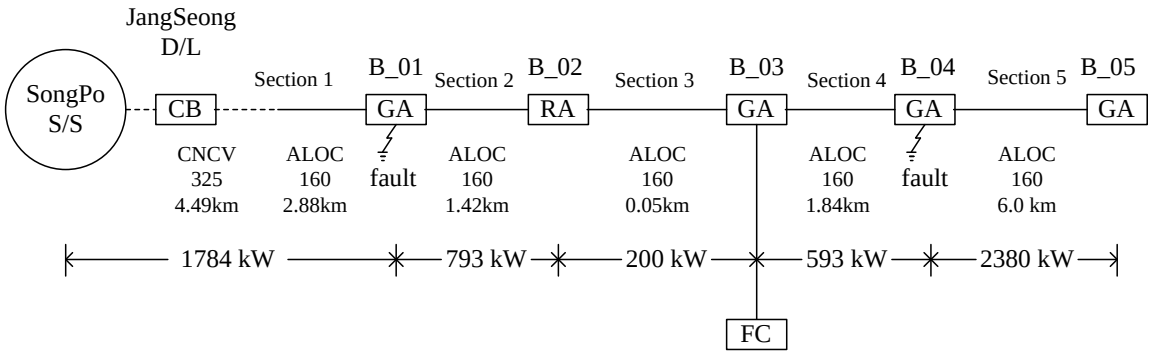

S/S: Substation, D/L: Distribution Line,
CB: Circuit Breaker, RA: Recloser_Automatic, GA: Gas Switch_Automatic, FC: Fuel Cell power plant
---- CNCV: Concentric Neutral Cross-linked polyethylene insulated Vinyl sheathed Cable,
— ALOC: Aluminum Conductor steel reinforced Outdoor Closs-linked Wire for 22.9kV

Figure 6.19. Single line diagram of a distribution network model.

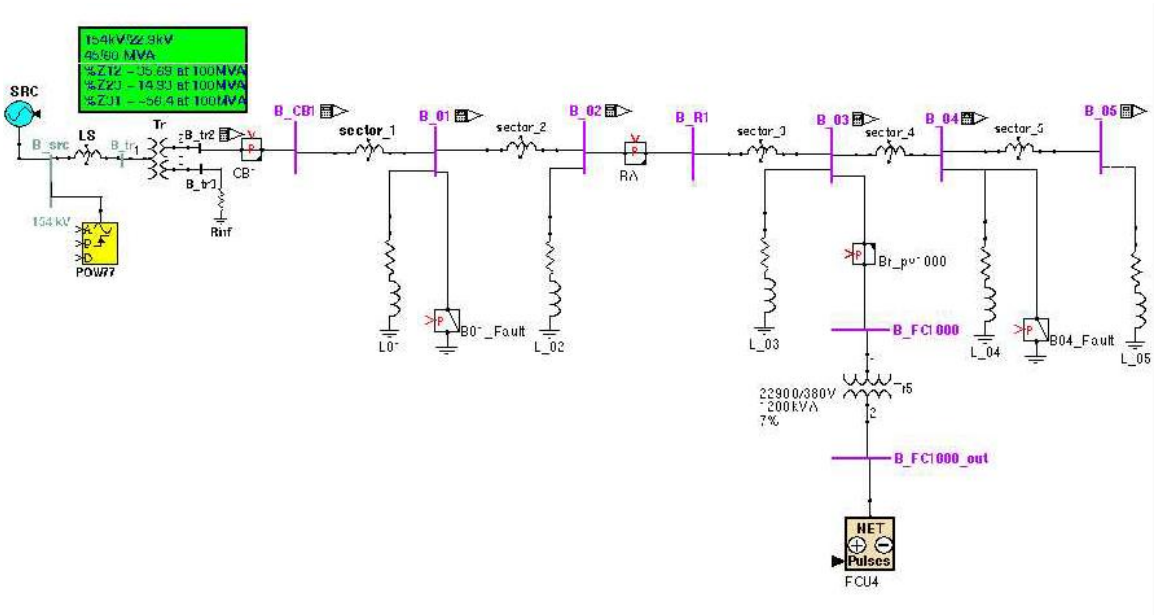

Figure 6.20. Simulation model on Hypersim program for a distribution network.

Table 6.3. Distribution line impedance and load data.

Positive Sequence Impedance

section	wire	%R/km	%X/km	km	%R	%X
B_01	CN325	1.7906	2.8451	4.49	8.040	12.774
	EW160	3.86	7.42	0.48	1.853	3.562
B_02	EW160	3.86	7.42	0.2	0.772	1.484
B_03	EW160	3.86	7.42	0.054	0.208	0.401
B_04	EW160	3.86	7.42	0.1	0.386	0.742
B_05	EW160	3.86	7.42	6	23.160	44.520

Zero Sequence Impedance

section	wire	%R/km	%X/km	km	%R	%X
B_01	CN325	5.3222	1.7353	4.49	23.897	7.791
	EW160	9.87	22.68	0.48	4.738	10.886
B_02	EW160	9.87	22.68	0.2	1.974	4.536
B_03	EW160	9.87	22.68	0.054	0.533	1.225
B_04	EW160	9.87	22.68	0.1	0.987	2.268
B_05	EW160	9.87	22.68	6	59.220	136.080

Load Data

section	P (kW)	Q (kVAr)	power factor
B_01	1784	862	0.9
B_02	793	383	0.9
B_03	200	97	0.9
B_04	593	286	0.9
B_05	2380	1150	0.9
Total	5750	2778	0.9

6.5.2 Load Sharing between FC power plant and Distribution Network

The load sharing between the FC and distribution network is shown in Figures 6.21 ~ 6.23 with ripples caused by the PWM switched operation of the inverter. The real power of 5,750 kW is delivered to the circuit breaker (CB) side from the utility in Figure 6.19. Some of this power is used through loads between the CB and recloser (RA), and then, its remainder is 3,173 kW at the RA side. When the fuel cell began to supply 1,000 kW real power, both 5,750 kW at the CB side and 3,173 kW at the RA side are reduced by 1,000 kW. This load sharing between the FC and distribution line is plotted in Figures 6.21 and 6.22, where the reactive powers are not affected by the FC because the FC supplies real power only. In the case of a FC failure, the power delivered from FC will be transferred to the network after the protector isolates the FC from the distribution line.

The voltage variation of this distribution network is investigated through simulations. The FC power plant is assumed to be installed at the section B_03: load center of the distribution line with five sections B_01~B_05. Simulation results of the

voltage variation are summarized in Table 6.4, which shows that the FC DG makes the voltage variation increase slightly. This indicates that the voltage variation due to the FC power can be ignored. All the voltage variation in Table 6.4 maintains adequate service levels within 2% voltage regulation.

Figure 6.23 shows case studies for increasing the load and changing the location of a FC. In Figure 6.23 (a), a FC 1,000 kW at B_01 is connected to the distribution network at t = 1 sec and the load at B_05 is increased by 1,000 kW at t = 2 sec. The increased load is supplied from distribution network, while the FC supplies 1,000 kW continuously. The real power at RA is not changed at t = 1 sec, because the FC is interfaced before the point of RA. In Figure 6.23 (b), a FC 1,000 kW at B_05 is connected to the distribution network at t = 1 sec, and the load at B_05 is increased by 1,000 kW at t = 2 sec and decreased by 1,000 kW at t = 3 sec. The real power at RA is changed similar to the one at CB, because the FC is interfaced after the point of RA. Simulation results show that the changes of load are followed successfully from the distribution network regardless of the location of a FC.

In Figure 6.23 (c), the real power from a FC at B_03 is increased to 3,000 kW at t = 1 sec and decreased to 1,000 kW at t = 2 sec. As the real power from a FC is changed, the distribution network supplied the rest of required power adaptively. Figure 6.23 (d) shows the case study of a FC failure. A FC is connected to the distribution network at t = 1 sec and disconnected at t = 2 sec due to a FC failure. The distribution network covers the real power lost by the FC failure. Table 6.5 shows the comparison of voltage drop

according to the locations of a FC. The voltage drop at B_01 is slightly bigger than the one at B_05, because much of the load is connected at B_05.

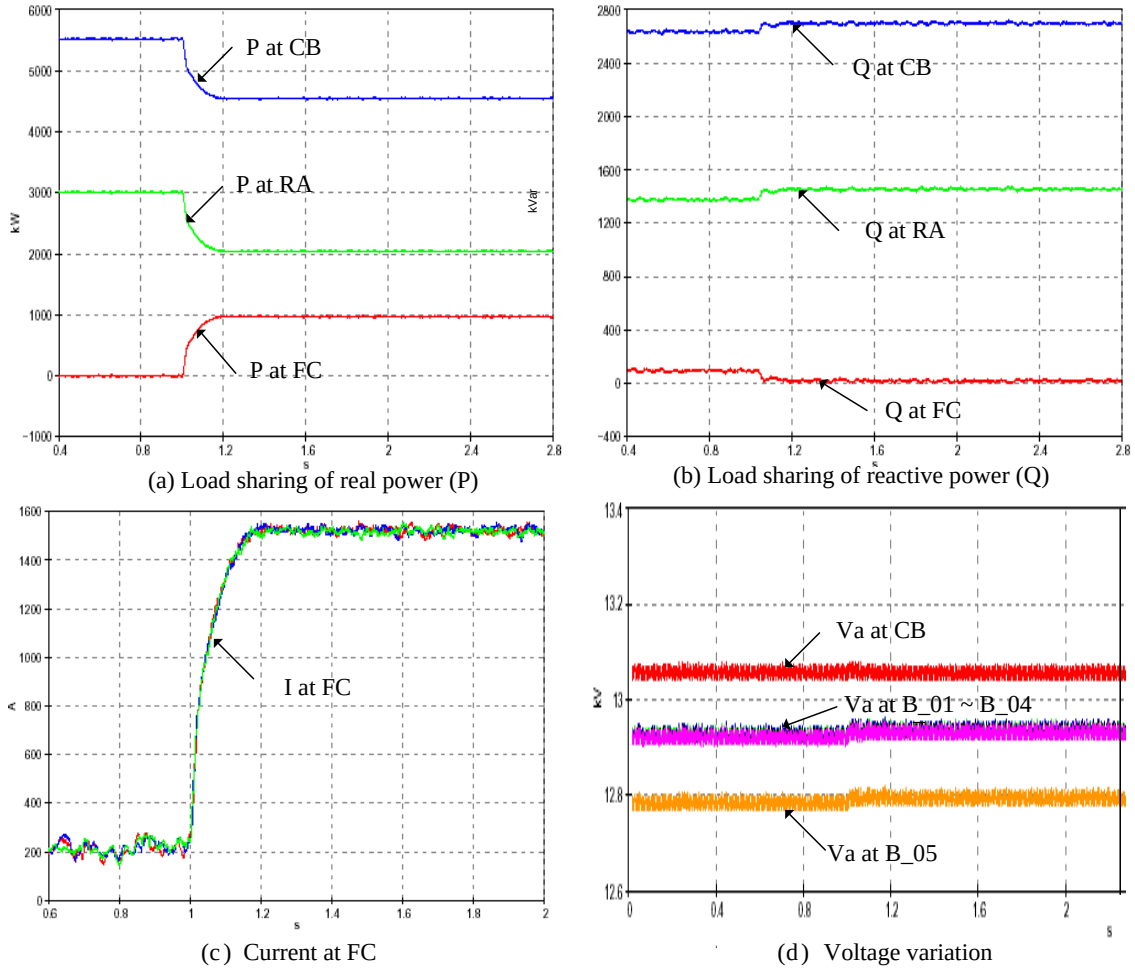

(a) Load sharing of real power (P)

(b) Load sharing of reactive power (Q)

(c) Current at FC

(d) Voltage variation

Figure 6.21. Load sharing with FC 1000 kW.

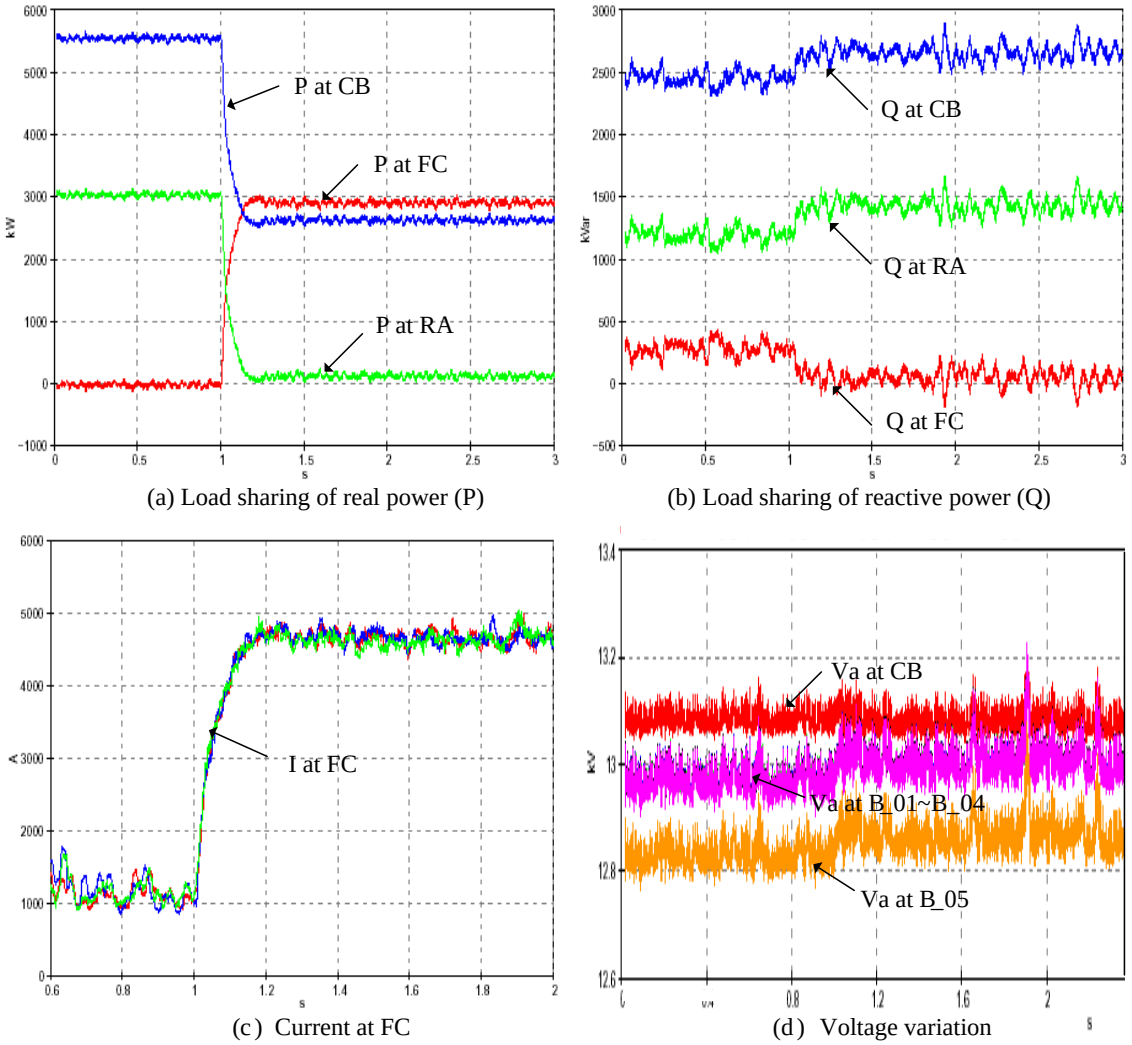

(a) Load sharing of real power (P)

(b) Load sharing of reactive power (Q)

(c) Current at FC

(d) Voltage variation

Figure 6.22. Load sharing with FC 3000 kW.

Table 6.4. Voltage variation due to FC interface.

section	without FC (V)	FC 1000kW (V)	FC 3000kW (V)
Va_B_CB1	13,057	13,056	13,060
Va_B_01	12,927	12,932	12,958
Va_B_02	12,924	12,929	12,956
Va_B_03	12,923	12,928	12,955
Va_B_04	12,920	12,925	12,953
Va_B_05	12,783	12,788	12,815

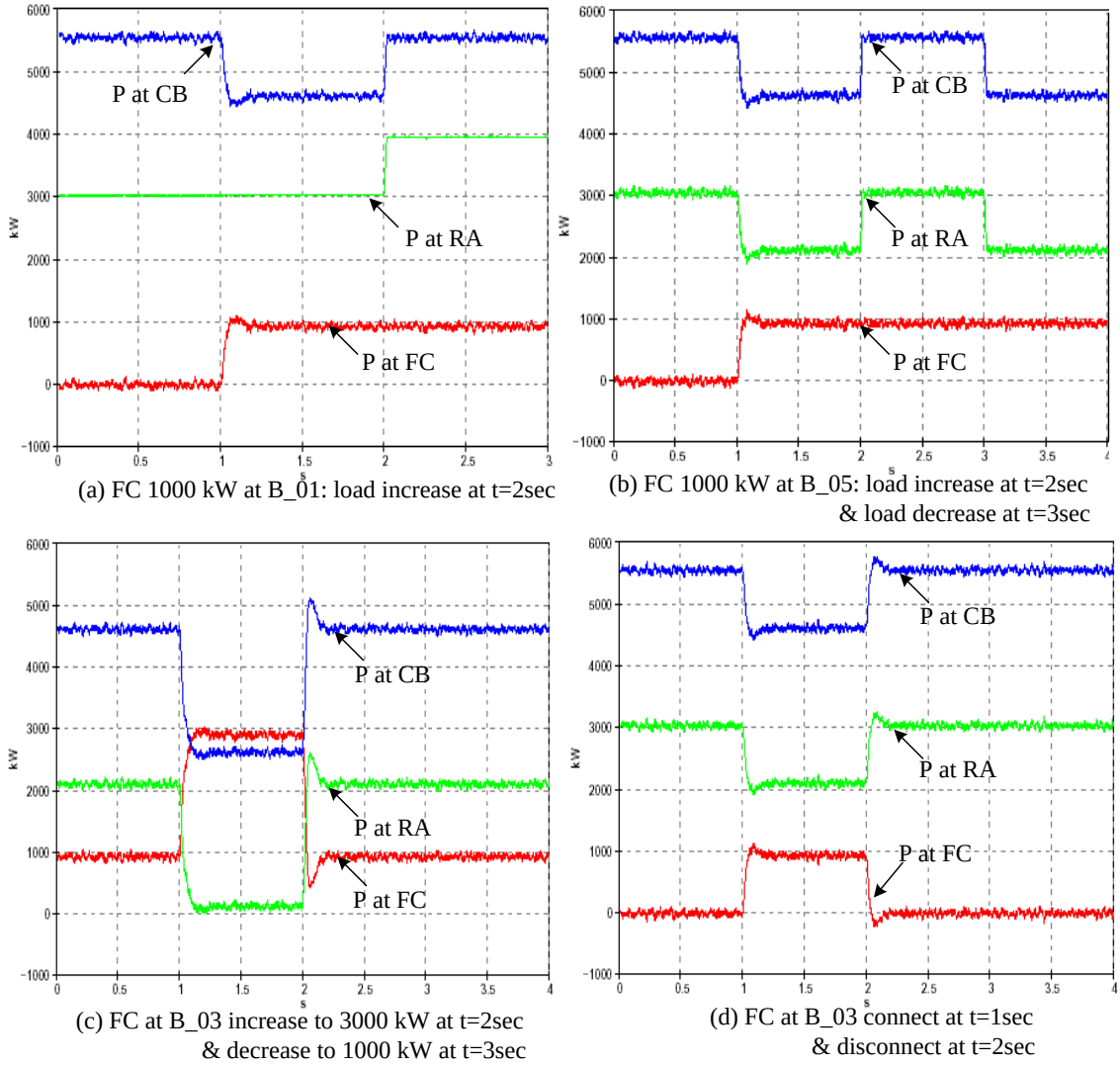

(a) FC 1000 kW at B_01: load increase at t=2sec

(b) FC 1000 kW at B_05: load increase at t=2sec & load decrease at t=3sec

(c) FC at B_03 increase to 3000 kW at t=2sec & decrease to 1000 kW at t=3sec

(d) FC at B_03 connect at t=1sec & disconnect at t=2sec

Figure 6.23. Increasing the load and changing the location of FC.

Table 6.5. Voltage Variation due to location of FC.

section	FC at B_01 (V)	FC at B_03 (V)	FC at B_05 (V)
Va_B_CB1	13,065	13,056	13,067
Va_B_01	12,945	12,932	12,958
Va_B_02	12,942	12,929	12,956
Va_B_03	12,940	12,928	12,955
Va_B_04	12,937	12,925	12,953
Va_B_05	12,770	12,788	12,879

6.5.3 Effect on Ground Fault with a FC Power Plant

A ground fault analysis in a real power system model is performed using the Hypersim software program to examine the effect to the distribution network when a FC power plant is added. A single line to ground fault is supposed to occur at two different points B_01 and B_04. It is assumed that the fault occurred at t = 1.5 sec and cleared at t = 1.6 sec after 0.1 sec.

For each fault point, three different cases are tested to compare the results: without a FC, a FC rated for 1000 kW, and a FC rated for 3,000 kW. Important concerns of transients during the fault are real power (P), reactive power (Q), voltage at fault, current at CB, RA and FC, etc. To protect distribution network facilities, the transients have to be sufficiently considered for the design of the breaker and fault processing sequence. The transients during the fault at B_01 are shown in Figures 6.24 ~ 6.26 and the ones at B_04 in Figures 6.27 ~ 6.29. Transients at B_01 and B_04 during the fault do not show any different effect on the power system network. However, Transients at B_04 show bigger voltage flickers than the ones at B_01 at the point of the fault.

During the simulations with FC switching and a line to ground fault, the effective grounding of the transformer at the interface between FC and distribution line can restrict the over-voltage caused by the fault, and any significant impact on FC power plant is not detected in Figures 6.24 ~ 6.29. With a successful analysis performed using a software program, simulation results prove that the penetration of a FC power plant does not bring any significant effect to the existing distribution network.

Figures 6.24 (a) and (b) show the transients of real and reactive power, respectively. The peak of transient values increases close to 4×10^4 kW and kVar temporarily and cleared by the circuit breaker (CB) after 0.1 sec. It is assumed that a single line to ground fault occurred at phase a. Figure 6.24 (c) shows the transients of the faulted phase voltage V*a* in rms value. V*a* drops to zero at t = 1.5 sec and is recovered at t = 1.6 sec. Figure 6.24 (d) shows the transients of the three phase voltages. The un-faulted two phase voltages V*b* and V*c* show slight variations temporarily during the fault and are recovered to normal values. Figure 6.24 (e) shows the current at CB. The current at the faulted phase goes up to 5,000 A and other two phase currents change slightly. Figure 6.24 (f) shows the transient currents at RA, after the faulted point. The current at the faulted phase I*a* drops to zero, because the fault current does not flow through RA. The other two phase currents at RA, I*b* and I*c*, show opposite variation according to the distribution line impedance during the fault. However, the magnitudes are smaller than the ones in Figures 6.25 (e) and 6.26 (e), because the FC is not connected.

In Figures 6.25 (a) and (b), transients of real and reactive power with a FC 1,000 kW are similar to the case without a FC. However, the peak of transient power at CB decreases a little bit compared to the case without a FC. Figure 6.25 (c) shows the transients of the faulted phase voltage V*a* in rms value. V*a* drops to zero at t = 1.5 sec and is recovered at t = 1.6 sec. Figures 6.25 (d), (e), and (f) shows the currents at CB, RA, and FC, respectively. In Figure 6.25 (d), the current at the faulted phase goes up to 5,000 A and the other two phase currents increase slightly during the fault. In Figure 6.25 (e), the transient currents at RA show slightly different values according to the impedance of

distribution line and transformer during the fault. Figure 6.25 (f) shows the current from the FC increases during the fault after it is connected at t = 1 sec.

In Figures 6.26 (a) and (b), transients of real and reactive power with a FC 3,000 kW are similar to Figures 6.24 and 6.25. However, the peak of transient power at CB decreases a little bit less compared to the case with a FC providing 1,000 kW. Figure 6.26 (c) shows the transients of the faulted phase voltage V*a* in rms value. V*a* drops to zero at t = 1.5 sec and is recovered at t = 1.6 sec. Figures 6.26 (d), (e), and (f) shows the currents at CB, RA, and FC, respectively. Being different from Figure 6.25 (e), the currents at RA show similar values because the FC supplies most of the load after RA and the magnitudes of the faulted current became bigger than the previous cases.

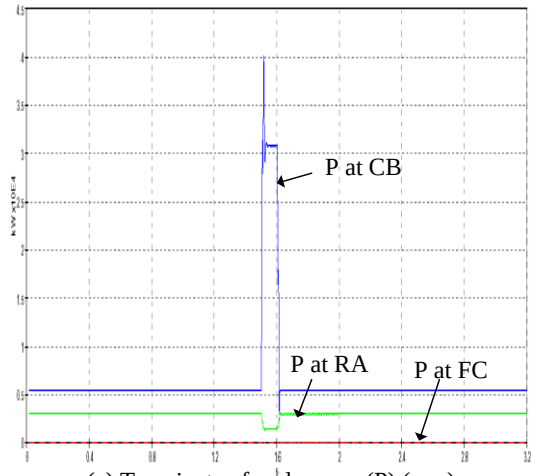

(a) Transients of real power (P) (rms)

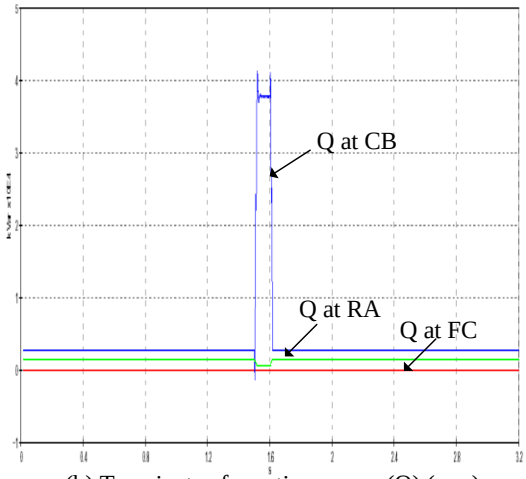

(b) Transients of reactive power (Q) (rms)

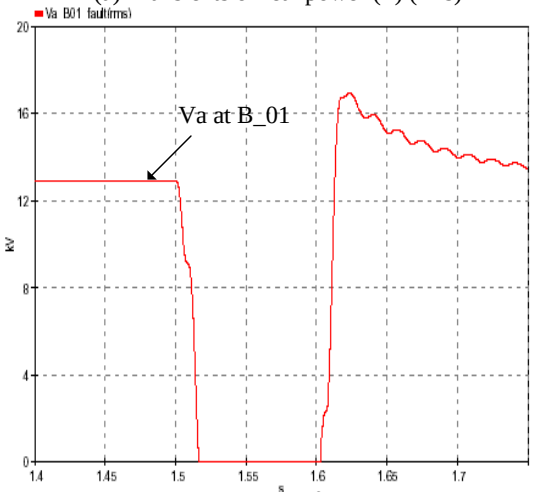

(c) Transients of Va (rms)

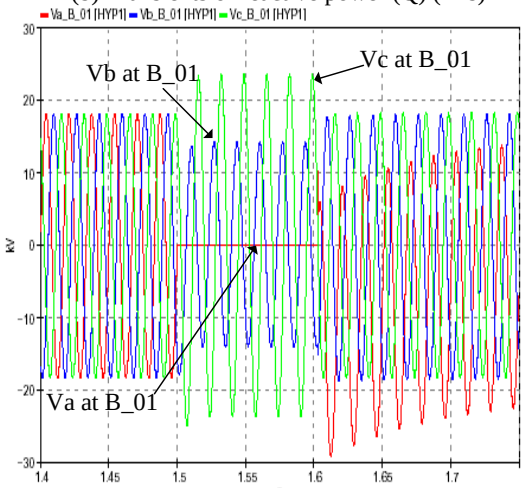

(d) Transients of 3 phase voltage

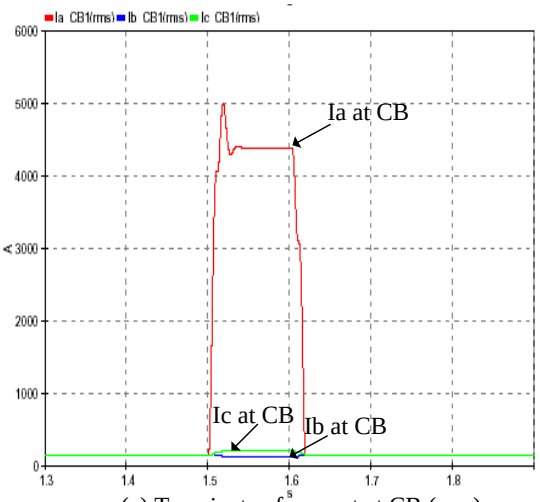

(e) Transients of current at CB (rms)

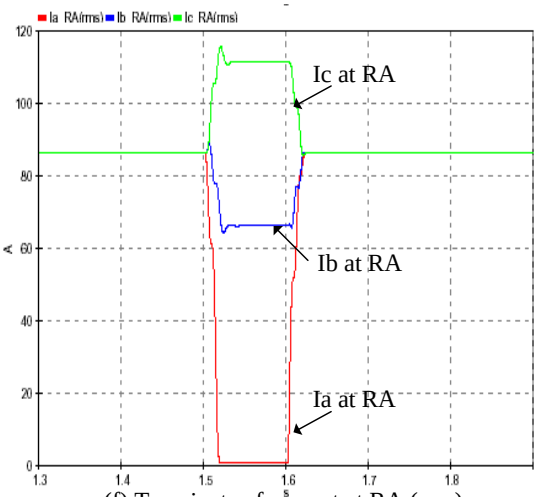

(f) Transients of current at RA (rms)

Figure 6.24. Transients during fault at B_01 without FC.

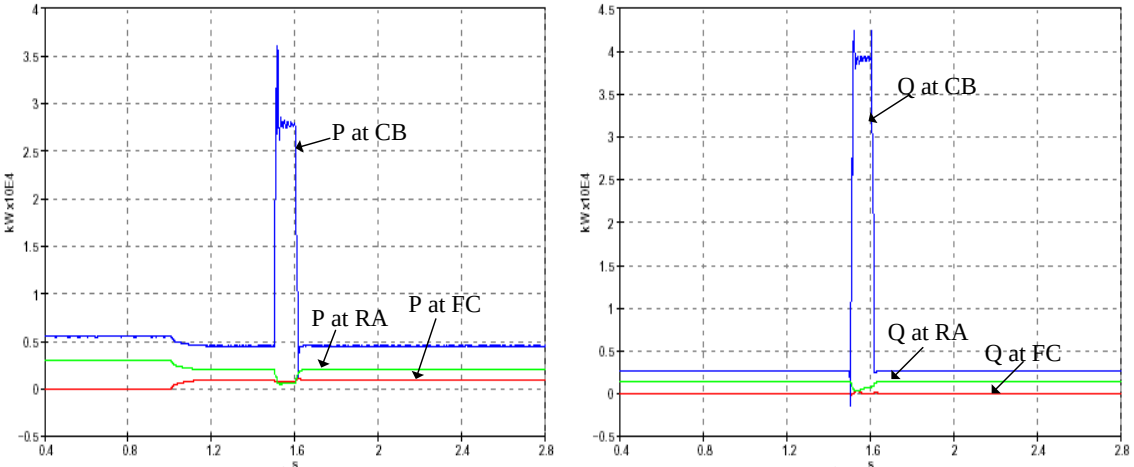

(a) Transients of real power (P) (rms)

(b) Transients of reactive power (Q) (rms)

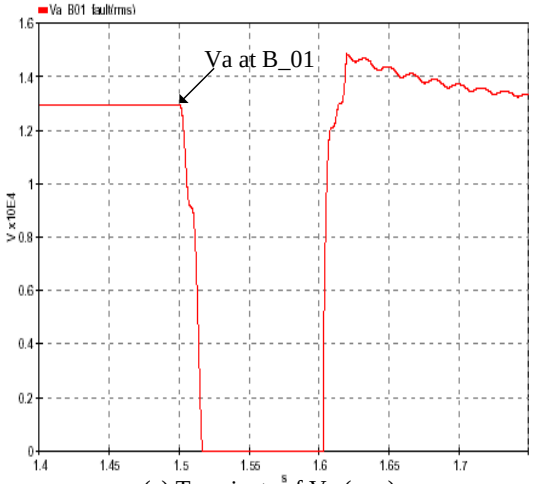

(c) Transients of Va (rms)

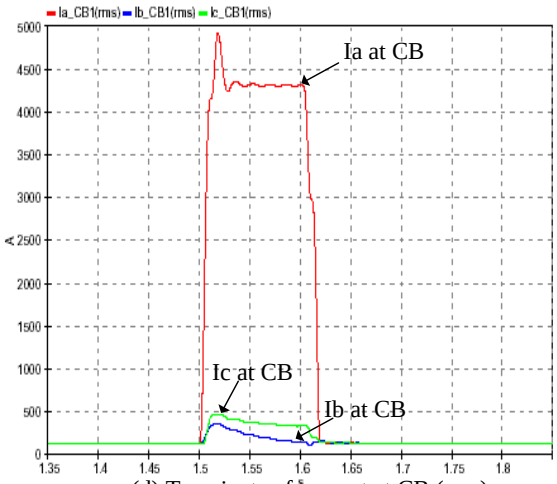

(d) Transients of current at CB (rms)

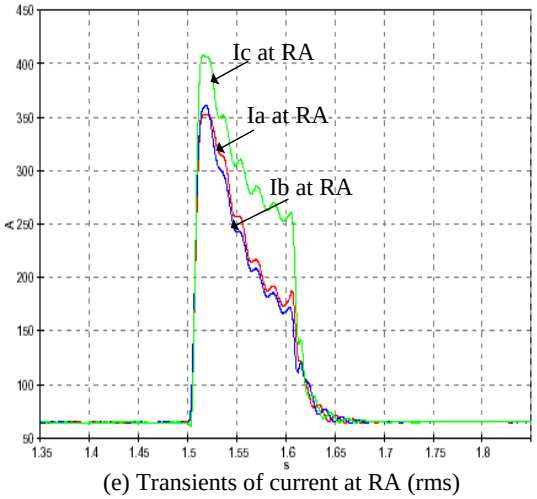

(e) Transients of current at RA (rms)

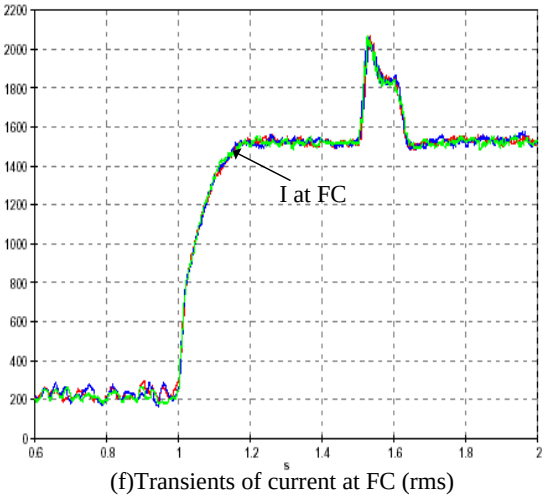

(f)Transients of current at FC (rms)

Figure 6.25. Transients during fault at B_01 with FC 1000 kW.

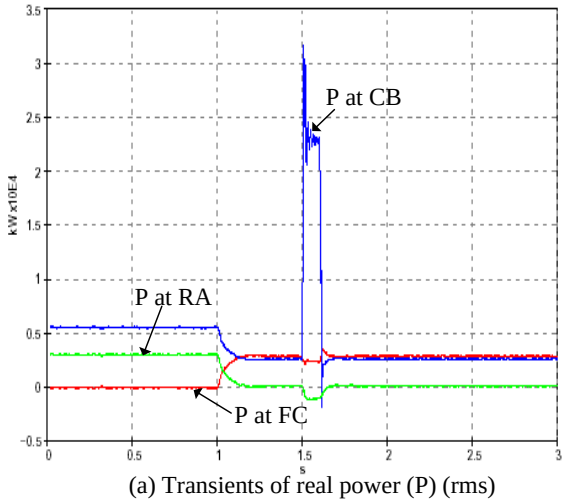

(a) Transients of real power (P) (rms)

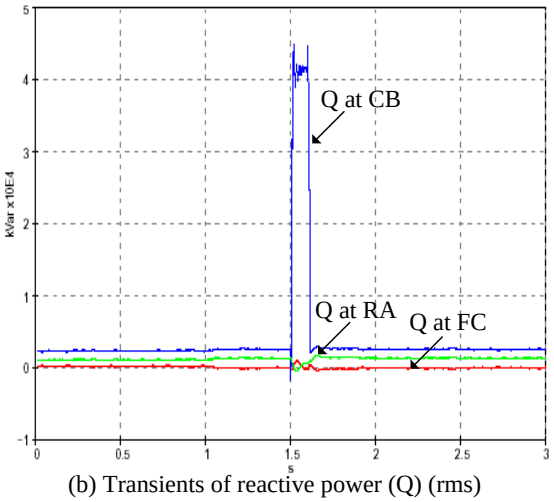

(b) Transients of reactive power (Q) (rms)

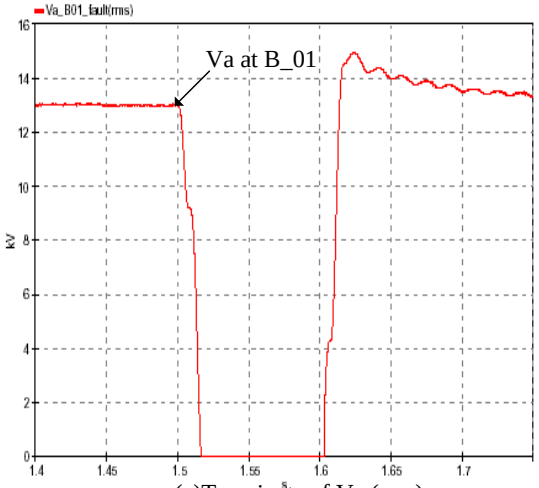

(c)Transients of Va (rms)

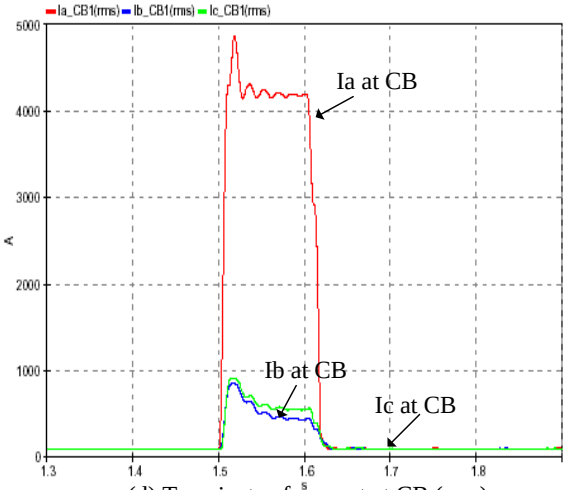

(d) Transients of current at CB (rms)

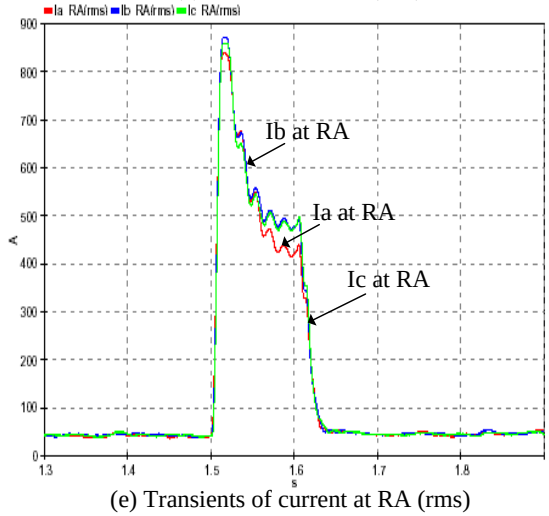

(e) Transients of current at RA (rms)

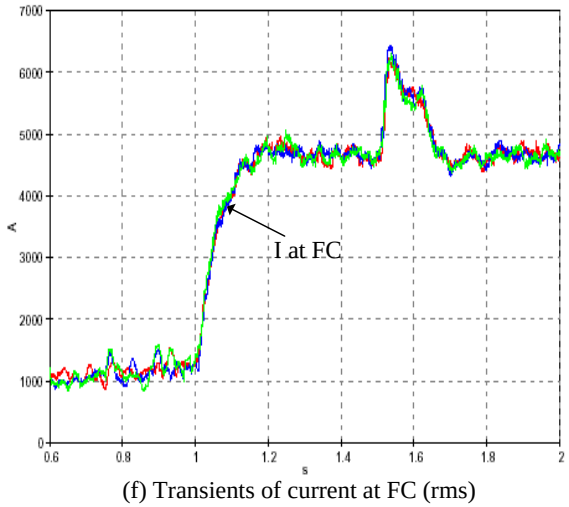

(f) Transients of current at FC (rms)

Figure 6.26. Transients during fault at B_01 with FC 3000 kW.

Figures 6.27 (a) and (b) show the transients of real and reactive power, respectively. Being different from the case of Figures 6.24 (a) and (b), the transients of real and reactive power at RA goes high, because the fault occurred after the point of the FC interface and the fault current flows through it. Figure 6.27 (c) shows the transients of the faulted phase voltage V*a* in rms value similar to Figure 6.24 (c). Figure 6.27 (d) shows the transients of the three-phase voltages. The un-faulted two phase voltages V*b* and V*c* show slight variations temporarily during the fault and recover to normal values. Figure 6.27 (e) shows the current at CB. The current at the faulted phase goes up to 5,000 A and the other two phase currents change slightly. Figure 6.27 (f) shows the transient currents at RA, before the faulted point. The current at the faulted phase I*a* goes high because the fault current passes through the point of a FC interface. The other two phase currents at RA, I*b* and I*c*, show smaller values compared to the fault current.

In Figures 6.28 (a) and (b), the transients of the real and reactive power at RA go high, because the fault current flows through the point of RA. However, the peak of transient power at CB decreases a little bit compared to the case without a FC. Figure 6.28 (c) shows the transients of the faulted phase voltage V*a* in rms value. Figures 6.28 (d), (e), and (f) shows the currents at CB, RA, and FC, respectively. In Figure 6.28 (d), the current at the faulted phase goes up to 5,000 A and other two phase currents increase slightly during the fault. In Figure 6.28 (e), the transient currents at RA show slightly different values according to the impedance of the distribution line and transformer during the fault. Figure 6.28 (f) shows that current of a FC increases during the fault after it is connected at t = 1 sec.

In Figures 6.29 (a) and (b), transients of real and reactive power with a FC 3,000 kW are similar to Figures 6.27 and 6.28. However, the peak of transient power at CB decreases a little bit less compared to the case with a FC 1,000 kW. Figure 6.29 (c) shows the transients of the faulted phase voltage V*a* in rms value. Figures 6.29 (d), (e), and (f) show the currents at CB, RA, and FC, respectively. Being different from Figure 6.28 (e), the currents at RA show similar values because the FC supplies most of load after RA, and the magnitudes of the faulted current became bigger than the previous cases.

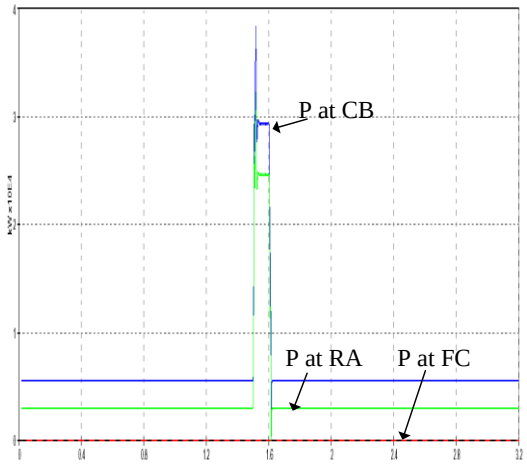

(a) Transients of real power (P) (rms)

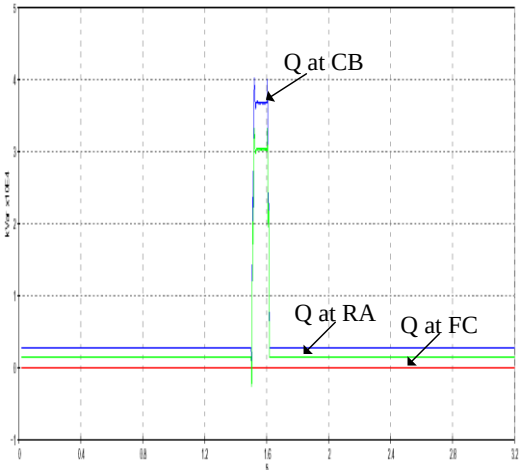

(b) Transients of reactive power (Q) (rms)

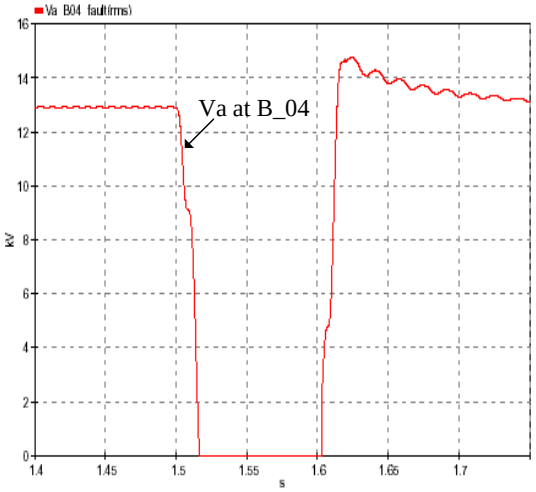

(c)Traansients of Va (rms)

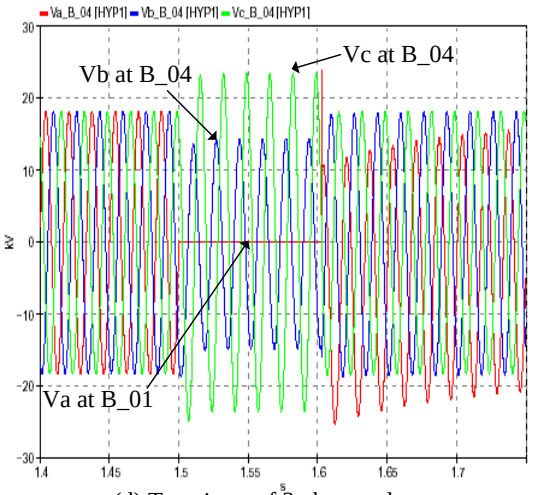

(d) Transients of 3 phase voltage

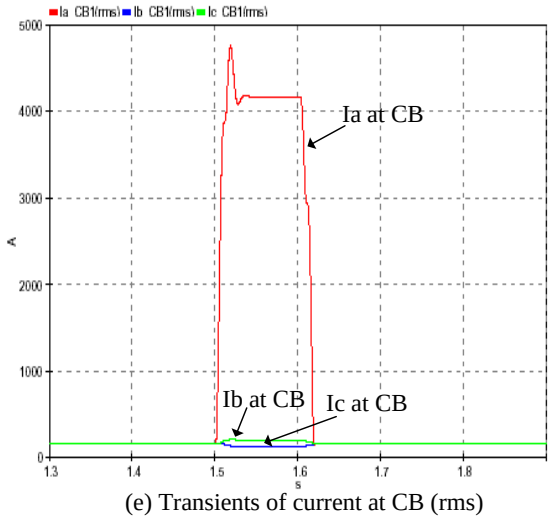

(e) Transients of current at CB (rms)

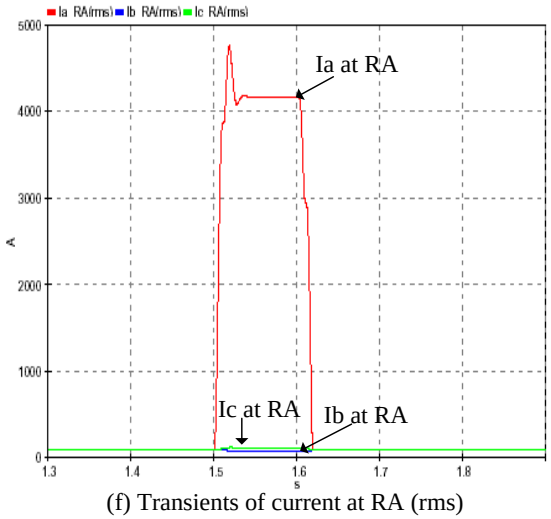

(f) Transients of current at RA (rms)

Figure 6.27. Transients during fault at B_04 without FC.

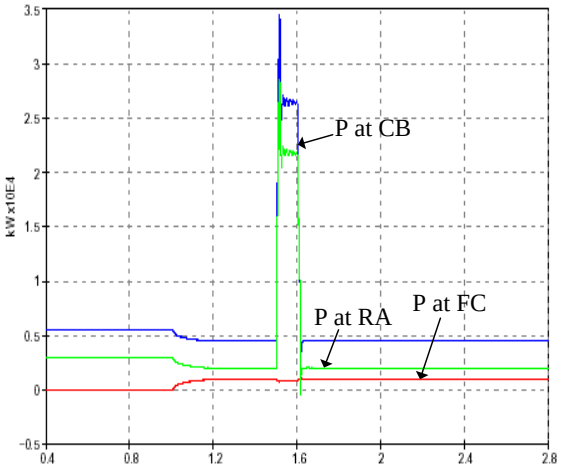

(a) Transients of real power (P) (rms)

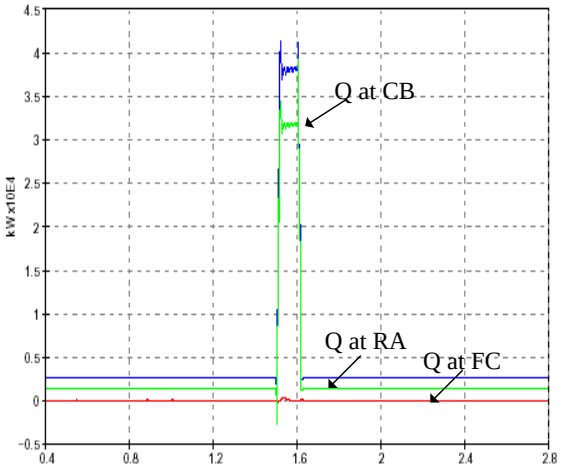

(b) Transients of reactive power (Q) (rms)

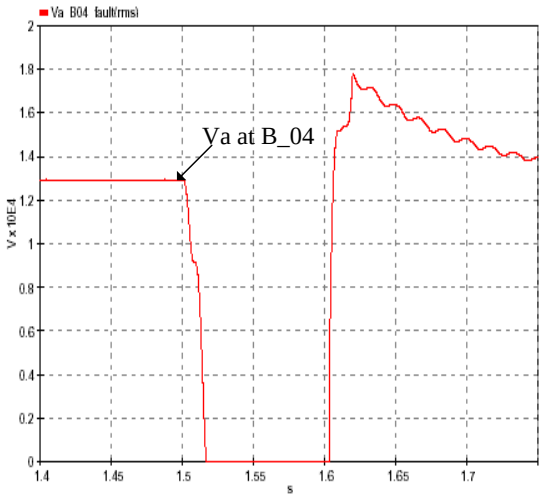

(c)Transients of Va (rms)

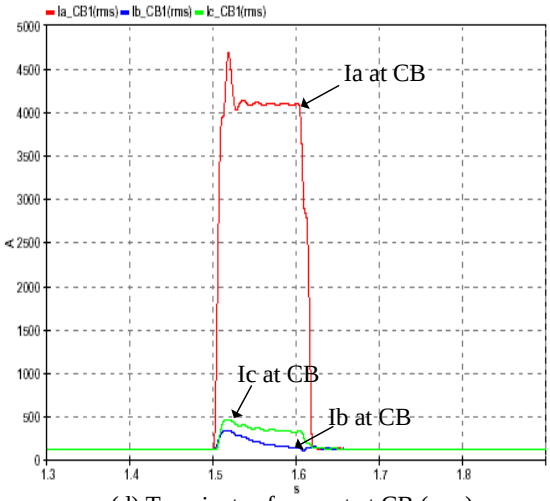

(d) Transients of current at CB (rms)

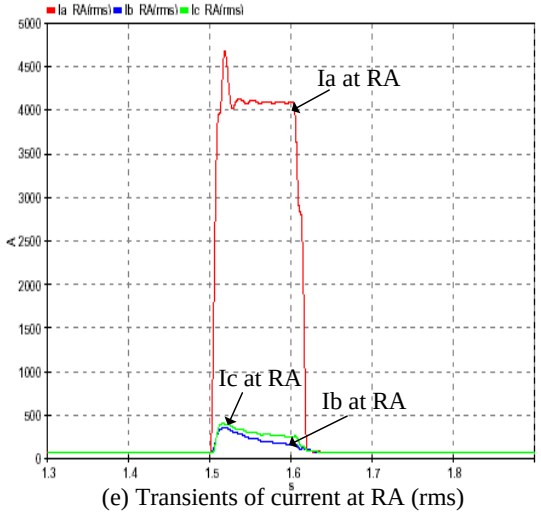

(e) Transients of current at RA (rms)

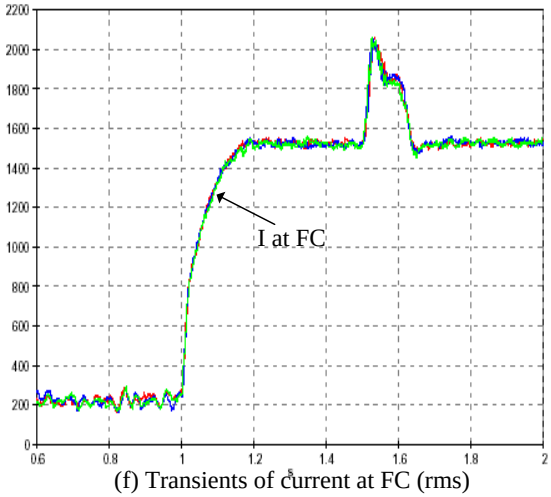

(f) Transients of current at FC (rms)

Figure 6.28. Transients during fault at B_04 with FC 1000 kW.

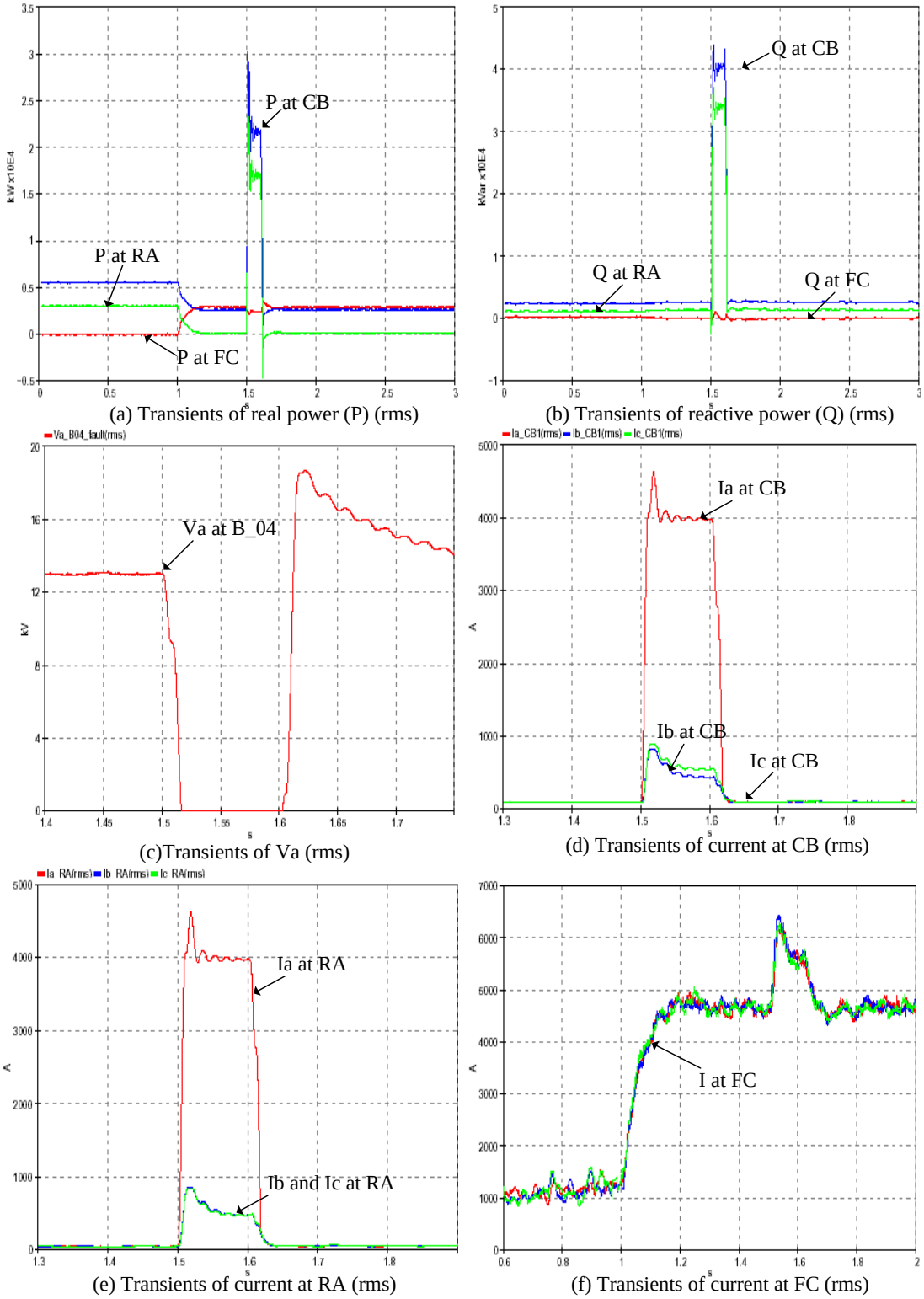

(a) Transients of real power (P) (rms)

(b) Transients of reactive power (Q) (rms)

(c)Transients of Va (rms)

(d) Transients of current at CB (rms)

(e) Transients of current at RA (rms)

(f) Transients of current at FC (rms)

Figure 6.29. Transients during fault at B_04 with FC 3000 kW.

Chapter 7
CONCLUSIONS AND FUTURE WORK

7.1 Conclusions

Fuel cells will start out as a high-cost technology, supplying electricity and gradually become more attractive to mainstream electricity users as they improve in capability and decrease in cost. Among several types of fuel cells, an MCFC stack dynamic model was developed to analyze a spectrum of dynamic responses. An intelligent control was developed for the optimal fuel cell power plant operation.

The major problems in power plant operation including fuel cells, are the coupling problems among systems and optimization problems. A new concept of an intelligent controller, the intelligent setpoint reference governor (I-SRG), using a heuristic algorithm and neural network was developed for a fuel cell power plant. Among several objective functions, load tracking and plant efficiency were solved to find optimal setpoints. Simulation results proved that load changes were followed successfully and the plant efficiency was improved using the I-SRG. The intelligent control technique could be useful for other power plants according to their objectives.

As it is difficult to model an MCFC power plant because of non-linearity and computational fluid dynamics, a NN identification method was used. In the NN modeling, the more parameters used, the higher the random influence on the model. To handle high computational complexity, the FC power plant was divided into three subsystems. NN models for each subsystem and combined system were developed. In the design of

control systems, a NN identifier was used to provide information about the plant to controllers. Simulation results show that NN identification is feasible for modeling an MCFC power plant.

For the successful penetration of a distributed generation to the distribution network, it is required to analyze the effect on the power quality conditions for the customers and utility equipment. Many of these effects can be improved using inverter technologies including real and reactive power control and power flow simulations. A DG interface model to the utility grid was developed and simulated using matlab/simulink for case studies. Operating conflicts and power quality issues were studied to clarify the existing problems. During the simulations with FC switching and line to ground fault, the effective grounding of the transformer at the interface between FC and distribution line can restrict the over-voltage caused by the fault, and any significant impact on FC power plant is not detected. Simulation results proved that the penetration of a FC power plant does not bring any significant impact to an existing distribution network.

7.2 Future Work

The integration of Hybrid Fuel Cells with Gas Turbines is a promising technology. The impetus for the integration is achieving ultra high efficiencies, especially in large-scale power markets where the traditional combined cycles are approaching the sixty percent efficiency mark. The intelligent control technique can be applied to the Hybrid Fuel Cell/Gas Turbine and other power plants to solve their objective

optimization problems. Using optimal setpoints from the intelligent control technique instead of conventional setpoints from linear interpolation, the plant efficiency can be improved, bringing economic benefits.

NN models of the MCFC power plant combining three subsystems can be used for system control and fault diagnosis. The error between actual plant output and the off-line NN identifier output can be used to detect a fault. An adaptive NN identifier can be used as a reference to differentiate a fault from minor sensor errors which can be caused by aging or environmental conditions such as weather and transient disturbances. If the off-line NN identifier shows a fault signal but the adaptive NN identifier does not, that would show a sensor error. Therefore an appropriate decision has to be made such as PI gain tuning, redesign of the I-SRG or the replacement of sensors.

As DGs become increasingly popular, several kinds of DGs might be installed in the same distribution network. Case studies for various kinds of DG-connected distribution networks can be performed using simulation programs to provide necessary information for different characteristics on power quality. The steady state and transient fault analysis need to be compared for the coordination between substation relays and distribution network protectors.

BIBLIOGRAPHY

[1] M. Ilic, F. Galiana and L. Fink, *Power Systems Restructuring*, Kluwer Academic Publishers, M.A., 1998.

[2] K. Y. Lee, "The Effect of DG Using Fuel Cell under Deregulated Electricity Energy Markets," *Proc. of the IEEE Power Engineering Society General Meeting*, in Montreal, Canada, June 18-22, 2006.

[3] Department of Energy, <URL: http://www.energy.gov/>, [Accessed: Feb. 24, 2007].

[4] H. C. Maru and H. Ghezel-Ayagh, "Direct Carbonate Fuel Cell – Gas Turbine Combined Cycle Power Plant," *European Fuel Cell Forum*, A10-4, July 5-8, 2005.

[5] F. Jurado and J. R. Saenz "Adaptive Control of a Fuel Cell-Microturbine Hybrid Power Plant," *IEEE Trans. on Energy Conversion*, vol. 18, No. 2, pp. 342-347, June, 2003.

[6] K. Tran and M. Vaziri, "Effects of dispersed generation (DG) on distribution systems," *IEEE Power Engineering Society General Meeting*, pp.748 – 753, June 12-16, 2005.

[7] T. Ackermann, G. Anderson and L. Soder, "Distributed generation: a definition," *Electric Power Systems Research*, vol.57, pp.195-204, 2001.

[8] El-Samahy and E. El-Saadany, "The effect of DG on power quality in a deregulated environment," *IEEE Power Engineering Society General Meeting*, pp.714 – 721, June 12-16, 2005.

[9] IEA, "Distributed Generation in Liberalized Electricity Markets," Paris, 2002.

[10] T. S. Perry, "Deregulation may give a boost to renewable resources," *IEEE Spectrum*, pp.87, Jan., 2001.

[11] W. Sweet, "Networking assets," *IEEE Spectrum*, pp.84 – 88, Jan., 2001.

[12] Iannone, S. Leva and D. Zaninelli, "Hybrid photovoltaic and hybrid photovoltaic-fuel cell system: Economic and environmental analysis," *IEEE Power Engineering Society General Meeting*, pp.2289 – 2295, June 12-16, 2005.

[13] A. J. Appleby and F. R. Foulkes, *Fuel Cell Handbook*, Van Nostrand Reinhold, New York, 1989.

[14] EG & G Technical Services, Inc. and Science Applications International Corporation, *Fuel Cell Handbook*, 6^{th} *edition*, U.S. Department of Energy Office

of Fossil Energy, National Energy Technology Lab., Morganton, West Virginia, Nov., 2002.

[15] California Distributed Energy Resource, <URL: http://www.energy.ca.gov/> [Accessed Mar. 3, 2007].

[16] M. D. Lukas, K. Y. Lee, and H. Ghezel-Ayagh, "Development of a Stack Simulation Model for Control Study on Direct Reforming Molten Carbonate Fuel Cell Power Plant," *IEEE Transactions on Energy Conversion*, Vol. 14, No. 4, pp. 1651-1657, 1999.

[17] T. P. O'shea and A. J. Leo, "The Santa Clara Demonstration Project 2-MW Direct Carbonate Fuel Cell Power Plant," *29th IECEC Meeting*, pp. 817-822, Monterey, CA, 1994.

[18] M. Monn, "Project Brings Fuel Cell Closer to Utility Use," *Power*, Vol. 139, No. 4, pp. 76-79, April, 1995.

[19] M. Farooque, "Development of Internal Reforming Carbonate Fuel Cell Technology, Final Report," *prepared for U.S. DOE/METC, DOE/MC/23274-2941*, pp. 3-6 to 3-11, October, 1991.

[20] T. Shinoki, M. Matsumura, and A. Sasaki, "Development of an Internal Reforming Molten Carbonate Fuel Cell Stack," *IEEE Transactions on Energy Conversion*, Vol. 10, No. 4, December, 1995.

[21] M. D. Lukas, K. Y. Lee, and H. Ghezel-Ayagh, "An Explicit Dynamic Model for Direct Reforming Carbonate Fuel Cell Stack," *IEEE Transactions on Energy Conversion*, Vol. 16, No. 3, pp. 289-295, Sep., 2001.

[22] W. He, "Three-dimensional Simulation of a Molten Carbonate Fuel Cell Stack Using Computational Fluid Dynamic Techniques," *Journal of Power Sources*, vol. 55, pp. 25-32, 1995.

[23] E. Achenbach, "Three-dimensional and Time-Dependent Simulation of a Planar Solid Oxide Fuel Cell Stack," *Journal of Power Sources*, Vol. 49, pp. 333-348, 1994.

[24] G. Strobino, L. Pollachini, G. Rocchini, and P. Savoldelli, "Dynamic Behavior of the 100 kW MCFC Compact Unit," *Fuel Cell Seminar*, Palm Springs, CA, Nov. 16-19, 1998.

[25] M. Yamaguchi, T. Saito, M. Izumitani, S. Sugita, and Y. Tsutsumi, "Analysis of Control Characteristics Using Fuel Cell Plant Simulator," *IEEE Transactions on Industrial Electronics*, Vol. 37, Issue 5, pp. 378-386, Oct., 1990.

[26] W. He, "A Simulation Model for Integrated Molten Carbonate Fuel Cell Systems," *Journal of Power Sources*, Vol. 49, pp. 283-290, 1994.

[27] J. H. Hirschenhofer, D. B. Stauffer, R. R. Engleman, and M. G. Klett, *Fuel Cell Handbook*. U.S. Department of Energy, 1998.

[28] E. S. Wagner and G. F. Froment, "Steam Reforming Analyzed," *Hydrocarbon Processing*, July, 1992.

[29] K. Denbigh, *Principles of Chemical Equilibrium*, Cambridge University Press, London, 1971.

[30] M. V. Twigg, *Catalyst Handbook*, Wolfe Publishing Ltd., London, 1989.

[31] G. Wilemski, H. G. Ghezel-Ayagh, P. S. Patel, and H. C. Maru, "Modeling of Internal Reforming Direct Fuel Cell," *Fuel Cell Seminar*, pp. P1-2A to P1-2E, Tucson, AZ, May 19-22, 1985.

[32] T. L. Wolf and G. Wilemski, "Molten Carbonate Fuel Cell Performance Model," *Journal of the Electrochemical Society*, Vol. 130, No. 48, 1983.

[33] J. Xu and G. F. Froment, "Methane Steam Reforming: II. Diffusional Limitations and Reactor Simulation," *AIChE Journal*, Vol. 35, No. 1, pp. 97-103, 1989.

[34] S. E. Sandler, *Chemical and Engineering Thermodynamics*, John Wiley & Sons, New York, 1989.

[35] G. F. Froment and K. B. Bischoff, *Chemical Reactor Analysis and Design*, John Wiley & Sons, New York, 1990.

[36] J. Ding, P. S. Patel, M. Farooque, and H. C. Maru, "A Computer Model for Direct Carbonate Fuel Cells," *Proceedings of the Fourth International Symposium on Carbonate Fuel Cell Technology*, Montreal, Quebec, 1997.

[37] M. D. Lukas, K. Y. Lee, and H. Ghezel-Ayagh, "Modeling, Simulation, and Control of Direct Reforming Molten Carbonate Fuel Cell Power Plant," *The Fourth IFAC Symposium on Power Plants & Power Systems Control* 2000, pp. 127-134, April 26-29, 2000.

[38] M. D. Lukas, K. Y. Lee, and H. Ghezel-Ayagh, "Performance Implications of Rapid Load Changes in Carbonate Fuel Cell Systems," *Proc. IEEE Power Engineering Society Winter Meeting*, #2001WM255, Jan., 2001.

[39] M. D. Lukas, K. Y. Lee, and H. Ghezel-Ayagh, "Operation and Control of Direct Reforming Fuel Cell Power Plant," *Proceedings of the 2000 IEEE Power Engineering Society Winter Meeting*, Jan., 2000.

[40] H. Kwakernaak and R. Sivan, *Linear Optimal Control Systems*, Wiley, New York, 1972.

[41] F. G. Shinskey, *Process Control Systems, Application, Design, and Tuning*, Mc-Graw Hill, New York, 1988.

[42] M. D. Lukas, K. Y. Lee, and H. Ghezel-Ayagh, "Modeling and Cycling Control of Carbonate Fuel Cell Power Plants," *Control Engineering Practice*, Vol. 10, pp. 197-206, 2002.

[43] K. Ogata, *Modern Control Engineering*, Prentice Hall, New Jersey, 1990.

[44] K. Y. Lee, X. Bai, and Y. M. Park, "Optimization Method for Reactive Power Planning Using a Genetic Algorithm," *IEEE Transactions on Power Systems*, Vol. 10, No. 10, pp. 1843-1850, Nov., 1995.

[45] Dimeo, R. and K. Y. Lee, "Boiler-Turbine Control System Design Using a Genetic Algorithm," *IEEE Transactions on Energy Conversion*, Vol. 10, No. 4, pp. 752-759, Dec., 1995.

[46] Park, Y. M., M. S. Choi, and K. Y. Lee, "A Neural Network-Based Power System Stabilizer Using Power Floor Characteristics," *IEEE Transactions on Energy Conversion*, Vol. 11, No. 2, pp. 442-448, June, 1996.

[47] Park, Y. M., M. S. Choi, and K. Y. Lee, "An Optimal Tracking Neuro-Controller for Nonlinear Dynamic Systems," *IEEE Transactions on Neural Networks*, Vol. 7, No. 5, pp. 1099-1110, Sep., 1996.

[48] Zhao, Y., R. M. Edwards, and K. Y. Lee, "Hybrid Feedforward and Feedback Controller Design for Nuclear Steam Generators over Wide Range Operation Using Genetic Algorithm," *IEEE Transactions on Energy Conversion*, Vol. 12, No. 1, pp. 100-106, March, 1997.

[49] K. Y. Lee and F. F. Yang, "Optimal Reactive Power Planning Using Evolutionary Algorithms: A Comparative Study for Evolutionary Programming, Evolutionary Strategy, Genetic Algorithm, and Linear Programming," *IEEE Transactions on Power Systems*, Vol. 13, No. 1, pp. 101-108, Feb., 1998.

[50] Ghezelayagh, H. and K. Y. Lee, "Neuro-Fuzzy Identifier of a Boiler System," *Engineering Intelligent Systems*, Vol. 7, No. 4, pp. 227-231, Dec., 1999.

[51] K. Y. Lee, M. Perakis, D. R. Sevcik, N. I. Santoso, G. K. Lausterer, and T. Samad, "Intelligent Distributed Simulation and Control of Power Plant," *IEEE Transactions on Energy Conversion*, Vol. 15, No. 1, pp. 116-123, March, 2000.

[52] Park, J.-B., Y.-M. Park, J.-R. Won, and K. Y. Lee, "An Improved Genetic Algorithm for Generation Expansion Planning," *IEEE Transactions on Power Systems*, Vol. 15, No. 3, pp. 916-922, Aug., 2000.

[53] Garduno-Ramirez R. and K. Y. Lee, "Multiobjective Optimal Power Plant Operation Through Coordinate Control with Pressure Set Point Scheduling," *IEEE Transactions on Energy Conversion*, Vol. 16, No. 2, pp. 115-122, June, 2001.

[54] Garduno-Ramirez, R. and K. Y. Lee, "Intelligent Hybrid Coordinated-Control of Fossil Fuel Power Units" *Proc. International Conference on Intelligent System Applications to Power Systems*, pp. 177-182, Budapest, June, 2001.

[55] Garduno-Ramirez, R. and K. Y. Lee, "A Multiobjective-Optimal Neuro-Fuzzy Extension to Power Plant Coordinated Control," *Transactions of the Institute of Measurement and Control*, Vol. 24, No. 2, pp. 159-192, 2002.

[56] Garduno-Ramirez, R. and K. Y. Lee, "Intelligent Multiagent Control for Power Plants," *Intelligent Systems: Technology and Applications*, (C. T. Leondes, Editor), Vol. 6, pp. 181-209, CRC Press, June, 2002.

[57] Garduno-Ramirez, R. and K. Y. Lee, "Extending Plant Load-Following Capabilities," *Thermal Power Plant Simulation and Control*, IEE Press, Stevenage, UK, Sep., 2002.

[58] K. Y. Lee, "Tutorial on Modern Heuristic Optimization Techniques with Applications to Power Systems," *IEEE Power Engineering Society*, IEEE Catalog Number 02TP160, Piscataway, NJ, 2002.

[59] J. S. Heo and K. Y. Lee, "A multi-agent system-based intelligent identification system for control and fault-diagnosis for a large-scale power plant," *IEEE Power Engineering Society General Meeting*, June, 2006.

[60] J. S. Heo, "A Multi-Agent System-based Intelligent Control for Large-Scale Power Plants," *Ph. D. Thesis*, Dept. of Electrical Engineering, The Pennsylvania State University, 2006.

[61] Angeline, P. "Using selection to improve particle swarm optimization," *Proceeding of IEEE International Conference on Evolutionary Computation*, pp. 84-89, 1988.

[62] P. Antsaklis (Eds.), "Special issue on neural network in control systems," *IEEE Control System Magazine*, vol. 10, No. 3-87, April, 1990.

[63] A. Guez and J. Selinsky, “A trainable neuromorphic controller,” *J. Robotic System,* vol. 5, No. 4, pp. 363-388, 1988.

[64] K. Y. Lee, C. C. Ku and R. M. Edwards, “A neural Network for Adapting Neuclear Power Plant Control for Wide Range Operation,” *Transactions of the American Neural Society*, Vol. 63, pp. 114-115, June, 1991.

[65] Garduno-Ramirez R. and K. Y. Lee, “Wide-Range Operation of a Power Unit via Feedforward Fuzzy Control,” *IEEE Transactions on Energy Conversion*, Vol. 15, No. 4, pp. 421-426, Dec., 2000.

[66] K. Y. Lee, T. I. Choi, C. C. Ku, and J. H. Park, “Short-Term Load Forecasting Using Diagonal Recurrent Neural Network,” *Proc. of the 2nd international Forum on Application of Neural Networks to Power Systems*, pp. 227-232, Yokohama, Japan, April 19-22, 1993.

[67] K. Y. Lee, T. I. Choi, and C. C. Ku, “Neural Network Architecture for Short-Term Load Forecasting,” *Proc. of IEEE international Conference on Neural Networks, IEEE World Congress on Computational Intelligence*, pp. 4724-4729, Orlando, FL, June 28-July 2, 1994.

[68] C. C. Ku, K. Y. Lee and R. M. Edwards, "Improved Nuclear Reactor Temperature Control Using Diagonal Recurrent Neural Networks," *IEEE Transactions on Nuclear Science*, Vol. 39, No. 6, pp. 2298-2309, Dec., 1992.

[69] Batzel, T. D. and K. Y. Lee, “Sensorless Operation of the Permanent Magnet Synchronous Motor using the Diagonal Recurrent Neural Network”, *Proc. International Conference on Intelligent System Applications to Power Systems*, pp. 53-58, Budapest, June 2001.

[70] C. C. Ku and K. Y. Lee, "Diagonal Recurrent Neural Network for Dynamic Systems Control," *IEEE Transactions on Neural Networks*, Vol. 6, pp. 144-156, Jan., 1995.

[71] Neural Network TOOLBOX, For Use with MATLAB, User’s Guide Version 4, The Math Works Inc., 2006.

[72] C. Wang, M. H. Nehrir, and S. R. Shaw, “Dynamic models and model validation for PEM fuel cells using electrical circuits,” *IEEE Trans. on Energy Conversion*, vol. 20, No. 2, pp. 442-451, June, 2005.

[73] D. Georgakis and S. Papathanassiou, “Modeling of grid-connected Fuel cell plants,” *Proc. CIGRE Symposium “Power Systems with Dispersed Generation,”* Athens, April, 2005.

[74] Mustapha Raou and Moulay Tahar Lamchich, "Average current mode control of a voltage source inverter connected to the grid: application to different filter cells," *Journal of Electrical Engineering*, vol. 55, No. 3-4, 2004.

[75] Koen J. P. Macken, Jeroen Van den Keybus, and Ronnie J. M. Belmans, "Distributed Control of Renewable Generation Units With Integrated Active Filter," *IEEE Transactions on Power Electronics*, vol. 19, No. 5, pp. 1353-1360, Sep., 2004.

[76] X. Yuan, W. Merk, H. Stemmler, and J. Allmeling, "Stationary-frame generalized integrators for current control of active power filters with zero steady-state error for current harmonics of concern under unbalanced and distorted operating conditions," *IEEE Trans. Ind. Appl.*, vol. 38, no. 2, pp. 523–532, Mar./Apr., 2002.

[77] R. Teodorescu, F. Blaabjerg, U. Borup, and M. Liserre, "A new control structure for grid-connected LCL PV inverters with zero steady-state error and selective harmonic compensation," *Proc. of APEC'04*, vol. 1, pp. 22-26, 2004.

[78] R. Lasseter and P. Piagi, "Providing Premium Power through Distributed Resources," *Proceedings of the 33rd Hawaii International Conference on System Sciences*, 2000.

[79] P. Giroux, G. Sybille, and H. Le -Huy, "Modeling and Simulation of a Distribution STATCOM using Simulink's Power System Blockset", *IECON'01: 27th Annual Conference of the IEEE Industrial Electronics Society*, pp. 990-994, 2001.

[80] R. Lasseter, K. Tomsovic, and P. Piagi, "Scenarios for Distributed Technology Applications with Steady-State and Dynamic Models of Loads and Micro-Sources," *Power System Engineering Research Center*, University of Wisconsin, April 14, 2000. (http://certs.lbl.gov/pdf/PSERC_deri.pdf)

[81] M. C. Chandorkar, D. M. Divan, and R. Adapa, "Control of Parallel Connected Inverters in Standalone ac Supply Systems," *IEEE Transaction on Industry Applications*, Vol. 29, No. 1, Jan/Feb., 1993.

[82] M. N. Marwali, J. W. Jung, and A. Keyhani, "Control of Distributed Generation Systems, Part 2: Load Sharing Control", *IEEE Trans. on Power Electronics*, Vol. 19, pp. 1551-1561, Nov., 2004.

[83] Lucian Asiminoaei, Remus Teodorescu, Frede Blaabjerg, and Uffe Borup, "A Digital Controlled PV-Inverter With Grid Impedance Estimation for ENS

Detection," *IEEE Trans. on Power Electronics*, vol. 20, No. 6, pp. 1480-1490, Nov., 2005.

[84] Willis, H. L., "Analytical Methods and Rules of Thumbs for Modeling DG-Distribution Interaction," in *Power Engineering Society Summer Meeting*, Vol. 3, Jul., 2000.

[85] M. Y. Vaziri, "Effects of Cogeneration On Distribution System", *Master Thesis*, California State University, Sacramento, 1991.

[86] H.-J. Choi and J.-C. Kim, "Advanced Voltage Regulation Method at the Power Distribution Systems Interconnected with Dispersed Storage and Generation Systems," *IEEE Transactions on Power Delivery*, Vol. 6, Issue 3, May, 1992.

[87] R. C. Dugan and T. E. Mcdermott, "Distributed Generation," *IEEE Industry Applications Magazine*, pp. 19-25, Mar/Apr., 2002.

[88] P. P. Barker and R. W. de Mello, "Determining the impact of distributed generation on power systems: *Part 1 - radial distribution systems*," in *Proc. IEEE Power Engineering Soc. Summer Meeting*, vol. 3, pp. 1645-1656, 2000.

[89] R. C. Dugan, M. F. McGranaghan, S. Santoso, and H. W. Beaty, "Electric power systems quality, 2nd edition," *McGraw-Hill Professional Engineering*, New York, 2002.

[90] "IEEE Recommended Practice for Utility Interface of Photovoltaic (PV) Systems," *IEEE Std. 929-2000*, April, 2000.

[91] T. I. Choi and K. Y. Lee, "Distribution Automation Using CDMA," *IEEE Power Engineering Society General Meeting*, Montreal, June, 2006.

[92] "California Electric Rule 21 Supplemental Review Guideline," *California Energy Commission*, Rule 21 Working Group, 2004.

[93] A. Bhowmik, A. Maitra, A. M. Halpin, and J. E. Schatz, "Determination of Allowable Penetration Levels of Distributed Generation Resources Based on Harmonic Limit Considerations" *IEEE Transactions on Power Delivery*, Vol. 18, No. 2, , pp. 619-624. April, 2003.

[94] A. A. Papathanassiou and D. N. Hatziargyriou, "Technical Requirements for the Connection of Dispersed Generation to the Grid," in *IEEE Power Engineering Society Summer Meeting*, Vol. 2, Jul., 2001.

[95] B. Ling, "Distribution Series Capacitor for Controlling Voltage Dip and Fluctuation When A Motor Starts," *Master Thesis*, Staffordshire University, Stoke on Trent, UK, 1996.

[96] "IEEE Recommended Practices and Requirements for Harmonic Control in Electric Power Systems," *IEEE Std. 519-1992*, 1992.

[97] T.-T Chang and H.-C. Chang, "An efficient Approach for reducing Harmonic Voltage Distortion in Distribution Systems with Active Power Line Conditioners," *IEEE Transactions on power delivery*, Vol. 15, No. 3, July, 2000.

[98] R. Caldon, F. Rossetto, and R. Turri, "Analysis of Dynamic Performance of Dispersed Generation Connected through Inverter to Distribution Networks," *17th International Conference on Electricity Distribution, CIRED*, Barcelona, May 12-15, 2003

Appendix

□ Process Equations for Oxidizer

Oxidizer Gas Composition

$$\frac{dx_{CO_2,ox}}{dt} = \alpha_1 \left\{ \alpha_2 x_{CO_2,ox} + N_{ox}^{gas} \left(x_{CO_2,ox}^{gas} + x_{CO,ox}^{gas} + x_{CH_4,ox}^{gas} \right) \right\}$$

$$\frac{dx_{H_2O,ox}}{dt} = \alpha_1 \left\{ \alpha_2 x_{H_2O,ox} + N_{ox}^{gas} \left(x_{H_2O,ox}^{gas} + x_{H_2,ox}^{gas} \right) \right\}$$

$$\frac{dx_{N_2,ox}}{dt} = \alpha_1 \left\{ \alpha_2 x_{N_2,ox} + N_{ox}^{air} x_{N_2,air}^{air} \right\}$$

$$x_{O_2,ox} = 1 - [x_{CO_2,ox} + x_{H_2O,ox} + x_{N_2,ox}]$$

As with the fuel cell stack, we complete the dynamics by describing the remaining independent properties.

Oxidizer Temperature

$$\frac{dT_{ox}}{dt} = \frac{N_{ox}^{gas}(\overline{h_{ox}^{gas}} \cdot \overline{x_{ox}^{gas}}) + N_{ox}^{air}(\overline{h_{air}} \cdot \overline{x_{air}}) - N_{ox} - (\overline{h_{ox}} \cdot \overline{x_{ox}})}{3600 M_{ox} C_{pox}}$$

where $\overline{h_{ox}^{gas}}$, $\overline{h_{air}}$, and h_{ox} are approximately defined vectors of molar enthalpy at anode off-gas temperature, air temperature, and oxidizer temperature respectively. Similarly,

$\overline{x_{ox}^{gas}}$, $\overline{x_{air}}$, and $\overline{x_{ox}}$ are compositions of anode off-gas, air, and oxidizer. Respectively. The oxidizer mass-specific heat product is denoted $M_{ox}C_{pox}$. Oxidizer pressure follows, by analogy.

Oxidizer Pressure

$$\frac{dP_{ox}}{dt} = -\alpha_1 P_{ox}[-\alpha_2 + 2N_{ox}^{gas} x_{CH_4,ox}^{gas} + N_{ox} - \frac{T_{ox}}{\alpha_1 T_{ox}}$$

Process Equations for Fuel Cell Stack

The analysis proceeds by first realizing that the oxidizer volume is relatively small. As an approximation, then, the oxidizer mole fraction differential equations are replaced by algebraic equations. A second characteristic is that, under fuel utilization control, the anode off-gas composition is practically constant throughout a load disturbance. This can be seen in a ramping load cycle in net AC power demand and the resulting anode gas composition under fuel utilization control.

Thus, as a good approximation, the anode gas composition can be considered constant. After setting derivatives to zero and using "hat" notation to represent fixed nominal values:

$$X_1 = -(a_4/a_1)\left[x_{CO}^s(a_1 a_3 + X_2) + (1-a_1)N_{ta}^{in} x_{CO}^{in}\right]$$

where,

$$X_2 \equiv \frac{N_{ta}^{in} x_{H_2O}^{in} + r_1 - 2r_3}{x_{H_2O}^s} - \frac{N_{ta}^{in} x_{CO_2}^{in} + r_1 + r_3}{x_{CO_2}^s} - \frac{N_{ta}^{in} x_{H_2}^{in} - r_1 + 4r_3}{x_{H_2}^s} \quad .$$

Thus, a simplified, reduced-order set of equations valid for fast dynamics follows:

Anode Composition

$$\frac{dx_{H_2}^s}{dt} = -\alpha_4\left\{\alpha_3\left(x_{H_2}^s + x_{CO}^s\right) - N_{ta}^{in}\left(x_{H_2}^{in} + x_{CO}^{in}\right) - 4r_3 + r_1\right\} - X_1$$

$$\frac{dx_{CO}^s}{dt} = X_1$$

$$\frac{dx_{CO_2}^s}{dt} = -\alpha_4 \left\{ \alpha_3 \left(x_{CO_2}^s + x_{CO}^s \right) - N_{ta}^{in} \left(x_{CO_2}^{in} + x_{CO}^{in} \right) - r_1 - r_3 \right\} - X_1$$

$$x_{H_2O}^s = \frac{x_{CO_2}^s x_{H_2}^s}{K_{seq} x_{CO}^s}$$

$$x_{CH_4}^s = 1 - \left(x_{H_2}^s + x_{CO}^s + x_{CO_2}^s + x_{H_2O}^s \right)$$

Cathode Composition

$$\frac{dx_{CO_2}^s}{dt} = \alpha_5 \left\{ N_{tc}^{in} \left(x_{CO_2}^{in} - x_{CO_2}^s \right) + \frac{3 x_{CO_2}^s r_1}{2} - r_1 \right\}$$

$$\frac{dx_{O_2}^s}{dt} = \alpha_5 \left\{ N_{tc}^{in} \left(x_{O_2}^{in} - x_{O_2}^s \right) + \frac{3 x_{O_2}^s r_1}{2} - \frac{r_1}{2} \right\}$$

$$(x_{H_2O}^a, x_{CO_2}^a, P_{dc}, h) = f(x_{CH_4}^s, x_{H_2O}^s, x_{CO_2}^s, x_{O_2}^s)$$

Dynamic States

T^s	:	stack solid average temperature
$P_a^s (P_c^s)$	:	anode (cathode) outlet pressures
$x_{ai}^s (x_{ci}^s)$	:	anode (cathode) outlet mole fractions

Constants

$M^s C_p^s$	:	stack solid mass-specific heat product
$V_a (V_c)$	:	anode (cathode) compartment volumes
R	:	universal gas constant
E_2	:	WGS reaction Gibb's free energy constant

Additional Quantities

$N_{ta}^{in} (N_{tc}^{in})$	:	total molar flow into anode (cathode)
$x_{ai}^{in} (x_{ci}^{in})$	:	anode (cathode) inlet mole fractions
$\bar{h}_{ai}^{in} (\bar{h}_{ci}^{in})$	:	anode (cathode) inlet partial molar enthalpies

$\bar{h}_i^s$: partial molar enthalpies at stack temperature

P_{dc} : stack dc power

r_1 : electrochemical reaction rate

r_3 : reforming reaction rate

□ Process Equations for Heat Recovery Unit

Accounting for storage both within the tube fluid and metal mass, energy conservation for the tube side is

$$\frac{d}{dt}[M_m C_{pm} T_m + \rho_t V_t H_t] = M_m C_{pm} \frac{dT_m}{dt} + \rho_t V_t \frac{dH_t}{dt} = Q_t - w_t (H_t - H_t^{in})$$

or

$$[\alpha M_m \frac{C_{pm}}{C_{ptm}} + \rho_t V_t] \frac{dH_t}{dt} = M_e \frac{dH_t}{dt} = Q_t - w_t (H_t - H_t^{in})$$

where

$M_m C_{pm}$: mass-specific heat product of tube metal [Btu/R]

T_m: Tube metal temperature [R]

ρ_t: tube-side fluid density [lbm/ft^3]

V_t: tube-side fluid volume [ft^3]

H_t: tube-side fluid specific enthalpy [Btu/lbm]

Q : convection heat transfer rate [Btu/hr]

w_t : fluid mass flow rate on tube-side [lbm/hr]

H_t^{in}: specific enthalpy of tube-side [Btu/lbm]

C_{pt}: constant pressure specific heat of tube-side fluid [Btu/(lbm · R)]

α : ratio of metal temperature to fluid rtemperature

T_t: tube-side fluid temperature [R]

M_e: effective mass [lbm]

VITA

Tae-Il Choi

EDUCATION:

Ph.D., Electrical Engineering, May 2008, M.S., Electrical Engineering, May 1993, The Pennsylvania State University, University Park, PA 16802.

B.S., Electrical Engineering, February 1982, Hanyang University, Seoul, Korea.

EXPERIENCE:

Manager	Korea Electric Power Corporation	04/01-11/07
Research Assistant	The Pennsylvania State University	09/05-12/06
Affiliated Professor	Kwangwoon University, Korea	01/01-12/03
Engineer, Assist. Manager	Korea Electric Power Corporation	01/82-04/01

PUBLICATION:

- Choi, Tae-Il and Lee, Kwang Y., "Distribution Automation Using CDMA," *IEEE Power Engineering Society General Meeting*, in Montreal, Canada, pp. 6, June 18-22, 2006.
- Choi, Tae-Il; Lee, Kwang Y.; Junker, S. Tobias; Ghezel-Ayagh, Hossein, " Neural Network Supervisor for Hybrid Fuel Cell/Gas Turbine Power Plants," *IEEE Power Engineering Society General Meeting*, pp. 1-8, June 24-28, 2007.
- Choi, Tae-Il, Lee, Kwang Y., Lee, Dong R., and Ahn, Jeong K., "Communication System for Distribution Automation including CDMA," admitted for Journal of the *IEEE Power Delivery*, January 2008
- Choi, Tae-II and Lee, Kwang Y., "Intelligent Control of a Fuel Cell Power Plant," submitted for *International Federation of Automatic Control* (*IFAC) Symposium on Power Plants & Power Systems Control*, Seoul, June 2008.
- Choi, Tae-Il and Lee, Kwang Y., "Interface of a Fuel Cell Distributed Generator to the Utility System," submitted for *Proc. of the IEEE Power Engineering Society General Meeting*, in Pittsburgh, 2008.